UNIVERSITY OF BERGEN

Department of Physics and Technology

MASTER'S THESIS IN OCEAN TECHNOLOGY

Flow measurements in the wake of multirotor wind turbine arrangements

---

By: Thomas Eriksen

June 2023

This page is intentionally left blank.

Abstract

Traditional single rotor wind turbines face challenges as the rotor diameter increases to meet energy requirements. This leads to higher manufacturing, transportation, and installation costs, giving rise to multirotor wind turbines as a viable alternative. However, multirotor wind turbines also introduce new challenges, such as complex wake interactions that require further exploration. Understanding these wake interactions is critical for optimizing the setup of multirotor wind turbines both individually and in farm arrangements.

This thesis investigates the wake flow behind different setups of downscaled multirotor wind turbines. Velocity reduction and turbulent kinetic energy will be investigated from an upstream and downstream perspective. The experiments are conducted on a submerged multirotor in the towing tank at Western Norway University of Applied Sciences (HVL). The experiments utilize lab-scaled actuator discs and employ an Acoustic Doppler Velocimetry (ADV) and a new Particle Image Velocimetry (PIV) system for measuring the wake flow. Different arrangements of a single rotor (SR) and multirotor of seven rotors (MR7) are compared, where the center disc's solidity is varied. This is done to introduce a non-even thrust distribution in the center of the MR7 in order to provoke initial gradients in the wake.

The results show that increasing center disc solidity leads to higher velocity reduction and wider wakes. The local velocity gradients around the center disc increase as the upstream induction zone expands, increasing initial turbulent kinetic energy levels in the wake. However, larger disc solidities result in smaller velocity reductions than single rotors. The disc configuration with the highest solidity shows the highest velocity reduction, turbulent kinetic energy, and shear stresses in the near wake. As a result, the wake behind this configuration regenerates faster than others due to the high mixing with the free stream.

The results indicate multirotors' potential to unevenly distribute rotor thrust and influence wake flow recovery by the resulting local flow velocity gradients. Flow measurements of both mean velocities and turbulent quantities attained with the new PIV system compare very well with previously measured ADV results, making the PIV system a powerful tool for full-field flow measurements in the towing tank.

This page is intentionally left blank.

Acknowledgment

My past year in the ocean technology study program has been challenging and fruitful. Through my master's project, I have acquired more knowledge related to a current topic within renewable energy: offshore multirotor wind turbines. The making of this thesis would not have been possible without some key persons. First and foremost, I would like to express my most incredible gratitude toward my primary supervisor, Jan Bartl. The constructive meetings and fruitful discussions have been very helpful in developing my knowledge about the field. Furthermore, he has provided me with relevant literature and contributed with much-appreciated guidance during the experimental campaign. Next, I would also like to thank my administrative supervisor from the University of Bergen, Bjørn Tore Hjertaker, who had a great impact in terms of proofreading and giving advice about the general structure of the thesis.

I would also like to thank the Western Norway University of Applied Sciences lab engineers, Frode Wessel Jansen and Harald Moen, and the other supervisors, Gloria Stenfelt and David Roger Lande-Sudall. Everyone has been very open and helpful during the setup and use of the brand-new measurement system, particle image velocimetry. Additionally, a shout-out goes to my fellow students and wind turbine colleagues, Ørjan Lunde and Daniel Sukhman, for many insightful discussions about the multirotor theme. Additionally, I would like to acknowledge the help of Juli Grønaas Kvamme and Sondre Tolleifsen during the experimental campaign. Last but not least, a big gratitude goes out to my girlfriend, Enya Rasmussen, who has been very supportive throughout my five years of studies here in Bergen.

This page is intentionally left blank.

Contents

This page is intentionally left blank.

List of Figures

This page is intentionally left blank.

List of Tables

List of abbreviations

ADV Accoustic Doppler Velocimetry

CFD Computational Fluid Dynamics

GHG Greenhouse Gas

HVL Western Norway University of Applied Sciences

LES Large Eddy Simulation

LED Light Emitting Diodes

MR Multirotor

NTNU Norwegian University of Science and Technology

OTF Optical-Transfer-Function

PIV Particle Imaging Velocimetry

LPTV Lagrangian Particle Tracking Velocimetry

TI Turbulence Intensity

RANS Reynolds-averaged Navier-Stokes

STB Shake-The-Box

SR Single Rotor

SNR Signal-to-Noise Ratio

S47 Actuator disc with 47% solidity

S57 Actuator disc with 57% solidity

S67 Actuator disc with 67% solidity

tke turbulent kinetic energy

UN United Nations

VOI Volume of Interest

VSC Volume Self-Calibration

Chapter 1

Introduction

The world is experiencing an excelling need for an energy transition due to global warming and climate change. This is mainly caused by emissions of greenhouse gases (GHG), which are released through the combustion of fossil fuels, including oil, coal, and natural gas. Since the start of the industrial revolution, this level has increased drastically, especially during the last decades. According to Friedlingstein et al. [1], the CO_2 concentration in the atmosphere has increased by almost 50% since 1750, with more than half of this increase being traced back to the period after 1958. The subsequent environmental impact is evident. The congestion of gases emerging in the atmosphere prevents the earth from reflecting photons from the sun, contributing to the so-called greenhouse effect. In turn, this increases the global average temperature, accelerating the melting of the glaciers at the poles and raising the overall sea level. According to the National and Atmospheric Administration's yearly climate report from 2022, the global temperature has increased with an average annual value of 0.08 °C since 1880 [2]. However, since 1981 the rate of increase has more than doubled.

As a worldwide measure in handling global warming and its pressing consequences, the Paris Agreement was adopted in 2015. This international agreement aimed to lower the world's GHG emissions and limit the average global temperature increase by 2 °C, preferably not more than 1.5 °C [3]. However, if the current emission trend continues, the United Nations (UN) climate panel [4] estimates in its latest report a total increase of 3.2 °C by 2050. Furthermore, it claims that the global emission peak must be reached by 2025 to achieve the Paris Agreement's temperature objectives. A comprehensive emission cut across all sectors and a transition to

renewable energy sources are essential to accommodate these demands.

Although climate emissions continue to increase, they are happening slower than in the previous decade. The International Energy Agency [5] predicted that global CO2 emissions from fossil fuels would increase by almost 1% in 2022, a significant decrease from 2021's growth of 6%. A more comprehensive, worldwide climate policy is being pursued, showcased by the UN's sustainable development goal #7 [6], about affordable and clean energy. The objective aims to ensure access to renewable, safe, and widely available energy sources. However, further research and development related to renewable sources are crucial in replacing traditional fossil fuel sources. This means that action regarding energy sources such as wind-, wave-, solar-, geothermal-, and bioenergy are crucial for ensuring a future sustainable environment.

Wind energy has emerged as a highly promising renewable source in recent years. Transitioning from onshore to offshore wind farms has made it even more appealing due to higher wind speed potential and reduced visual impact. Additionally, floating wind technology-, and rotor design advancements are driving down the cost of offshore wind energy, making it more viable. The installed global wind capacity is constantly increasing. According to Global Wind Energy Council's Offshore Wind Report from 2022, [7], the outlook for 2030 has increased by 16.7%, giving a projected global installment of 316 GW. This ambition is also shared from a national perspective. By 2040, the Norwegian government's goal is to allocate areas for 30 GW on the Norwegian continental shelf, almost equivalent to Norway's total power production in 2022. In line with this national objective, the ministry has recently announced the first competitions for project areas in two locations, namely Sørlige Nordsjø II and Utsira Nord [8]. This act is a clear statement of intent and a pathway for the future energy transition. However, the limited availability of licensed wind farm sites poses a challenge, raising the question of how today's wind farm industry can be more cost-, energy- and area efficient. Could a multirotor-based wind farm be the solution?

1.1 Multirotor or single rotor?

The fundamental concept behind using the wind as a resource has a long history and goes back to the first sailboats in the Middle East 7000 years ago. The idea of utilizing the wind for onshore mechanical chores later developed and can be traced back to the Persians in the Middle East, who used wind power to pump water and mill grain. These first machines were based on a vertical axis with cloth sails, while crusaders introduced the horizontal-axis windmills in Europe around 1300 AD. The first dated wind turbine for generating electricity was in 1887, invented by James Blyth in northern Scotland. His design was based on a 10 m vertical axis rotor with cloth sails. Only months later, Charles F Brush, in Cleveland, Ohio, introduced the first horizontal axis wind turbine with a 12 kW, 17 m diameter rotor [9]. Since these first turbines were introduced, wind turbines have undergone massive changes in design, technology, size, and materials. Since 1975, the size of the turbines and the generated power have increased by respectively 7% and 16% annually [9]. This upscale development has been essential for meeting the continuously increasing energy demand, resulting in rotor diameters above 150 meters in the 10 MW class [10]. Figure 1.1 illustrates this upscaling trend from an offshore perspective.

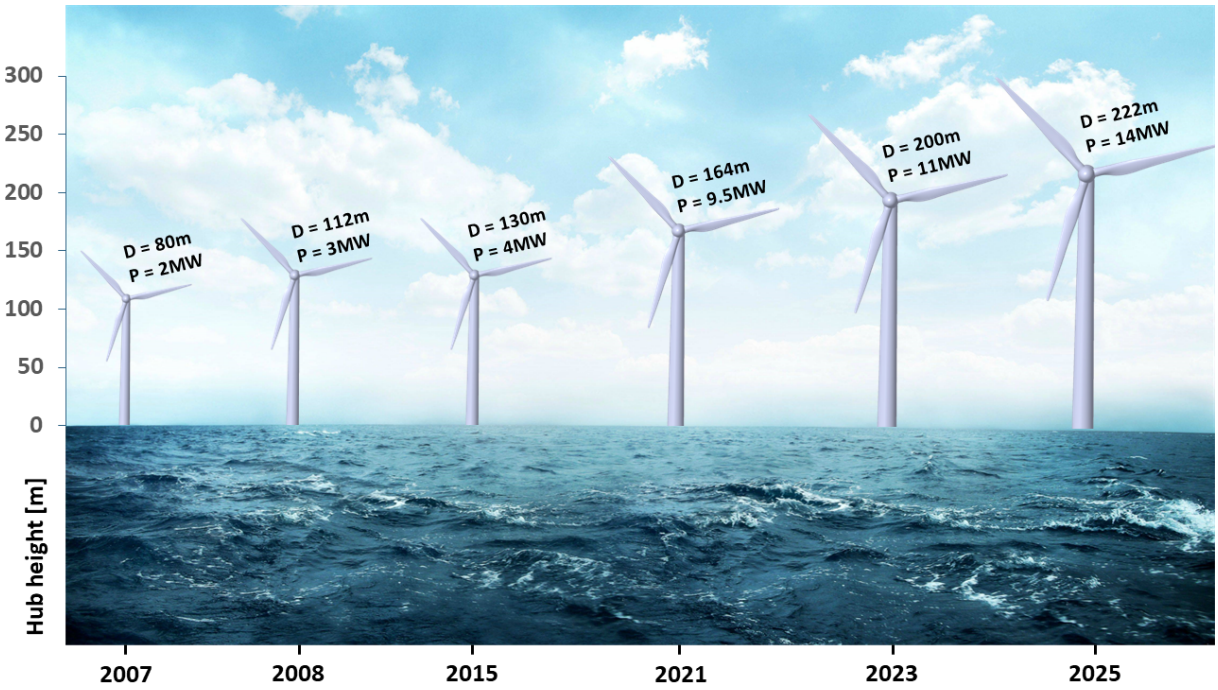

Figure 1.1: *The size and generated wind power development. Adapted from [11].*

The rotor-swept area is proportional to the power output, explaining this drastic upscale development. Key advances in blade design and material technology have enabled this size development. These advances include lighter and stiffer glass fiber- and carbon composite turbine blades, improved aerodynamic blade design, blade pitch, and rotor speed control. Despite these significant steps, the large upscale raises many challenges, such as the manufacturing process, offshore transportation, installation, maintenance, and cost. By increasing the rotor diameter, the associated mass significantly increases. This means that the energy advantages of a larger rotor size may be outweighed by the accompanying rise in mass and cost [12].

Based on these challenges, the multirotor wind turbine concept has gained more and more attention. Such a system, equipped with several smaller turbines, exploits the advantage of weight and area. Furthermore, by utilizing wake steering techniques, the multirotor wind turbine system could optimize the wake characteristics, resulting in improved wake management. The yaw angle could be adjusted for each turbine in the multirotor setup, and thereby expand, channel or redirect the wake. As a result, the application of wake steering in the multirotor configuration has the potential to reduce both wake and power losses [13],

A multirotor wind turbine could also be beneficial from a structural point of view. Compared to a conventional wind turbine, the total load would be reduced and more distributed on the whole system. Furthermore, standardization of smaller rotor components could reduce costs and simplify manufacturing, transportation, and installation, which is often more demanding in an offshore context [14]. Figure 1.2 and Figure 1.3 illustrate two different multirotor wind turbine designs, Vestas Multirotor at Risør in Denmark and the Windcatching system's multirotor, respectively. The Vestas Multirotor is a prototype used for testing, while the Windcatching system's multirotor design is still under development.

Figure 1.2: *Vestas Multirotor at Risør, Denmark [15].*

Figure 1.3: *Windcatching systems' multi-rotor design [16].*

Although the disruptive idea of the multirotor concept shows promising signs [15], little is known about complex interactions between multirotor wakes and blockage effects. Wake effects are well accounted for in an isolated wind turbine and will be reviewed in Section 2.4. Nevertheless, a multirotor-based design becomes more complex and requires more knowledge before commercializing full-scale operational multirotor systems.

1.2 Aim of thesis

Multirotor wind turbines are still a new technology concept, where no specific design has proven to be better than others. More comprehensive knowledge about blockage- and wake effects is crucial in understanding the concept's full potential. The previously performed studies in the field by Bastankhah & Abkar [17] and Ghaisas et al. [18] are mainly based on a numerical approach, where further validation through experimental investigation is necessary.

Recent studies by Skoland [19] and Koi [20] have performed an experimental approach using an Acoustic Doppler Velocimetry (ADV). This measurement instrument exploits the Doppler shift frequency concept, which enables measurements of the velocity in the wake along a single point. However, such an approach is a time-consuming process that requires multiple measurements to generate a single wake profile. A newly acquired Particle Image Velocimetry (PIV) could be more advantageous as the camera system can detect and map the flow effects more extensively. The camera system can provide more information regarding velocity deficits upstream and downstream of different multirotor configurations. By imaging a given subvolume of the flow, vortex formation can be investigated, which is impossible with an ADV.

The first aim of this thesis is to investigate how a local thrust variation influences the wake recovery process behind a multirotor turbine. The experimental research will be a parameter study performed on a single rotor (SR) and multirotor equipped with seven discs (MR7) with different cases of center disc solidities using an ADV. The second aim of this thesis is to experimentally investigate whether it is possible to accurately measure mean and turbulent quantities with the new PIV system. Hence, the ADV- and PIV results will be analyzed and compared. Figure 1.4 illustrates the experimental PIV investigation of the downstream wake of a single rotor.

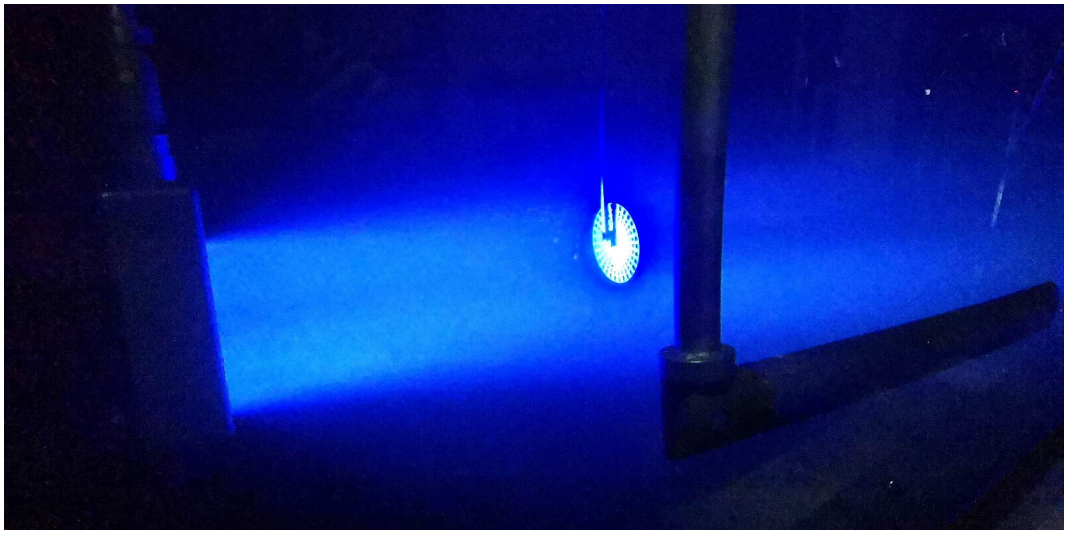

Figure 1.4: *Downstream PIV flow measurement of a single rotor wake.*

This page is intentionally left blank.

Chapter 2

Theory

The following theory chapter provides a comprehensive overview of wind power's key concepts and principles and its application in single- and multirotor wind turbines. The chapter begins by discussing wind power and the actuator disc, followed by an in-depth examination of momentum theory and its associated concepts, including the power- and thrust coefficient and the Betz limit. The chapter then delves into the specific challenges of turbine systems, including the effects of the single and multirotor wake. Additionally, the chapter explores the impact of turbulence and blockage, including isolated and row blockage. Finally, the chapter discusses model scaling and laws and reviews previous experimental research on multirotor systems.

2.1 Wind power

The wind is characterized by the movement of air masses and is a fundamental element of our natural environment. The wind masses occur due to the sun's electromagnetic radiation, leading to uneven heating of the earth. A higher temperature is present in tropical areas, while lower temperatures occur at higher altitudes. Additionally, the heating process depends on the water, rock, and soil's ability to absorb sunlight. The unbalanced heating is transformed into air motion through a convective-based process, further regulated by the earth's rotation and Coriolis effect. The wind flows from high-pressure to low-pressure areas, following circular paths toward the low-pressure center [9].

A wind turbine seeks to exploit the containing kinetic energy from the wind. In order to perform this energy extraction, the wind has to decelerate. The wind turbine only affects the wind masses that pass through it, leaving the ambient wind unaffected. Based on this assumption, a stream tube separates the approaching wind from the outside wind through a boundary layer, illustrated in Figure 2.1.

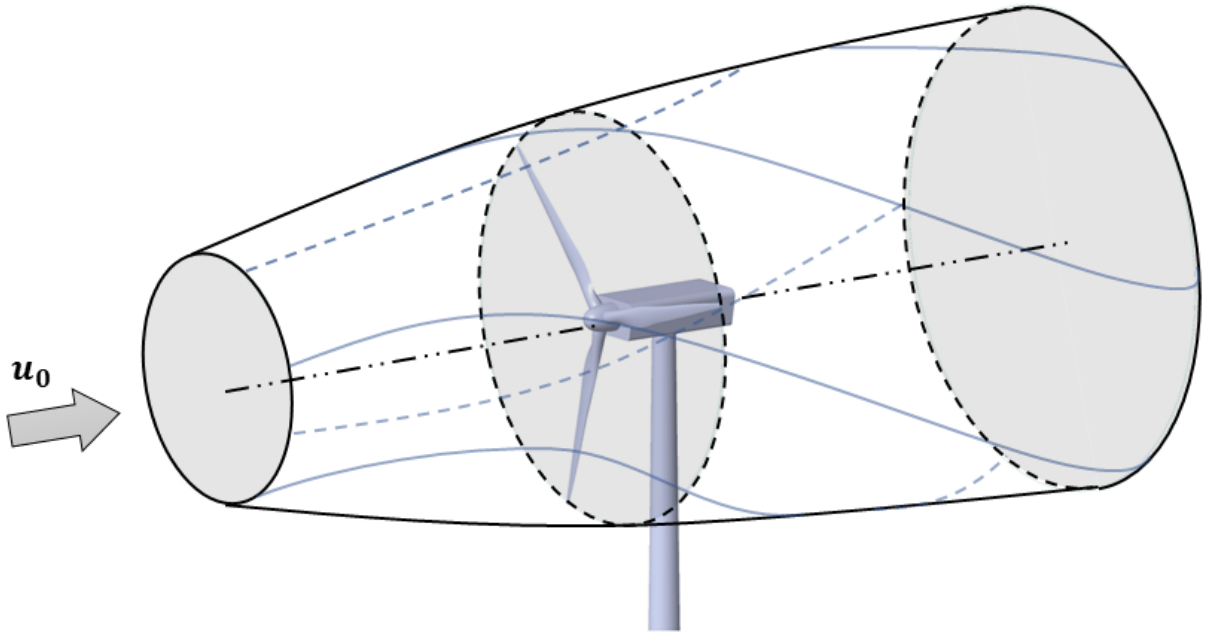

Figure 2.1: *The expanding streamtube of a wind turbine, including rotational motion of the contained air. Adapted from [9].*

The mass flow rate remains constant throughout the stream tube, as no wind crosses the boundary layer. Due to the wind masses' deceleration, the stream tube's cross-sectional area has to increase, as illustrated in Figure 2.1. As the wind passes the turbine, the rotating blades drive a generator, transforming mechanical energy into electrical energy. Equation 2.1 gives the total wind power contained far upstream in the stream tube [9].

$$P = \frac{1}{2}\rho_{air} A u_0^3, \tag{2.1}$$

where ρ_{air} is the air density, A is the rotor swept area and u_0 is the incoming wind velocity. However, it is impossible to exploit all of this power. According to the fundamental one-dimensional theory, an upper boundary limit regarding the wind power available for extraction is defined as the Betz limit. This will be further reviewed in Section 2.3.2.

2.2 Actuator disc

In 1926, Albert Betz developed a simple model for determining an idealized wind turbine's power output and thrust force. This analysis is based on the conservation of linear momentum for a given control volume. As illustrated in Figure 2.2, the rotor swept area is represented by an actuator disc, a hypothetical surface containing an infinite number of blades. As the flow bypasses the surface, energy is extracted. The model is further based upon the following assumptions: There is no frictional drag, and the fluid flowing is incompressible, homogenous, and steady. The acting thrust force is uniform over the disc surface, while no rotational motion is present in the downstream wake. Additionally, the ambient static pressure far upstream and downstream is identical [9].

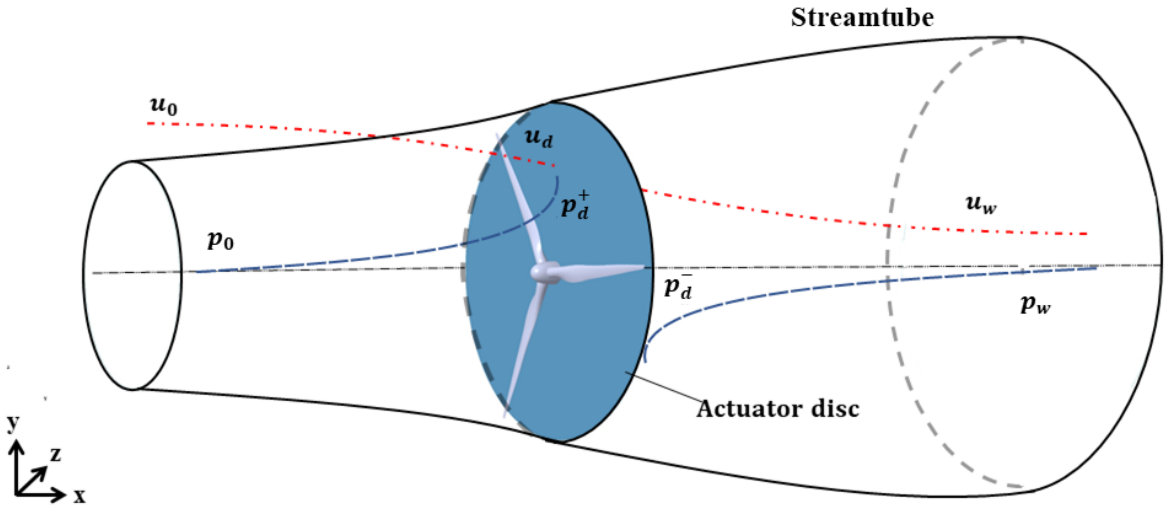

Figure 2.2: *The pressure and velocity drop over an actuator disc. Adapted from [9].*

The resulting pressure drop over the static actuator disc will be derived based on these fundamental assumptions. As previously reviewed, the actuator disc expands the cross-sectional area of the stream tube. Consequently, air mass flow must remain the same at any given point along its path. Hence, Equation 2.2 summarizes the mass flow conservation.

$$\rho_{air} A_u u_u = \rho_{air} A_d u_d = \rho_{air} A_w u_w \tag{2.2}$$

The letters u, d, and w refer to conditions far upstream, at the disc, and far downstream, respectively. As the wind approaches the actuator disc, it slows down. A common way of describing this velocity deficit is by the axial induction factor, a. This factor is defined as

the fractional decrease of the incoming velocity, u_0. Consequently, the velocity in the plane occupied by the disc, u_d, can be written as presented in Equation 2.3.

$$u_d = (1-a)u_0 \tag{2.3}$$

2.3 Momentum theory

The wind that passes the actuator disc experiences a rate of change of momentum that is dependent on the drop in velocity, $u_0 - u_w$ [9]. Thus, Equation 2.4 yields.

$$\text{Rate of change of momentum} = (u_0 - u_w)\rho_{air} A_d u_d \tag{2.4}$$

The force that drives the momentum change rate is entirely driven by the pressure difference, Δp. Thus, Equation 2.5 yields.

$$\Delta p A_d = (u_0 - u_w)\rho_{air} A_d u_0 (1-a) \tag{2.5}$$

The pressure drop, Δp, is given by the immediate pressure difference between each side of the actuator disc, $p_d^+ - p_d^-$. Bernoulli's equation is used separately for each side of the occupied disc area to obtain this pressure difference. This well-known equation states that the resulting pressure, kinetic energy, and gravitational potential remain constant, given that the fluid does no additional work. Hence, Equation 2.6 can be applied.

$$\frac{1}{2}\rho_{air} u_0^2 + p + \rho_{air} g h = \text{Constant} \tag{2.6}$$

Thus, by using this equation on either side of the disc in Figure 2.2, the total pressure drop can be expressed as shown in Equation 2.7.

$$\Delta p = p_d^+ - p_d^- = \frac{1}{2}\rho_{air}(u_0^2 - u_w^2), \tag{2.7}$$

By implementing this expression in Equation 2.5, Equation 2.8 is obtained.

$$\rho_{air} A_0 u_0^2 = \rho_{air} A_w u_w^2 + p A_r = \rho_{air} A_w u_w^2 + \frac{1}{2} \rho_{air} A_r (u_0^2 - u_w^2) \tag{2.8}$$

Based on this relation, the velocity in the disc plane can be written as expressed in Equation 2.9.

$$u_d = \frac{1}{2}(u_0 + u_w) \tag{2.9}$$

By asserting the expression for the velocity in the disc plane, Equation 2.3, in the above equation, the velocity in the wake can be derived as shown in Equation 2.10.

$$u_w = (1 - 2a) u_0 \tag{2.10}$$

2.3.1 The power and thrust coefficient

The one-dimensional theory ultimately provides expressions for the acting thrust force on the disc area and its associated power extraction. Based on Equation 2.5, an expression for the thrust force, F_T, that acts on the wind can be introduced as given in Equation 2.11:

$$F_T = \Delta p A_d = 2 \rho_{air} A_d u_0^2 (1 - a) \tag{2.11}$$

Due to the force being concentrated on the actuator disc, its rate of work is $F_T u_d$. As a result, the amount of power extracted from the air is provided by Equation 2.12.

$$P = F_T u_d = 2 \rho_{air} A_d u_0^3 a (1 - a)^2 \tag{2.12}$$

Consequently, an expression for the power coefficient can be defined, given in Equation 2.13:

$$C_p = \frac{P}{\frac{1}{2} \rho_{air} u_0^3 A_d} \tag{2.13}$$

Similarly, the thrust coefficient, C_T, can be obtained. The thrust force, caused by the pressure drop over the disc, is previously given by Equation 2.11. The thrust coefficient is then:

$$C_T = \frac{P}{\frac{1}{2}\rho_{air} u_0^2 A_d} \tag{2.14}$$

The power and thrust coefficient, from Equation 2.13 and Equation 2.14, can further be expressed as a function of the axial induction factor, a. This is summarized in Equation 2.15 and Equation 2.16.

$$C_T = 4a(1-a) \tag{2.15}$$

$$C_P = 4a(1-a)^2 \tag{2.16}$$

2.3.2 Betz limit

The Betz limit is defined as the maximum achievable power coefficient. It can be obtained by computing the derivative of the power coefficient, C_P, from Equation 2.16, with respect to the axial induction factor, a. When this expression equals zero, the maximum value of C_P occurs, highlighted in Equation 2.17.

$$\frac{dC_p}{da} = 4(1-a)(1-3a) = 0 \tag{2.17}$$

The maximum limit occurs when the axial induction factor has a value of $a = \frac{1}{3}$. Thus, Equation 2.18 yields.

$$C_{P\,max} = \frac{16}{27} = 0.593 \tag{2.18}$$

The Betz limit is further illustrated in Figure 2.3, which shows the thrust and power coefficients, C_T, and C_P as a function of the axial induction factor, a.

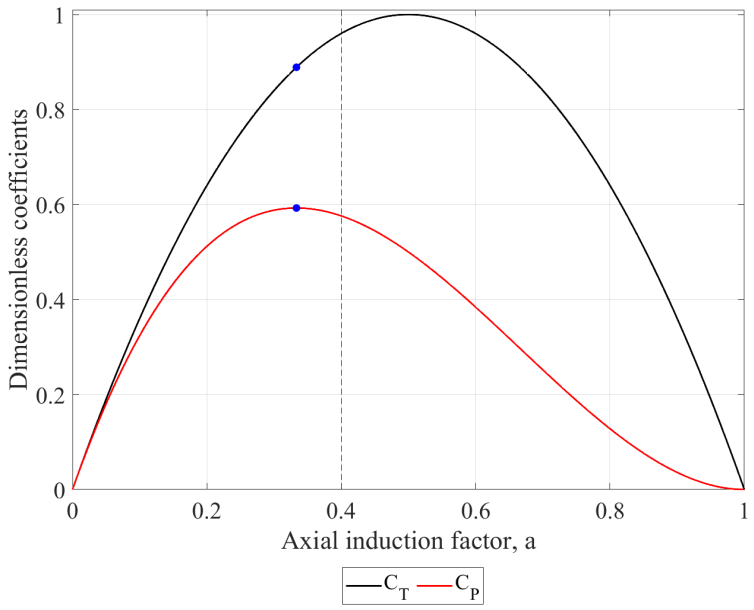

Figure 2.3: *The thrust- and power coefficient as a function of the induction factor a, illustrating the Betz limit. As the induction factor exceeds a value of a = 0.4, momentum theory brakes down due to high blockage. Figure adapted from [9].*

No power or thrust is generated at the zero point due to the free stream velocity being unaffected. The thrust and power coefficients increase with the increasing induction factor. The power curve reaches it's maximum value at $a = \frac{1}{3}$, giving a maximum $C_p = 0.593$, as given in Equation 2.18. This equation explains the upper limit regarding how much power theoretically can be harvested from the wind. At this given induction factor, the thrust coefficient equals $C_T = 0.89$. High thrust loading is therefore predicted at an optimized power harvest and needs to be considered during the planning and development of the aerodynamic blade design. As the induction factor passes a value of 0.4, high blockage occurs, and the theory becomes invalid.

2.4 Single rotor wake

A wind turbine extracts the kinetic energy from the wind, and a generator transforms the mechanical energy into electrical energy. This extraction process causes an immediate velocity deficit in the downstream wake. Additionally, increased turbulence occurs. The reduced energy downstream for an isolated wind turbine does not affect its power output. However, these flow effects can have comprehensive consequences from a wind farm point of view. Turbines located downstream will be influenced by the wake characteristics generated from the upstream turbine, potentially causing a power reduction and fatigue loading. According to Barthelmie et al., [21], the average power loss due to the downstream wake constitutes about 10-20% of the total power output in an offshore located wind farm. Hence, it is crucial to identify the wake flow characteristics to minimize this power loss. These characteristics are summarized in Figure 2.4.

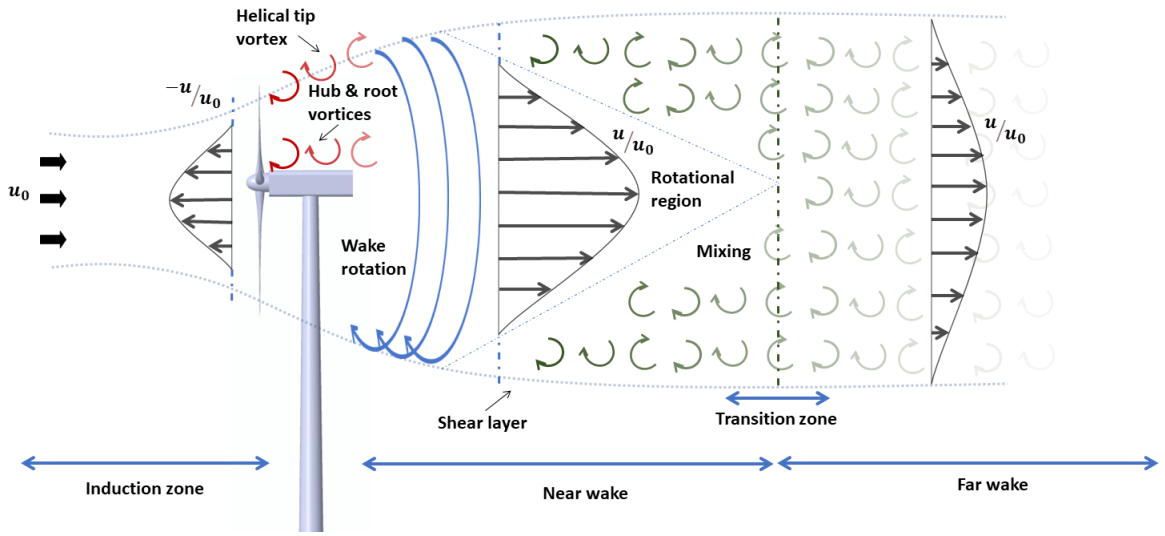

Figure 2.4: *Downstream wake characteristics of a single rotor wind turbine. Adapted from [22].*

As the figure illustrates, the wake of a wind turbine can be further separated into a near wake and a far wake. In the near wake region, stretching from 1-2D, tip and hub vortices are present. These formations mainly depend on the wind turbine's geometrical characteristics, such as the aerodynamic blade profile, hub, and nacelle. The vortex structures appear as periodic helicoidal formations caused by the blade's pressure difference between the suction and the pressure side [23].

The tip and hub vortices play a pivotal role in the behavior and stability of a wake system. Dobrev et al. [24] investigated the wake flow behind a three-bladed horizontal axis wind turbine with a diameter of d = 0.5 m using a PIV system in a wind tunnel. Their experimental study revealed that the tip vortices expanded in a radial direction. Moreover, the vortex core radius remained constant with age, slowly decreasing its tangential velocity. Howard et al. [25] investigated the influence of hub vortices on wake development also using a PIV. The vortex oscillations contributed to the tip vortices' instability and the overall wake system. The hub vortices can interact with other vortices, causing a meandering motion of the wake. In turn, this can impact a wind turbine's energy production and structural loading.

As the flow moves further downstream, the wake structure expands due to pressure gradients. Eventually, the flow reaches the far wake, which is less dependent on the geometrical characteristics of the turbine. Along the width of the wake, a shear layer is present. This contradicts the actuator disc theory that assumes that the free stream velocity is fully separated from the wake. However, the difference in velocity from the inside and outside wake creates an expanding shear layer. The generated turbulence in the wake contributes to mixing the flow velocities of either side of the shear layer. The velocity deficit decreases as the flow moves further downstream until it fully recovers very far downstream [23].

According to a recent study by Van der Laan et al. [26], the main mechanism behind the recovery process of a wake system is the shear stresses, specifically the lateral shear stress $u'v'$ and the vertical shear stress $u'w'$. Their results were obtained using Large Eddy Simulation (LES), which is a Computational Fluid Dynamics (CFD) approach used to model and simulate turbulent flows. The simulations were conducted on a single rotor turbine under atmospheric conditions. The divergence of these shear stresses was found to play a crucial role in the recovery of the wake.

2.5 Multirotor wake

The previous research on multirotor wind turbine wakes is primarily based on a numerical approach. According to Bastankhah & Abkar's study [17], the multirotor wake just behind the rotors can be considered individual wakes associated with each rotor in the configuration. As the wake moves further downstream, the individual wakes will interact and eventually merge into a single wake, as illustrated in Figure 2.5. Xiong et al. [27] conducted a wind tunnel experiment based on an MR4, with an equivalent inter-rotor spacing as Bastankhah & Abkar 's[17] of $s = 0.1D$. The individual wakes were found to be drawn against each other due to an unequal transfer of momentum on each side of the wake. Before the individual downstream wakes merge, a high-velocity gap flow is present between the rotors. Additionally, tip vortices appear for each rotor. Due to the interacting wakes, the appearing tip vortices experience faster destruction, contributing to a faster wake regeneration. Simultaneously, the gap flow decays before disappearing prior to the merging process [27].

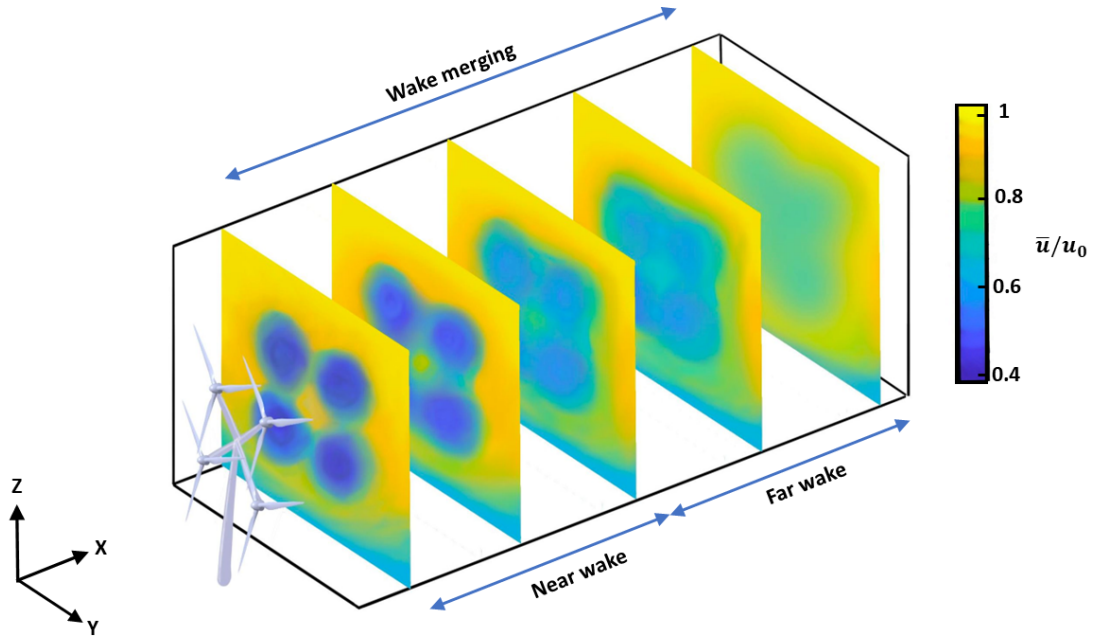

Figure 2.5: *The wake merging from near to far wake in the downstream of a rotor configuration of four rotors, MR4. Adapted from Bastankhah and Abkar [17].*

The downstream velocity, turbulence, and transition length in the multirotor wake were found to be dependent on different parameters, such as rotor size, rotor number, inter-rotor spacing, and rotation. These findings will be covered in more detail in the following four sections.

2.5.1 Inter-rotor spacing

The distance between the rotors in a multirotor setup is crucial for how the wake develops. This finding from Bastankhah & Abkar [17] contradicts Ghaisas et al. [18] study with a large inter-rotor spacing, where they concluded that the inter-rotor spacing had a low impact on the near and far wake. However, Bastankhah & Abkar [17] studied this in more detail, based on a CFD analysis with a more realistic value for the tip clearance. The simulation results showed that an increased spacing between the rotors led to a lower velocity deficit in the near wake. This occurrence was due to a postponement in the transition from the individual, localized wake areas to the single wake further downstream. They additionally implemented a mathematical model for describing the transition length, depending on the inter-rotor spacing, resulting in Equation 2.19:

$$\frac{L_T}{d} = \frac{1}{k}(\frac{1+\frac{s}{d}}{2.2} - \epsilon), \tag{2.19}$$

where L_T is the transition length, d is the rotor diameter, k is the wake growth rate, s/d is the inter-rotor spacing, and ϵ is the normalized, initial width of the wake. This proposed mathematical model was found to predict the transition length for MR wakes accurately, given various inter-rotor spacing. [17].

The numerical results from Bastankhah & Abkar related to the inter-rotor spacing's effect on the wake are consistent with recent experimental research at Western Norway University of Applied Sciences (HVL)[19, 20, 28]. This will be further reviewed in Section 2.9.

2.5.2 Rotor size

Bastankhah & Abkar [17] further investigated how the rotor diameter influenced the wake recovery. This was done by comparing the normalized velocity deficits for four different SR diameters, with $D_n = D/\sqrt{n}$. Their LES-based results showed that the lesser the diameter, the faster the initial wake recovery. However, this is due to the streamwise location being much further downstream for a smaller turbine with respect to its rotor diameter. The four individual curves coincide into a single curve by further normalizing the downstream distance with respect to its corresponding diameter, such that $X = x/D_n$. Hence, the rotor size was

found not to be crucial for the development of the wake.

2.5.3 Rotor number

The number of rotors in the MR configuration is also essential for understanding how the wake develops. In Bastankhah & Abkar's study [17], CFD simulations were performed for an isolated turbine and different MR setups. A rotor configuration equipped with one, two, four, and seven rotors, now referred to as SR, MR2, MR4, and MR7, were studied and compared for an inter-rotor spacing of $s = 0.1d$. The results showed that an increased number of rotors led to a lower velocity deficit in the near wake region up to a distance of $x = 4D$. However, the resulting difference is most significant between SR and MR2 as well as between MR2 and MR4. The difference in the normalized velocity deficit was only marginal for an additional increment in the rotor number. Further downstream, the curves representing the velocity deficits stabilize at the same downstream distance.

2.5.4 Rotor rotation

For a single rotor, the rotational effect only appears in one direction. On the contrary, a multirotor configuration could consist of multiple rotors turning in different directions. Bastankhah & Abkar [17] examined whether such an induced rotor rotation could influence the development of the downstream wake. Their numerical investigation was based on the idea that the generated swirl motions from the rotors could force the bypassing flow into the same channeled wake (passage), thereby enhancing the regeneration of the wake velocity. By varying the rotational speed of an MR4, the effect was analyzed. However, the results showed that the rotational movements and the subsequent swirls had a negligible impact on the wake regeneration. Nonetheless, more research could be necessary to analyze different rotor configurations based on various inter-rotor spacing and the number of rotors.

2.6 Rotor wake turbulence

A flow can be separated into two categories, laminar and turbulent. In a laminar flow, the flow particles retain their relative position through successive cross-sections in a highly ordered manner. On the contrary, a turbulent flow is characterized by a more chaotic motion. The flow particles' movement and relative position in successive cross sections are more unpredictable

than a laminar flow, with the particles moving randomly in 3 dimensions. These unordered motions cause slight fluctuations in their mean velocity and pressure values at a given point in the streamwise location [29].

The turbulence generated from an upstream wind turbine greatly impacts the development of a downstream wake. Higher turbulence enhances a higher mixing between the boundary layers, excelling the recovery of the velocity deficit [15]. According to Bastankhah & Abkar [17], the turbulence intensity in the wake is less significant for an MR than an SR. This could be advantageous from a wind farm point of view, where increased turbulence causes a higher fatigue loading, reducing the lifetime of a wind turbine. Moreover, the generated turbulence can shorten the transition time from the localized, individual wakes to the merged, single wake. However, the wake turbulence also depends on the incoming flow's turbulence level. Given a high turbulence inflow, the advantages related to the MR configuration's wake recovery become less significant, as stated by Skoland [19].

The turbulence level can be expressed as either turbulence intensity (TI) or turbulent kinetic energy (tke). The TI is the intensity of the velocity component's fluctuations and is given in Equation 2.20.

$$TI = \frac{u_{rms}}{U} \tag{2.20}$$

where u_{rms} is the average velocity fluctuations of the time series N, further expressed in Equation 2.21.

$$u_{rms} = \sqrt{\frac{1}{3}((u')^2 + (v')^2 + (w')^2)} \tag{2.21}$$

and U is given by Equation 2.22:

$$U = \sqrt{\bar{u}^2 + \bar{v}^2 + \bar{w}^2} \tag{2.22}$$

Here $\bar{u}$, $\bar{v}$, and $\bar{w}$ is the averaged value for each of the three velocity components.

Moreover, the turbulent kinetic energy can be defined as the average variance value of the velocity components, as given in Equation 2.23.

$$tke = \frac{1}{2}((u')^2 + (v')^2 + (w')^2) \tag{2.23}$$

The individual velocity components are defined as the difference between the instantaneous velocity and the mean value.

In this thesis, the turbulence level will be expressed as tke/u_0^2, such that this parameter is normalized by the incoming velocity. Thus allowing a standardized, dimensionless comparison of the downstream wake of different multirotor setups.

2.7 Upstream blockage

As the wind approaches the wind turbine, the upstream velocity reduces while some of the wind gets diverted. This phenomenon is commonly known as the blockage effect. In order to obtain more knowledge about wind farms and potential MR layouts, more comprehensive knowledge about this topic is necessary. According to recent studies by Bleeg et al., [30], the average upstream velocity of three different wind farm sites was reduced by 3.4% at an upstream distance of two rotor diameters. As a result, the front row of a wind farm layout produces less energy than an isolated wind turbine, indicating that the well-known wake approach is inadequate. Consequently, this could lead to overestimating energy production [30].

The reviewed impact on power production is negative from a "normal" single rotor wind farm point of view. However, according to Forsting et al. [31], the blockage effect could be advantageous by controlling parameters such as inter-rotor spacing and rotor number for a multirotor setup. These conditions are also considered when designing tidal turbines in a channel, and a parallel could therefore be drawn to multirotors. Hence, the following two sub-sections will examine this impact for both an isolated turbine and a row of turbines. Additionally, critical design parameters which are decisive for power production will be reviewed. By analyzing these factors, optimizing power production for multirotor wind

turbines may be possible.

2.7.1 Isolated blockage

The blockage effect for a conventional wind farm layout or a multirotor setup is analogous to a tidal turbine in a channel. Garrett & Cummins [32] performed a study on the blockage effect in a channel for a single tidal turbine, where relevant definitions are illustrated in Figure 2.6.

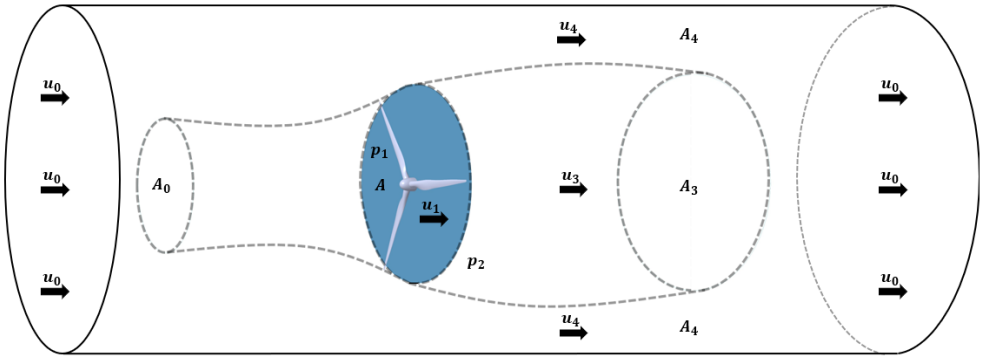

Figure 2.6: *Definitions of a single tidal turbine in a channel [32].*

By considering the definitions and relations from Figure 2.6 and linking it up with the one-dimensional theory, Garrett & Cummins derived an expression for the resulting power output. This is summarized in Equation 2.24.

$$P = 2(1-\epsilon)^{-2} A u_3 (u_0 - u_3)^2, \tag{2.24}$$

where ϵ is the blockage ratio expressed as $\epsilon = \frac{A}{A_C}$. Compared to the power output for the ideal actuator disc in Section 2.2, an extra efficiency of $(1-\epsilon)^2$ occurs. This is due to the increased pressure build-up caused by the channel boundaries. The total power output possible to extract for an actuator disc is determined by the Betz limit, previously given in Equation 2.18. Equivalently, the tidal turbine's maximum power is obtained at the same induction factor of $a = \frac{1}{3}$, giving a velocity of $u_3 = \frac{1}{3}u_0$. Hence, the maximum power for a single rotor in a tidal channel is:

$$P_{max} = \frac{16}{27}(1-\epsilon)^{-2}\frac{1}{2}Au_0^3 \tag{2.25}$$

2.7.2 Array blockage

In the case of multiple lateral wind turbines, the force distribution and velocity deficit become more complex. This is due to the interacting blockage effect among the neighboring turbines. Forsting et al. [31] studied this effect from a Reynolds-averaged Navier-Stokes (RANS) based numerical perspective, which is a mathematical model used in CFD to simulate fluid flows. This approach was used to analyze the upstream flow and its effect on power production. A lateral row consisting of five turbine rotors with a spacing of three rotor diameters was studied by varying the angle of the incoming wind speed from 0-45°. Both of the methods used had an agreeable trend. Due to the induced blockage effect, the overall power production tends to increase with an increasing flow angle. Compared to an isolated turbine, the increase in power was 1-2% larger. Although the interacting effect from the upstream flow seems encouraging, turbulence may arise, potentially causing fatigue loadings.

The research from Forsting et al. [31] clearly illustrates how a lateral row of turbines causes the wind to slow down. Furthermore, it is interesting to consider this blockage effect from a theoretical point of view. According to the research of Garrett & Cummins [32], the efficiency and corresponding power increased for an isolated tidal turbine in a channel, with an increasing blockage ratio. This also corresponds with Nishino & Willden's study [33], further expanding the existing model from an isolated turbine to a lateral row of turbines. Correspondingly, the turbine row is located in a blocked channel. This proposed mathematical model is based on the definitions illustrated in Figure 2.7.

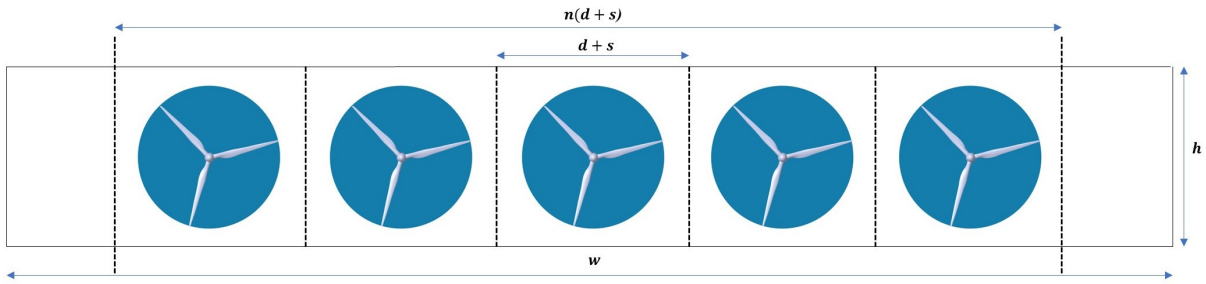

Figure 2.7: *A row of n tidal turbines located in a w wide channel. Adapted from [33].*

The model is based on three different blockage ratios: array-, local- and global blockage, denoted as B_A, B_L, and B_G, respectively. The array blockage is defined as the ratio between the

array of turbines and the channel area. The local blockage is the ratio between a single turbine and a given cross-section. The global blockage is the ratio between the turbines and the whole channel area. These non-dimensional blockage ratios are summarized in Equation 2.26.

$$B_G = \frac{\pi}{4\frac{h}{d}\frac{w}{nd}}, \quad B_L = \frac{\pi}{4\frac{h}{d}(1+\frac{s}{d})}, \quad B_A = \frac{1+\frac{s}{d}}{\frac{w}{nd}} \tag{2.26}$$

Here h is the channel height, w is the channel width, d is the rotor diameter, n is the rotor number, and s is the inter-rotor spacing. Compared to the isolated turbine model from Garrett & Cummins [32], previously illustrated in Figure 2.6, multiple stream tubes are now present. This is further presented in Figure 2.8.

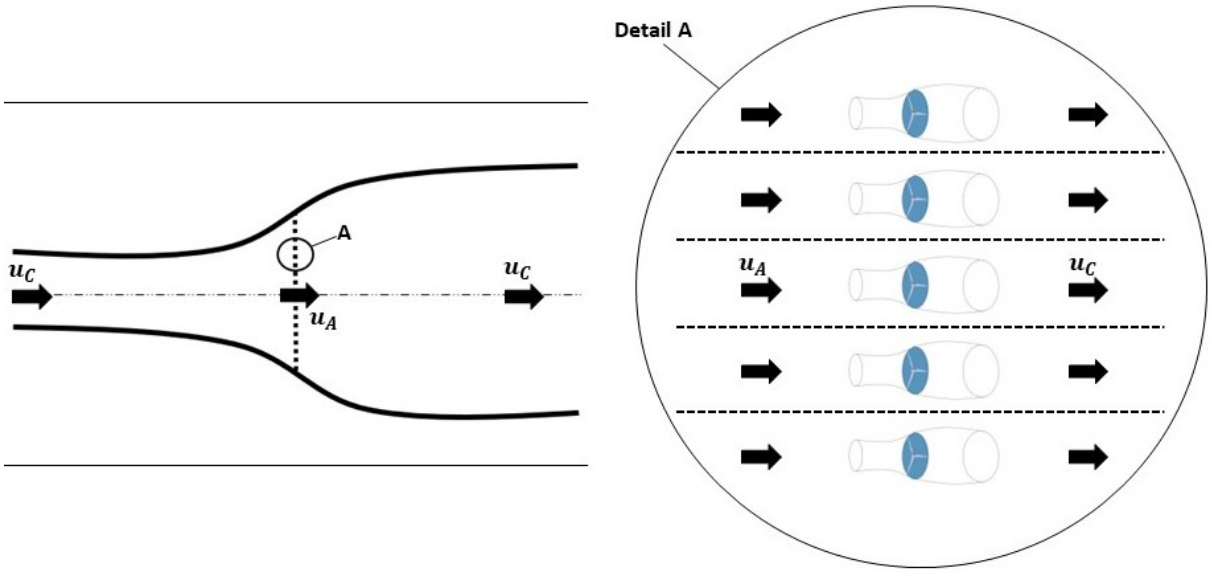

Figure 2.8: *Array- and individual stream-tubes. Adapted from [33].*

A flow expansion and mixing appear at an array scale and individual scale. The mixing zone, wake generation, and interacting jet streams become more complex than for an isolated case.

What is particularly interesting and relatable to multirotors is how the efficiency is affected when the row of turbines is placed in an infinitely wide channel, $w/nd \to \infty$. The global power coefficient then becomes solely dependent on the local blockage. The coefficient reaches a maximum value of $C_{PG} = 0.798$ at a local blockage ratio of $B_L = 0.785$, exceeding the Betz

limit of $C_P = 0.593$. However, a further increase in the local blockage decreases the power coefficient.

2.7.3 Blockage in fences

As previously reviewed in Section 2.7, the increased blockage effect in a channel leads to an increment of the rotor's pressure gradient and thrust force. Hence, the power coefficient also increases. Different studies have been performed to analyze how the proposed model from Garret & Cummins [32] applies to different rotor configurations in light of the different number of rotors, inter-rotor spaces, and blockage ratios. Vogel & Willden [34] investigated how the increased blockage effect influenced the power performance for both a single turbine and a row of four horizontal turbines in a channel, based on a RANS numerical approach. The turbines were closely spaced in a cross-stream fence, with an equal local blockage ratio of $B_L = 0.196$ and $B_L = 0.0507$. Although the power coefficient was found to be below the theoretical limit demonstrated by Garrett & Cummins [32], the achieved power coefficient of $C_P = 0.739$ and $C_P = 0.529$, respectively, for the single rotor case surpassed the well-known Betz limit. As for the four-rotor case, the flow interactions between the lateral turbines led to a lower C_P for the higher blockage simulation and a higher C_P for the lower blockage simulation. A value of $C_P = 0.535$ for the inner turbines and $C_P = 0.528$ for the outer turbines was achieved for the higher blockage case. This difference is because the row of four turbines is placed in the broader channel with a global blockage ratio of $B_G = 0.0507$. Thus the pressure gradient and thrust force are reduced compared to the single rotor case. However, by adjusting the pitch angle, an increment of 6% of the power coefficient could be achieved. Thereby the lift and drag ratio along the span of the rotor blades was optimized.

Schluntz & Willden [35] also studied how the local blockage affects a tidal turbine configuration's power performance in an indefinitely wide channel. The analysis was based on a RANS-BEM optimization tool to design a turbine setup with a maximum power effect. The performed simulations were based on four different domains, where the blade solidity, σ, and the characteristic distance between the rotors, s/d, for each domain, is illustrated in Figure 2.9.

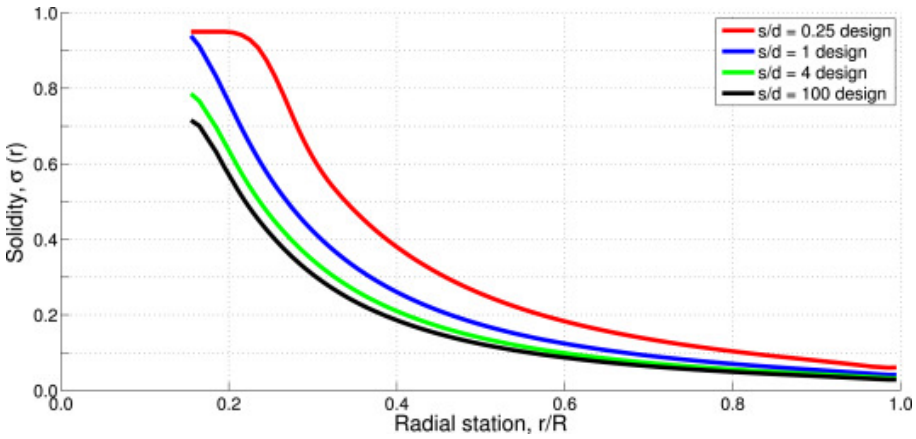

Figure 2.9: *A blade solidity comparison for the different rotor designs [35].*

The simulation results showed that the highest effect occurred for the domain with the highest local blockage of $B_L = 0.25$ with an inter-rotor spacing of $s = 0.314d$. This gave a theoretical power coefficient of $C_P = 1.259$, while the simulations showed a power coefficient of $C_P = 1.10$. In other words, the simulations gave consistency with the theoretical foundation for the effect with the blockage taken into account. The difference between the values was mainly due to a loss in viscosity during the simulation process. Schluntz & Willden [35] concluded that the highest maximum efficiency was obtained for the design with the highest local blockage ratio. A higher blade solidity and lower blade twist angle were required for the blades to operate under these blockage conditions while obtaining maximum efficiency.

Zhu et al. [36] optimized a turbine design with respect to parameters such as cord length and pitch angle distribution. Based on this algorithm optimization, it was concluded that the pitch angle distribution should be optimized for each airfoil, thereby maximizing the lift-drag ratio along the span of the blade. Additionally, the primary location of the power generation was found to be at 75% of the span of the blade. Thus, expanding the cord length in the middle part of the blade was conducive to catching more energy from the water flow and further improving the turbine's power coefficient. Based on their specific design, a gain of 2% of the power coefficient was achieved.

Wimhurst & Willden [37] presented two tidal turbine designs, one operating in unblocked conditions and the other operating in blocked conditions. The latter was placed in an infinite tidal fence with a local blockage of $B_L = 0.197$. and a tip-to-tip spacing of 1D. Both

computed turbine designs achieved their maximum power at a tip-speed ratio close to 5. Furthermore, increasing the power coefficient could be achieved by increasing the thrust force. This could be done for the blocked condition design by increasing the blade solidity. As for the unblocked condition design, a significant increase in the tip speed ratio became necessary.

Based on the above-reviewed studies, it becomes clear that a specific rotor designed for blocked conditions shows promising signs. A multirotor must consider many of the same parameters under a design procedure, such as local blockage, blade solidity, chord length, and twist angle. For multirotors, this is especially important for the center turbine in an MR7 setup, which will experience a higher blockage effect by the surrounding lateral turbines.

2.8 Model scaling

The majority of research on multirotor wakes and blockage effects has relied on numerical methods, as demonstrated by studies such as Bastankhah & Abkar [17] and Ghaisas et al. [18]. However, it is essential to conduct experimental research to validate these previous findings and to improve current and future simulation tools. This will ultimately lead to greater agreement across different approaches and increased reliability of the resulting data. Several full-scale experiments have been conducted on full-scale wind farms [38, 39, 40]. Although these physical measurements are crucial for gaining a deeper understanding, full-scale experiments are often impracticable due to their high cost and complexity of manufacturing. Additionally, these methods can be quite time-consuming. As a result, a simplified, down-scaled experimental approach is needed. These procedures are based on fundamental scaling laws, which state that the simplified models are only representative if certain conditions are met. These conditions include geometric-, kinematic-, and dynamic similarity [41].

Geometric similarity is a term used in model-scaled experiments to describe the relationship between the physical characteristics of a model and its corresponding full-scale prototype. It refers to the fact that the ratio of any two corresponding linear dimensions of the model and prototype are equal or similar. This means that if a model is scaled down by a factor of λ, the ratio of any linear dimension in the model to the corresponding dimension in the prototype is $1/\lambda$ [41]. The geometric similarity is important in model-scaled experiments

because it ensures that the forces, velocities, and other physical phenomena experienced by the model are proportionally the same as those experienced by the prototype. This allows for accurate predictions and simulations of the full-scale prototype's behavior based on the model experiments' results. As for this experimental campaign, the area of the down-scaled actuator disc must be scaled correctly for the swept area of the full-scale rotating turbine. Correct model dimensions can, for example, be obtained through 3D printing, later explained in Section 3.1.3 and 3.1.4.

Kinematic similarity means that the flow conditions must be the same. This requirement can be challenging because a turbulent flow surrounds the full-scale object while a laminar flow surrounds the model. However, similar turbulent characteristics can be obtained by implementing a turbulence grid in the physical experiments, as previously shown by Skoland [19].

Dynamic similarity means that different force ratios between the model and the full-scale device must be the same. However, as different force ratios require different model velocities, this requirement can only partially be fulfilled. A model test dilemma arises, where experimentalists must make compromises and prioritize certain aspects of the model testing to achieve the best possible results. Nevertheless, the most important force ratio criteria for downscaled wind turbine experiments in a towing tank or a wind tunnel is the Reynolds number, Re, given in Equation 2.27.

$$Re = \frac{\rho L u_0}{\mu} = \frac{L u_0}{\nu} \tag{2.27}$$

where L is the lenght of the model, u_0 is the model velocity, and ν is the kinematic viscosity. For a wind turbine, the length of the model corresponds to the rotor diameter, d. One common issue is the requirement for an unrealistically high model velocity to match the Reynolds number of the full-scale device. For instance, the company Mingyang Smart Energy is presently manufacturing the MySE 16-260 offshore wind turbine, with a rotor diameter of d = 260 m and a power of P = 16 MW [42]. Assuming an altitude of h = 200 m, Table A-16 from [43] gives a dynamic viscosity of $\mu = 1.783 \cdot 10^{-5}$ kg/m·s and a air densitiy of $\rho_{air} = 1.202 \text{kg/m}^3$. Given a rated wind speed of u_0 = 12 m/s, Equation 2.27 gives a Reynolds number of $Re = 210 \cdot 10^6$.

Table 2.1 shows the velocity requirements to match this Reynolds number from an experimental point of view. Note that the values for the dynamic viscosity and density for fresh water, μ and ρ_{water}, are taken from the International Towing Tank Commission's freshwater table [44] given a measured temperature of $T = 16°C$ in the tank. The values for these conditions in the wind tunnel are again taken from Table A-16 [43], now at an assumed altitude of $h = 0$ m.

Table 2.1: *The required model test velocities in a towing tank and wind tunnel to match the Reynolds number of Re = 210·10^6, for MySE 16-260 offshore wind turbine. Values for μ taken from ITTC [44] and Table A-16 from [43]. Calculations based on Equation 2.27.*

Parameter	**Full-scale**	**Towing tank**	**Wind tunnel**
Re [-]	$210 \cdot 10^6$	$210 \cdot 10^6$	$210 \cdot 10^6$
μ **[kg/m·s]**	$1.783 \cdot 10^{-5}$	$1.108 \cdot 10^{-3}$	$1.789 \cdot 10^{-5}$
ρ **[kg/m^3]**	1.223	998.946	1.225
d [m]	260.0	0.2	0.2
u_0 **[m/s]**	12	1164	15334

Such model velocities are unachievable. However, experimental research has shown that the thrust coefficient becomes independent of the Reynolds number once it exceeds a value of 1000 [45], shown in Figure 2.10. Note that both C_T and C_D describe the normalized axial force on the rotor or disc. While C_T is often used for rotating devices such as turbines, C_D is mainly used for static objects.

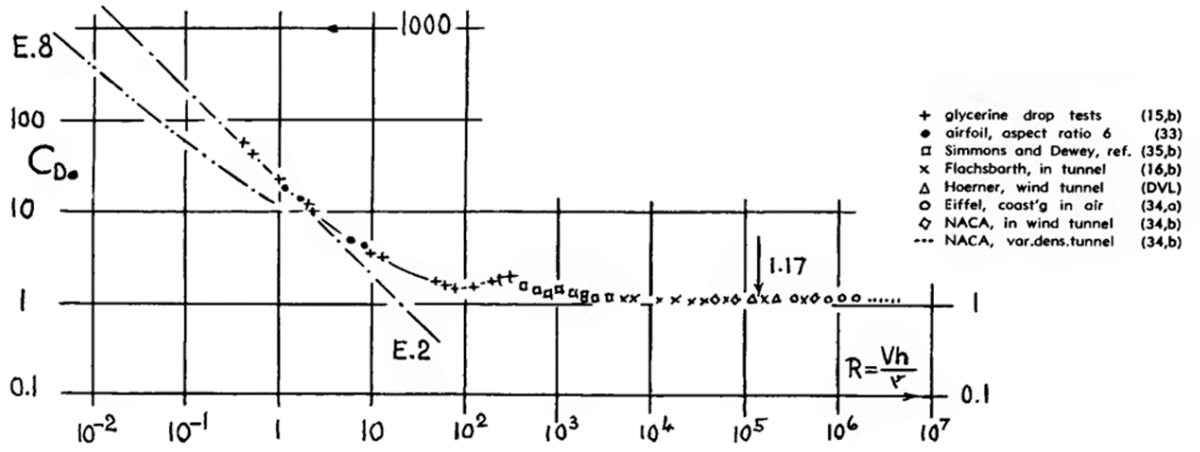

Figure 2.10: *Thrust coefficient for circular and square plates as a function of Reynolds number [45].*

As Figure 2.10 illustrates, the thrust coefficient becomes independent of the Reynolds number beyond a certain threshold. Therefore, using a more suitable model velocity is possible

while still achieving the same flow behavior and turbulence intensity as the full-scale device. Thus enabling more practical model tests while maintaining the critical aspect of dynamic similarity.

The thrust coefficient C_T can be found theoretically and is dependent on the resistance coefficient κ, which is related to the disc porosity Φ. This relation is based on Taylor's equation, given in Equation2.28 [46]:

$$\Phi^2 = \frac{1}{1+\kappa}. \tag{2.28}$$

The porosity factor Φ of the static disc used in the experiment can be expressed as $\Phi = A_{open}/\mathrm{A}_{total}$. The theoretical thrust coefficient can then be calculated by Equation 2.29.

$$C_T = \frac{\kappa}{(1+\frac{\kappa}{4})^2}. \tag{2.29}$$

The solidity of the discs used in the experimental campaign is $s = 47\%$, $s = 57\%$, and $s = 67\%$, hereby denoted as S47, S57, and S67. Based on these parameters, a theoretical thrust coefficient and thrust force can be calculated. Table 2.2 presents an overview of these values.

Table 2.2: *Theoretical thrust coefficient, C_T, based on Taylor's equation [46].*

Solidity [-]	**Porosity** [-]	k [-]	C_T [-]
0.47	0.53	2.560	0.952
0.57	0.43	4.408	0.998
0.67	0.33	8.183	0.882

Based on these calculations of the thrust coefficient, C_T, a thrust force, F_T, can be calculated using Equation 2.30.

$$F_T = \frac{1}{2}\rho_{water} A_{disc} u_0^2 C_T \tag{2.30}$$

where ρ_{water} is the densitiy in fresh water, A_{disc} is the total area of the disc and u_0 is the towing velocity. During the experimental campaign, a towing velocity in the range of $u_0 = 0.5 - 1.0$ m/s was used. Furthermore, a temperature of $T = 16$°C was measured in the towing tank. Hence, according to ITTC' properties for fresh water [44], the density is

ρ_{water} = 998.946 kg/m^3 and the dynamic viscosity is μ = 1.108·10^{-3} m^2/s. Based on these values, Re and F_T can be theoretically calculated, as presented in Table 2.3.

Table 2.3: *The theoretically calculated thrust force, F_T, for each towing velocity. Re calculations based on Equation 2.27.*

		F_T **[N]**		
Towing velocity [m/s]	**Re [-]**	**S47**	**S57**	**S67**
0.5	$9.015 \cdot 10^5$	3.734	3.914	3.460
0.6	$10.818 \cdot 10^5$	5.377	5.636	4.983
0.7	$12.621 \cdot 10^5$	7.318	7.671	6.782
0.8	$14.424 \cdot 10^5$	9.559	10.019	8.859
0.9	$16.226 \cdot 10^5$	12.098	12.680	11.212
1	$18.029 \cdot 10^5$	14.935	15.654	13.842

Based on these calculations, the thrust force and thrust coefficients experience a drop if the solidity keeps increasing. Whether this is physical or not will be reviewed in Section 4.1.

2.9 Previous experimental research of multirotor systems

The previous numerical-based studies on multirotor have given encouraging results. However, an experimental approach is essential for validating and optimizing existing software. Several experimental multirotor studies have been performed at MarinLab at HVL. Jørs & Mjåtveit [28] investigated MR wake characteristics using different MR configurations in terms of rotor spacing and number. The experiments were conducted with an ADV based on laminar inflow conditions. Results showed that an increased number of rotors greatly influenced the flow characteristics, especially in the near wake region. Jet streams located in between the rotors led to a faster wake regeneration with a lower velocity deficit compared to an SR. Further downstream in the far wake region, the differences were smaller. The inter-rotor spacing also greatly impacted the wake development. An increased spacing caused higher mixing in the near wake region, causing a lower velocity deficit and a faster transition from the individual wakes to the uniform wake.

Skoland [19] also performed MR-related experiments in MarinLab, based on SR, MR4, MR7, and MR19. A comparison between SR- and MR wakes revealed that the latter had initially lower velocity deficit and turbulence levels in the near wake. However, as the wakes progressed downstream, the SR wake recovered faster and exhibited lower velocity deficits in the

far wake at $x = 10D$. Furthermore, the study investigated how turbulent inflow conditions affected the wake. Results showed that different inflow conditions had a low impact on the wake generation for an MR7. However, exposing an SR with a higher turbulent inflow gave a higher velocity deficit. Additionally, the effect of inter-rotor spacing and rotor number was investigated. When the inter-rotor spacing increased from $0.0d$ to $0.1d$ and $0.4d$, the velocity deficit decreased in the near wake region. The tightest spacing resulted in the highest velocity deficit in the far wake, agreeing with the findings from Jørs & Mjåtveit [28]. When increasing the rotor number, the velocity deficit and turbulent kinetic energy decreased in the near wake region. However, further downstream, a higher number of rotors revealed a higher velocity deficit in the far wake, indicating a slower wake recovery.

Another critical aspect of the multirotor system is the blockage effect. Koi [20] investigated how this effect influences the force distribution and induction zone based on an MR7 design, using the same inter-rotor spacing variations as Skoland [19]. By using a load cell, the acting thrust force was measured for different setups. Based on her findings, she concluded that the thrust force and distribution are highly reliant on the local blockage ratio. The wake expands as the local blockage increases and a higher velocity deficit is obtained in the upstream induction zone.

The highest gain in thrust force occurred for the tightest spacing and the highest local blockage, resulting in a 19.4% increase compared to a single rotor disc. From a force distribution point of view, the disc in the configuration's center experiences a higher thrust coefficient than the discs at the edges. However, the local blockage ratio is not only determined by the spacing parameter. The porosity of the actuator discs also plays a vital role. By adjusting the porosity of the center disc, the force distribution can be controlled and balanced. Nonetheless, the question of how this porosity adjustment affects the velocity in the induction zone and wake must be highlighted.

This page is intentionally left blank.

Chapter 3

Methodology

This methodology chapter will review the experimental setup, measurement instruments, measurement procedures and associated uncertainties and errors.

3.1 Experimental setup

In these first following subsections the experimental setup will be presented, including the test facility and 3D disc construction.

3.1.1 Test facility

Traditionally, wind turbine experiments are conducted in wind tunnels. However, Reynolds scaling allows us to perform similar experiments underwater. Due to its higher density, water moves more slowly than air at the same velocity. This slower movement can make it easier to detect and visualize particle movements and fluid flow patterns using instruments such as ADV and PIV, which measure fluid velocities and visualize fluid flow patterns. Hence, the measurement campaign was performed at MarinLab at the Western Norway University of Applied Sciences. This test facility consists of a combined towing and wave tank with dimensions of 50x3x2.2 m, illustrated in Figure 3.1.

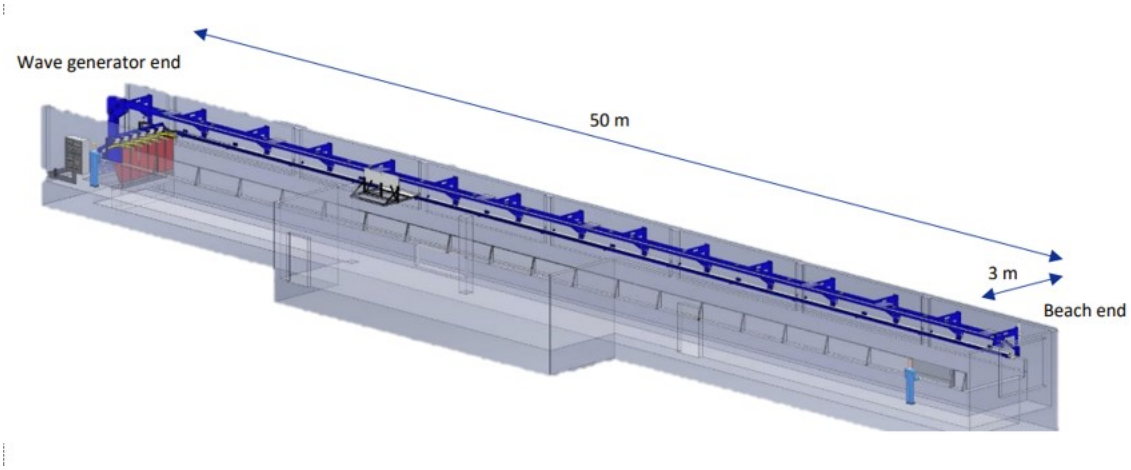

Figure 3.1: *MarinLab at HVL, the test facility for the measurement campaign [47].*

The towing tank is equipped with a wave generator and a towing carriage. The wave generator can generate waves with a maximum wave height of $h = 0.5$ m, while the carriage can be towed with a maximum velocity and acceleration of $u = 5$ m/s and $a = 1.3$ m/s^2, respectively [47]. The wave generator is equipped with six hinged force-feedback-controlled wave paddles, enabling attenuations of the tank's wall reflections. On the opposite side of the tank, an exponentially porous, profiled beach absorbs the breaking waves with a minimum reflection. The test facility can be used for model-scale testing and analysis of ships, offshore structures, floating rigs, mooring systems, underwater and autonomous vehicles, and hydrodynamic interactions [47].

The submerged multirotor system will be attached to a moving carriage in this towing tank above the waterline. A LabVIEW program further controls the carriage system. Contrary to a wind tunnel, the measured object moves relative to the flow. The differences and similarities between these measurement techniques will be reviewed in Section 3.1.2. The measurement system, either an ADV or a PIV, is further attached to a second carriage behind the multirotor setup. These two carriages move at the same velocity, while the distance between them is manually controlled, depending on the downstream area of interest.

3.1.2 Porous disc

The complexity and cost of installing rotating turbines for model-scale experiments are often very high and demanding. Hence, a simplified rotor model can be an effective solution. In-

stead of using these actual rotating turbines, the experiments will be conducted on simplified, porous discs. Such a porous disc representation, also known as an actuator disc, is simpler and cheaper to manufacture. However, this approach must be distinguished from the idealized turbine, reviewed in Section 2.2, because the fundamental assumptions behind the theoretical concept, such as non-friction, are invalid. The representative discs are manufactured with a design that resembles an actual rotating turbine's thrust force and diameter.

Helvig et al. [48] studied the wake flow upstream and downstream of a rotating two-bladed turbine and compared it to different porous discs based on design, hole geometry, and solidity. This experiment's objective was to identify the optimal disc design that closely resembles the thrust force of the turbine and flow characteristics in its wake. The measurement campaign was conducted by a PIV in a wind tunnel at the Norwegian University of Science and Technology (NTNU). Results showed that a radially trapezoidal-based hole geometry with a porosity of 35% corresponded the most with the rotating turbine regarding velocity field and vortex formations in the wake. However, the characteristic tip vortices for a rotating turbine are not present in the wake of the actuator discs.

The solidity of the discs used in this experiment campaign is 57%, illustrated in Figure 3.2. However, according to Koi [20], the upstream blockage effect leads to a higher thrust force on the actuator disc located at the center of a multirotor configuration. In order to control this force distribution, the center disc will be studied with a solidity of $\pm 10\%$, offering better insight into the acting forces and their effect on wake recovery.

Figure 3.2: *Porous discs used in the measurement campaign, arranged in an MR7 setup.*

Moreover, Garnes et al. [49] studied the upstream blockage effect and the downstream wake based on a single, isolated disc. This disc is identical to the one used in this experiment. Furthermore, the results from the velocity reduction in the wake were compared to a similar case performed in the wind tunnel at NTNU. Results from the comparison are illustrated in Figure 3.3.

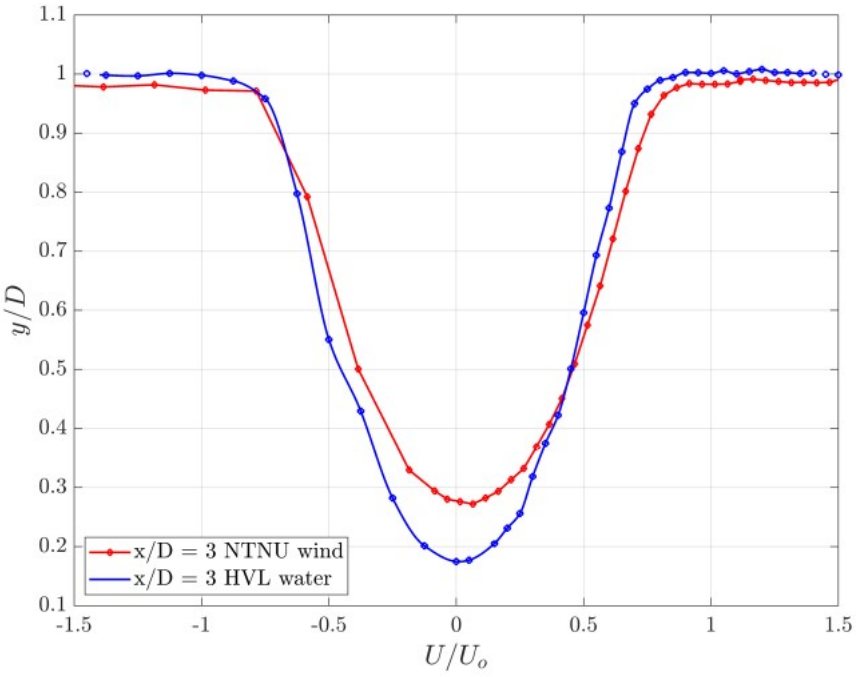

Figure 3.3: *Comparison between the velocity reduction for a wind tunnel- and a towing tank-based experiment [49].*

The findings indicate that the velocity reduction is slightly higher in experiments conducted in a towing tank due to differences in the inlet flow conditions. The wind tunnel had a low inflow turbulence level of $TI = 0.3\%$ in the upstream region, while the towing tank had completely laminar flow conditions of $TI = 0.0\%$. A turbulence grid could be used to account for these differences, as done by Skoland [19].

3.1.3 Support structure

The support structure of the multirotor design, which was originally created by Hansen et al. [50], and Jørs & Mjåtveit [28], consists of three main parts, a center joint, corner joints, and slender steel rods. Using Creo Parametric, the joints were modeled and converted to a Stereolithography file. This file was then uploaded to the flashprint program called Flash Force Adventure 3 before the joints were 3D printed based on a Polylactic Acid (PLA) material. Figure 3.4 and 3.5 illustrate an overview of the joints.

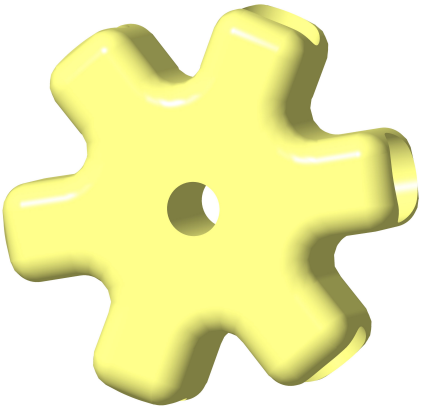

Figure 3.4: *Center joint [50].*

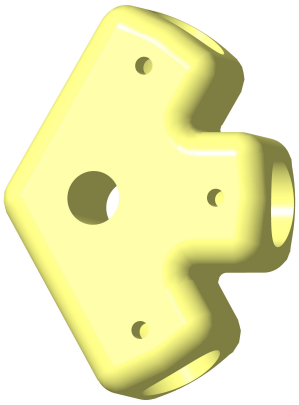

Figure 3.5: *Corner joint [50].*

The slender rods connecting the joints have a diameter of d = 10 mm. The hexagon-based frame structure consists of six corner joints, one center joint, and 12 steel rods. Figure 3.6 further fully illustrates the support structure.

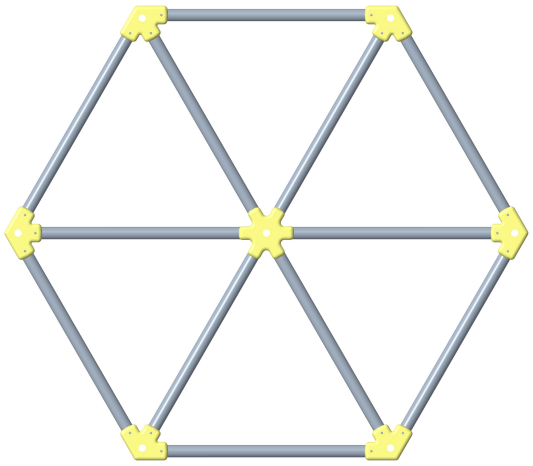

Figure 3.6: *Hexagonial support structure [50].*

3.1.4 Multirotor configurations

In order to validate previous experimental results from the ADV-based measurement technique, a similar experimental approach is necessary. By doing so, similarities across the measurement techniques can be identified while providing further details on the upstream and downstream wake flow. Thus, the experimental campaign will be conducted on an MR7 configuration, accordingly to the previous studies performed by Skoland [19] and Koi [20]. A inter-rotor spacing of $s = 0.1d$ will be applied, with a rotor disc diameter of d = 0.2 m.

Next, the local blockage ratio, B_L, needs to be introduced. Based on Nishino & Willden [33], the blockage ratio is defined as $B_L = \frac{A_d}{A_c}$, where A_d is the area of the actuator disc, and A_c is the area of an associated local channel from which individual discs extract momentum. Koi [20] used a quadratic channel area as a reference. However, by doing so, a portion of the surrounding discs will appear in the same channel area, which was not considered. Thus, in this thesis, a hexagonal channel area is introduced, avoiding any overlap between the rotors in the different channel areas. Figure 3.7 illustrates how the multirotor was divided into seven equal isolated channel regions. As shown in Table 3.1, a "solid" disc blocks about 75% of the hexagonal channel area.

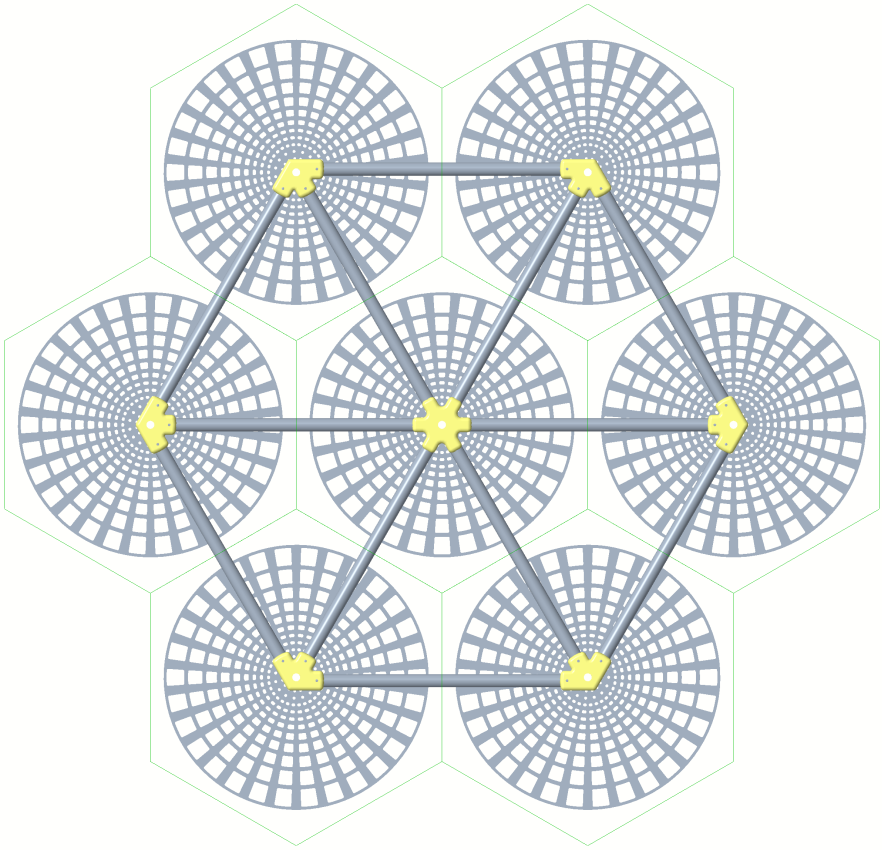

Figure 3.7: *MR7 setup with an inter-rotor spacing of* $s = 0.1d$.

Table 3.1: *Local blockage ratio,* B_L*, for a "solid" disc in a hexagonal channel.*

Area channel $[m^2]$	**Area disc** $[m^2]$	**Local blockage**
0.042	0.031	0.749

The solidity of the discs is 57% for the baseline setup. However, the upstream blockage effect leads to an increased thrust force on the disc located at the configuration's center. In order

to account for local blockage effects and to achieve a more balanced force distribution, the solidity of the center disc will be adjusted. The hole pattern follows the same trapezoidal shape but is scaled with a different factor. An illustration of the three different center discs follows in Figure 3.8.

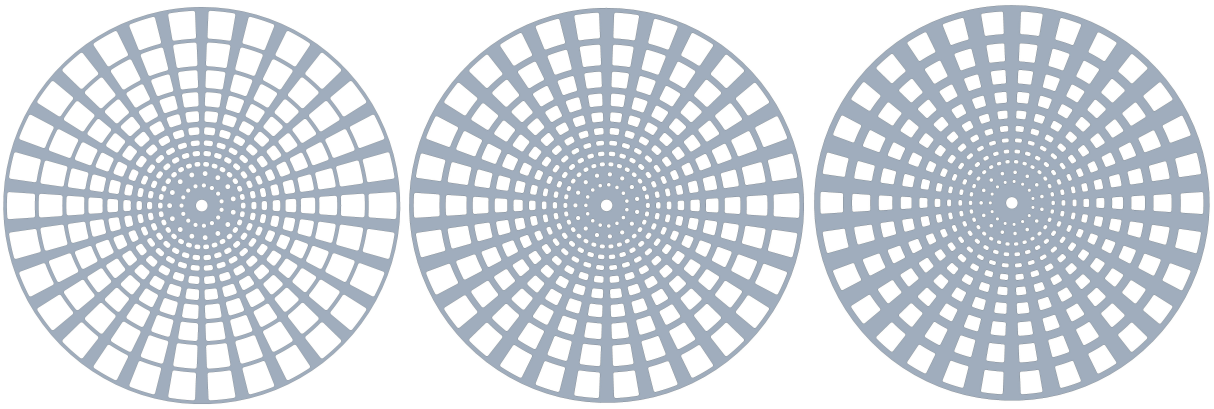

(a) *47%* ***(b)*** *57%* ***(c)*** *67%*

Figure 3.8: *The different center discs: S47, S57 and S67.*

Furthermore, Figure 3.9 shows the radial variation of the center disc's solidity. In terms of thrust, the radial variation in disc solidity can be regarded to correspond to rotor blade solidity, as previously shown in Figure 2.9, or a fixed rotor geometry operated at different rotational speeds.

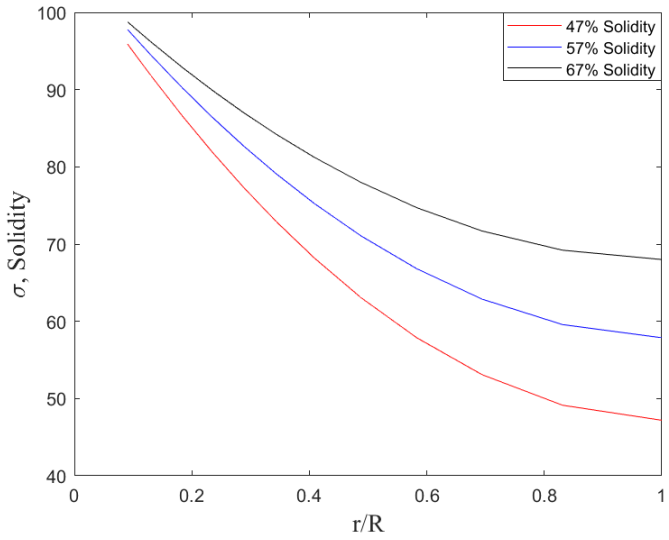

Figure 3.9: *Radial distribution of the different disc's solidity.*

The local blockage ratio, B_L, will be considered from an isolated disc perspective, with an equally big disc area, as previously presented in Table 3.1. However, the solidity of the center

disc in the multirotor configuration will also be a contributing parameter in terms of the resulting thrust force, upstream induction zone, and downstream wake. Hence, the blockage ratio and the associated center disc solidity will now be combined into a common parameter, as presented in Table 3.2.

Table 3.2: *Total local blockage ratio, B_{TL}, solidity weighted, for the three porous discs.*

Disc solidity	**Area channel [m^2]**	**Area disc[m^2]**	**Total local blockage [-]**
S47	0.042	0.015	0.352
S57	0.042	0.018	0.427
S67	0.042	0.021	0.502

As shown in the table, the effective total solidity now decreases from 75% to 35-50%, depending on the disc design. Hence, it will be interesting to analyze the wake development and wake recovery based on these different solidity and local blockage ratios.

3.2 Load cell

A 100N HMB load cell measured the axial thrust force acting on the SR based on the different disc solidities. This instrument contains resistive strain gauges that sense the applied force through strain and compression. The strain gauge's resistance, ΔR, changes based on the resulting strain. This change is further described by Equation 3.1 [29].

$$\Delta R = \left(\frac{\partial R}{l}\right)\delta l + \left(\frac{\partial R}{A}\right)\delta A + \left(\frac{\partial R}{\rho}\right)\delta l \tag{3.1}$$

where l is the length of the gauge element, A is the cross sectional area and ρ is the resistivity. A strain gauge is characterized by its Gauge factor, defined as the fractional change in resistance $\Delta R/R_0$ divided by the applied strain, e. The Gauge factor can also be expressed as shown in Equation 3.2:

$$\frac{\Delta R}{R_0} = Ge \tag{3.2}$$

Nevertheless, when the force is exerted, the strain gauges undergo deformation, resulting in a corresponding change in electrical resistance. This change in resistance is then measured using a Wheatstone bridge configuration. By analyzing the output voltage signal from the

Wheatstone bridge, a proportional relationship with the applied force is established [29]. The load cell employed in this experiment demonstrates linearity, wherein the measured force can be calculated using Equation 3.3.

$$y = kI + a \tag{3.3}$$

where k is the rate of increase and a is the offset value. The parameters k and a of this linear equation were obtained by calibrating the load cell. For this purpose, five known weights were applied to the load cell in ascending order before being subsequently unloaded in the opposite order. The registered output from the load cell was noted for each applied load. Based on these numbers, a best-fit line was applied to the data, giving a linear relationship as shown in Equation 3.3. Table 3.3 presents the data from the calibration procedure.

Table 3.3: *The worksheet from the calibration procedure of the load cell.*

Applied load O(I), [N]	**Measured output I, [mV/V]**	**Calculated load y, [N]**	**Non-linearity N(I), [N]**
Increasing load			
-0.032	-0.037	0.411	0.447
18.307	-0.374	18.937	0.630
36.332	-0.701	36.875	0.543
54.222	-1.024	54.604	0.382
72.451	-1.354	72.686	0.235
90.269	-1.675	90.339	0.070
Decreasing load			
80.505	-1.495	80.420	-0.085
61.757	-1.146	61.311	-0.446
39.501	-0.736	38.764	-0.738
21.025	-0.400	20.324	-0.701
-0.037	-0.022	-0.394	-0.358

The first two columns from Table 3.3 present the output value from the load cell in mV/V given the applied load in N. Based on these values, a best-fit line was obtained, with a gain value of k = -54.878 and an offset value of a = -1.603. Hence, the basis for the calculations of the third column. Furthermore, the load cell can be checked for non-linearity, defined as the difference between the actual and idealized lines, expressed in Equation 3.4 [29].

$$N(I) = O(I) - kI + a \tag{3.4}$$

Here, $O(I)$ is the actual line, while $kI + a$ is the idealized line, previously given in Equation 3.3. This difference is presented in the fourth column of Table 3.3. The non-linearity can be further expressed as a percentage of the total capacity of the load cell, further illustrated in Figure 3.10.

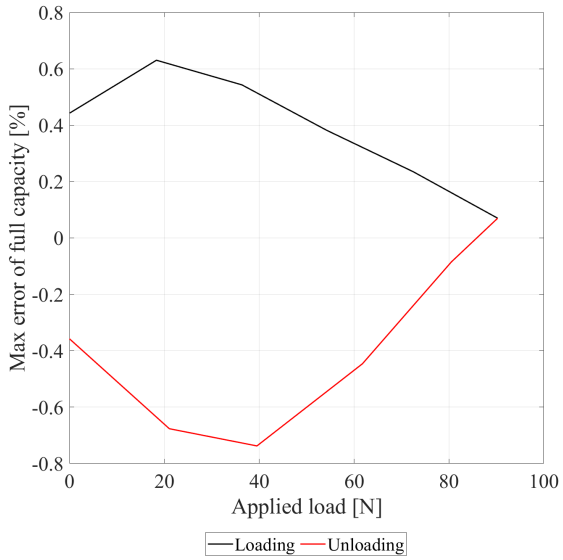

Figure 3.10: *The max error in percentage of the total output range for the load cell.*

An absolute maximum non-linearity was found to be N_{max} =0.74%. Furthermore, the hysteresis, defined as the difference in output value given loading and unloading conditions, can be calculated using Equation 3.5 [29].

$$H(I) = O(I)\uparrow - O(I)\downarrow \tag{3.5}$$

Here, $O(I)\uparrow$ is the output value when the load increases, while $O(I)\downarrow$ is the output value when the load decreases. By interpolating the curves under loading and unloading conditions, a maximum hysteresis as a percentage of the total capacity of the load cell was found to be $H_{max} = 0.2\%$. Both the non-linearity and the hysteresis were relatively low throughout the experimental campaign.

3.3 Acoustic Doppler Velocimetry (ADV)

This study first measured the fluid flow velocity using Nortek's four-beam ADV, the Vectrino+. The ADV is a type of Doppler velocimeter that uses the Doppler effect to measure fluid velocity. It works by emitting a high-frequency acoustic signal into the fluid and measuring the frequency shift of the reflected signal [51]. The velocity of the fluid can be calculated using Equation 3.6:

$$f_{doppler} = -f_{transmitter} * \frac{u}{c} \tag{3.6}$$

Here, the $f_{doppler}$ is the frequency of the Doppler-shifted signal that is received by the ADV, $f_{transmitter}$ is the frequency of the signal emitted by the ADV transmitter, u is the velocity of the fluid and c is the speed of sound in the medium through which the acoustic signal is traveling. The four receiving transducers of the ADV, illustrated in Figure 3.11, are configured in a rectangle, with the transmitting probe in the middle. An acoustic signal is emitted by this transmitting probe in a focused volume of height and diameter of $h = 3$ mm and $d = 6$ mm, respectively. The signal is then reflected by the suspended particles in the water volume before being registered by the four transducing beams. The ADV outputs the fluid velocity in each of the three measurement directions in the Vectrino+ software [51].

Figure 3.11: *The Vectrino+ velocimeter from Nortek [51].*

In addition, the ADV uses a built-in temperature sensor to correct the effect of temperature on the sound speed in the fluid. However, this temperature sensor was broken, and a manual temperature correction was necessary to implement during the post-processing phase, later described in Section 3.7.2.

To obtain accurate measurements, the ADV is dependent on a sufficient mixing of the particles. These seeding particles, recommended by Nortek [51], are glass spheres with a diameter of $d = 10\,\mu m$. These tiny particles act as reflectors, providing the necessary signal for the ADV to detect and analyze. Furthermore, an important parameter for evaluating data quality in the ADV is the Signal-to-Noise Ratio (SNR). SNR quantifies the signal level relative to the background noise and is measured in decibels (dB). Equation 3.7 expresses this relation:

$$SNR = 20log_{10}\frac{S_A}{N_A}, \tag{3.7}$$

where S_A is the signal amplitude and N_A is the noise amplitude [51]. Higher SNR values indicate a stronger signal than the noise, which ensures more reliable velocity measurements. Hence, the mixing procedure of the suspended particles in the tank was crucial for obtaining higher SNR and will be further reviewed in Section 3.5.3.

Furthermore, some of the key specifications of the Vectrino+ ADV are presented in Table 3.4.

Table 3.4: *Technical specifications for the Vectrino+ velocimeter from Nortek [51].*

Component	**Technical specifications**	
Vectrino+ ADV	Sampling rate	1-200 Hz
	Accuracy	± 5% of measurement value
	Height of sample volume	3 mm
	Diameter of sample volume	6 mm
Mixing particles	Particle type	Sphere-shaped glass (Neutrolly bouyant)
	Diameter	10 µm

The ADV was used to measure the fluid velocity of SR and MR7, both from an upstream and downstream perspective. The measurement procedure will later be presented in Section 3.5.2.

3.4 Particle Image Velocimetry (PIV)

The Particle Image Velocimetry (PIV) system used in this thesis is a brand-new volumetric Lagrangian Particle Tracking Velocimetry (LPTV) developed by LaVision. It consists of the underwater MiniShaker multi-camera and a Lightning Emid Diode (LED) illumination source. The captured images were post-processed and analyzed using the Shake-The-Box (STB) module in LaVision's integrated software, DaVis 10. This STB module is based on a 4D Lagrangian technique, capable of identifying the 3D positions of particles and tracking their motion over time. By analyzing image sequences, the STB module accurately traces the tracer particles' trajectories throughout the flow field [52]. This post-process will be further reviewed in Section 3.6.3. An illustration of the MiniShaker multi-camera and the LED source is presented in Figure 3.12.

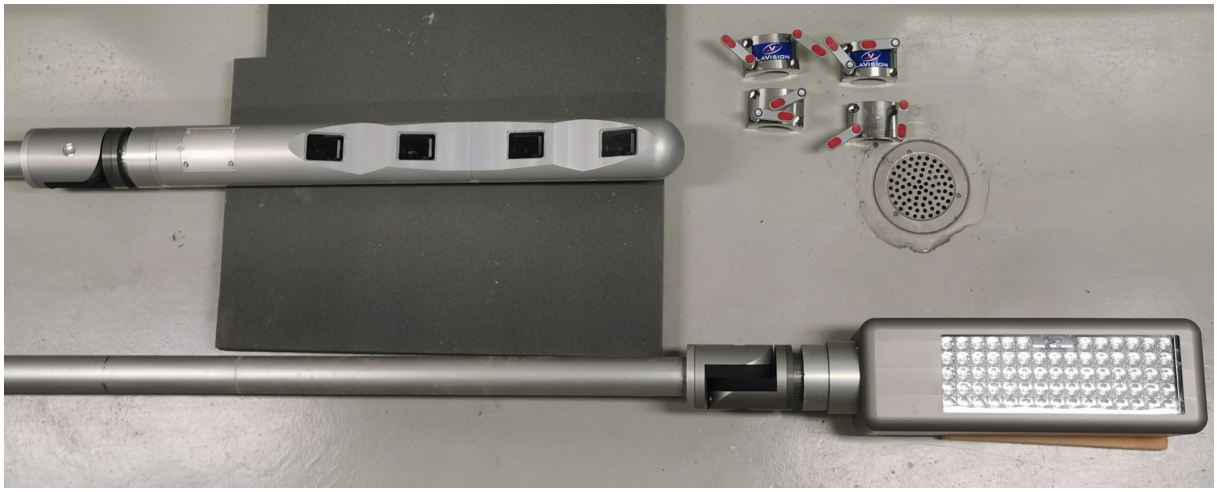

Figure 3.12: *LaVision's PIV system, including Minishaker multi-camera and LED flashlight 300 [53].*

The submerged MiniShaker multi-camera consists of 4 cameras, each with a resolution of 896x656 pixels. Furthermore, the cameras can capture images at 8- or 10-bit, with a maximum frame rate of 510 fps [52]. In this thesis, the camera frequency was set to 150 Hz, with a camera exposure time of 338 µs. The recording was manually started as the towing carriage reached a constant velocity of u = 0.5 m/s, avoiding the acceleration- and deceleration phases.

A steel housing with length of l = 700 mm protects the camera system and is further attached to a rod guiding all the cables above the waterline. Traditionally, PIV measurements are

performed based on laser illumination. However, recent advancements have made LED more appealing due to cost-efficiency, size, durability, brightness, and flexibility. Additionally, LED illumination is safer than laser, producing less intense light and not posing the same hazards to the eyes and skin [54]. The illumination source consists of 72 eye-safe high-power LEDs, covering an effective area of 300x100 mm. Similar to the MiniShaker, the LED lamp is attached to a rod, guiding the cables above the waterline. Both the MiniShaker's and the LED's supporting rods are mounted to the towing carriages above the water line in the tank, as later illustrated in Figure 3.16. Thus, the distance between the carriages can be manually adjusted depending on the volume of interest (VOI). A significant advantage of this camera system is that it can be moved without the need for recalibration [52]. Table 3.5 further highlights some key technical specifications for the PIV system.

Table 3.5: *Technical specifications for the MiniShaker multi-camera and the LED Flashlight 300 from LaVision [52]. The tracer particles were the same type as for the ADV instrument, highlighted in Table 3.4.*

Component	**Technical specifications**	
MiniShaker multi-camera	Camera resolution	896x656 pixels
	image acquisition	8- or 10-bit
	Max frame rate	510 fps
	Recording rate	150 Hz
	Camera exposure time	200 µs
	Focal length of lenses	7.8 mm
LED Flashlight 300	Array area	300 x 100 mm
	LEDs	72 eye-safe high powered
	Working distance	500-2000 mm

Prior to the measurement campaign, the imaging system was calibrated by taking 2D images of a stationary 300x300 mm calibration plate. This perspective calibration was done in cooperation with LaVision during an introduction day of the newly acquired PIV system and was subsequently reused for the measurement campaign in this thesis. Nevertheless, the calibration procedure allows for the algorithms in DaVis 10 to triangulate the subsequent 2D images to accurately 3D-reconstruct the particles' position in the flow field. Volume-Self-Calibration (VSC) was then iteratively applied on a sample set of 100 images for each VOI. Thus, correcting for any remaining calibration error from the first calibration step, based on captured images of the tracer particles in the flow [55]. In this VSC procedure, a VOI with the dimensions of 350x250x140 mm was divided into 4x4x2 subvolumes. A maximum number of particles were set to 10 000 with an allowed triangulation error of 1.5 pixels, resulting in

voxel disparity below 0.01. Hence, well in line with the criteria for a valid calibration for this kind of experiment [52]. Based on an averaged particle image of the obtained VSC data, an Optical-Transfer-Function (OTF) is calculated. Thus, allowing the algorithms in the STB module to accurately track the particles' positions over time. This post-processing procedure, containing the STB module and data stitching, will be further reviewed in Section 3.6.3.

3.5 Measurement procedure

The following section will provide an overview of the experimental procedure with respect to the different measurement methods. These methods are based on either a load cell, ADV, or PIV, where the instruments are previously described in Section 3.2 - 3.4.

3.5.1 Load cell measurements

The load cell measurements were performed at six different towing velocities: 0.5 m/s, 0.6 m/s, 0.7 m/s, 0.8 m/s, 0.9 m/s, and 1.0 m/s, as previously highlighted in Table 2.3. Each experimental run was conducted once for each velocity. The force measured during this campaign is the drag force on the disc and tower. This is because the single disc configuration is a non-rotating fixed object. However, in the wind turbine theory, previously reviewed in Section 2.3.1, the wind moves through a rotating turbine, thereby creating a thrust force. In other words, the thrust and the drag forces are equally big with an opposite sign. Nevertheless, the parameter of interest is the thrust force, F_T, and the thrust force coefficient, C_T.

The experimental approach is based on the disc and tower being dragged through the towing tank at different velocities. These velocities depend on the Reynolds number, given in Equation 2.27. In order to identify the thrust coefficient that acts upon the disc, the drag force associated with the tower needs to be taken into account. This is done based on Equation 3.8.

$$C_T = \frac{F_x - F_{x,tower}}{0.5\rho_{water} A_{total} u_0^2}, \tag{3.8}$$

where F_x is the drag force from the tower and disc, while $F_{x,tower}$ is the drag force acting on the tower alone. The experimental values obtained from the measurements will be compared to the theoretical ones previously highlighted in Table 2.2. The goal of this thrust force campaign

is to compare these parameters based on the different disc solidities. Additionally, the data will be checked for Reynolds independence, accordingly with Figure 2.10. The measurements are only done for the SR for simple comparisons, as the primary purpose of this thesis is to investigate the flow characteristics in the upstream and downstream regions of the SR and MR7. The experimental runs were not repeated. Hence, giving a too-small sample size for uncertainty calculations. Nevertheless, uncertainty calculations for this type of experiment are previously well documented by Koi [20].

3.5.2 ADV-based wake measurements

The experimental campaign continued with the ADV-based measurements in the towing tank. Figure 3.13 illustrates how the experiment was set up.

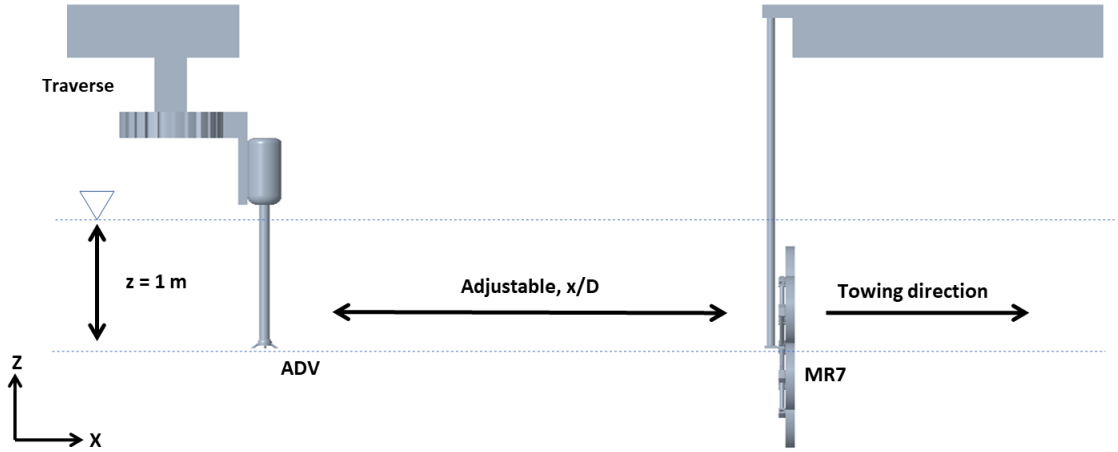

Figure 3.13: *Experimental setup of the ADV-based approach, illustrated in the XZ-plane.*

As Figure 3.13 illustrates, the ADV and the actuator disc configuration were mounted to two separate carriages, with the in-between horizontal distance adjusted depending on the area of interest. The experimental measurements performed on the SR were based on a downstream distance of $x = 2d$, $x = 4d$, $x = 7d$, and $x = 10d$, respectively. A depth of $z = 1$ m from the above water surface to the center of the setup was applied. This distance was considered deep enough to avoid potential effects from the surface waves. Furthermore, a maximum distance of $y = \pm 1.5d$ from the discs' center point was used, thereby defining the interval of the performed measurement points and the width of the wake. By remotely controlling the traverse's location using a LabVIEW program, the position of the SR or MR7 could easily be adjusted, as Figure 3.14 illustrates.

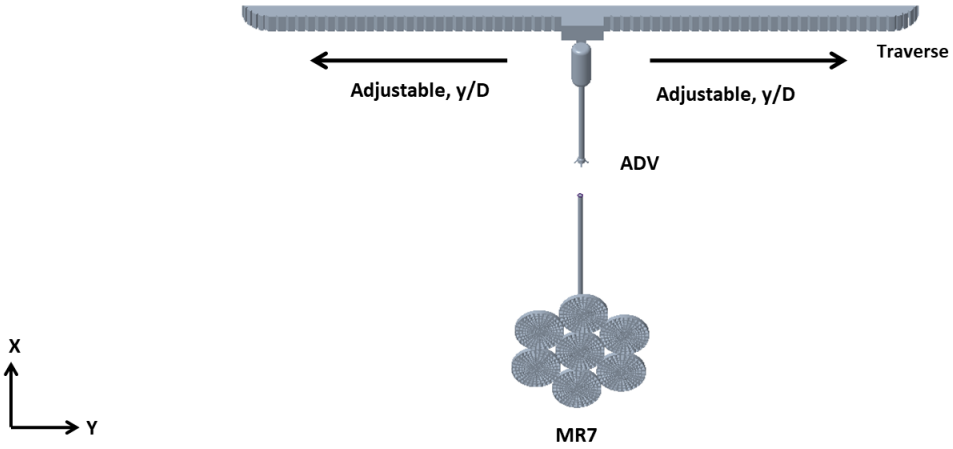

Figure 3.14: *Experimental setup of the ADV-based approach, illustrated in the XY-plane.*

As for the MR7, both upstream and downstream measurements were performed. A total overview of the key parameters related to the measurement campaign for SR and MR7, respectively, is given in Table 3.6 and Table 3.7.

Table 3.6: *Overview of the measurement procedure of SR.*

Key parameters	**Single rotor**			
x [-]	2d	4d	7d	10d
x [mm]	400	800	1400	2000
y [-]	3.5d	3.5d	3.5d	3.5d
y [mm]	700	700	700	700
Center disc solidity, σ	All	All	All	All
Measurement points y(+)	28	28	28	28
Control points (y-)	10	10	10	10

Table 3.7: *Overview of the measurement procedure of MR7.*

Key parameters	**MR7 (s/d = 0.1)**						
x [-]	± 0.4d	± 1d	± 1.4d	± 2d	± 3d	± 2D	± 7D
x [mm]	± 80	± 200	± 280	± 400	± 600	± 1280	± 4480
y [-]	± 3.5d	± 3.5d	± 3.5d	± 3.5d	± 3.5d	± 1.5D	± 1.5D
y [mm]	± 700	± 700	± 700	± 700	± 700	± 960	± 960
Center disc solidity, σ	All	All	S47, S67	S47, S67	S47, S67	All	S47, S67
Measurement points y(+)	45	45	45	45	45	48	32
Control points (y-)	14	14	14	14	14	15	10

It is essential to clarify that the downstream- (x) and horizontal (y) distances for the measurement points are based on either the isolated disc diameter d or the total diameter of the

MR7 setup, D. This diameter subsequently depends on the spacing between lateral discs, which is $s = 0.1d$. This adds up to having an isolated disc diameter of $d = 200$ mm and a total multirotor diameter of $D = 3 \cdot d + 2s = 640$ mm.

Due to a symmetrical setup, measurements were mainly done along the positive y-axis behind the disc setup. The measurements were then mirrored across the y-axis at $y = 0$ during the subsequent post-processing in MATLAB. However, some control points were established on the negative half to validate the symmetry. If the point did not correspond, it could indicate a yaw misalignment, and a manual adjustment of the measurement system could become necessary, which is further described in Section 3.6. Figure 3.15 illustrates where the experimental measurements were taken in the upstream and downstream wake.

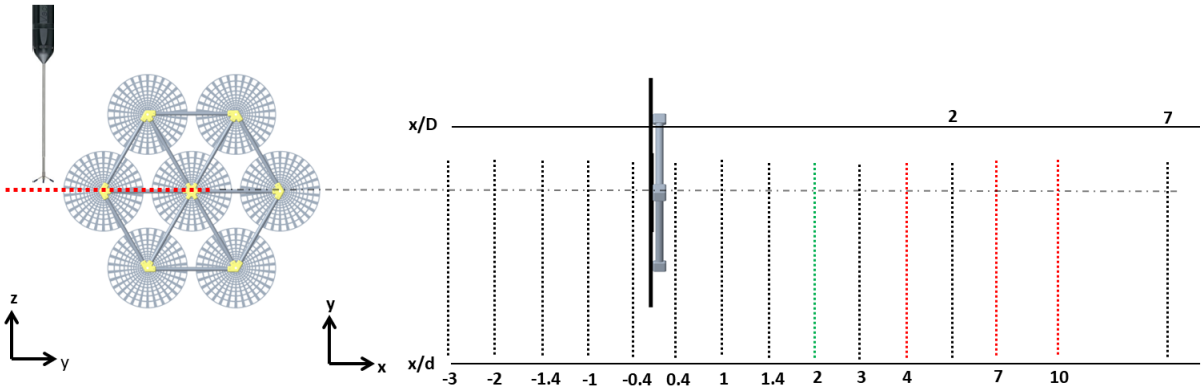

Figure 3.15: *Overview of the performed ADV measurements. The black and red dashed lines represent the MR7 and SR measurements, respectively. The green dashed line represents a distance where both MR7 and SR were measured.*

In the figure above, the left side displays the multirotor in the yz-plane, illustrating the stepwise movement of the ADV along the y-axis for each new measurement. This approach allows for obtaining a horizontal wake profile. On the right side of the figure, the xy-plane visualizes the various horizontal downstream distances.

When the measurement procedure was done for a day, the seeding particles tended to sink and gather in layers at the bottom of the tank. A surface layer of seeding particles was also visible at the water's surface. In order to obtain representative data, the ADV instrument depends on the reflected signal from the mixed particles in the water flow. Hence, a suffi-

cient mixing of the particles is required. Thus, the procedure started for each new day with experiments by generating waves in the tank. Simultaneously, the carriage was run back and forth with an extended structure reaching the bottom, breaking up the bottom layers of seeding particles. The physical experiments could start when the registered signal was stable in the Vectrino+ software without much noise, i.e., an SNR ≥ 10 for all three velocity components.

For each downstream distance from Figure 3.15, numerous measurement points were taken along the y-axis. This was done by adjusting the position of the ADV along the traverse using LabVIEW, as previously described in Section 3.1.1. Before each measurement, the water had to be as still as possible. Thus, a waiting time of 1 minute was required until the reading in the software showed $u = 0.00$ m/s. Additionally, each run took about 50 seconds, while the rewind process took another 30 seconds, adding up to a total of 2 minutes and 20 seconds for each measurement point. As per Table 3.7, a total of nearly 60 measurement- and control points was used for the MR7 experiments, meaning that the time needed for generating one single wake profile could take up to 2 hours and 20 minutes. Such an ADV-based approach is more time-consuming than the PIV approach, described in Section 3.4.

3.5.3 PIV-based measurements

The PIV instrument was utilized to investigate flow characteristics in the downstream region. The volume of interest (VOI) overlapped with the velocity profiles obtained by the ADV in the near wake, providing a solid foundation for comparison and analysis. Due to a large amount of data and time restrictions in the lab, only SR and MR7 with a disc solidity of 57% were investigated with the PIV. Figure 3.16 illustrates the experimental PIV setup.

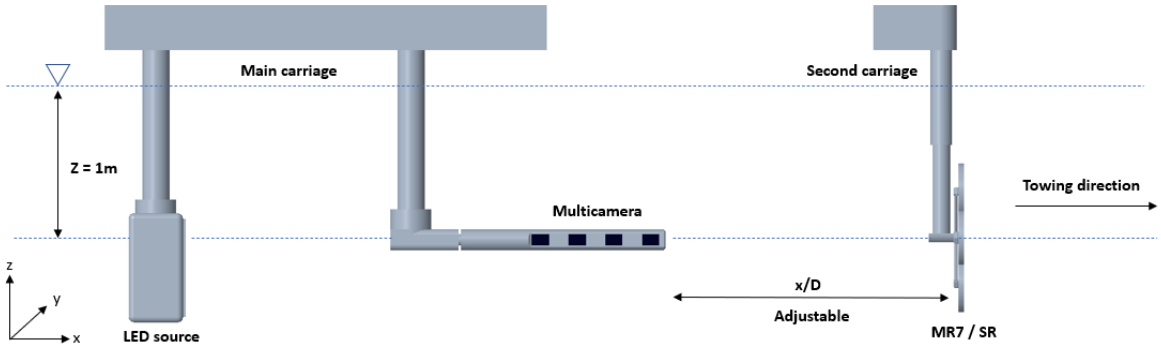

Figure 3.16: *The experimental setup of the PIV, including LED illumination source, Minishaker camera, and multirotor configuration.*

The multi-camera system, MiniShaker, and the LED source were mounted on the main carriage with the actuator disc configuration on the other. Similarly to the experimental procedure of the ADV, the horizontal distance was adjusted depending on the VOI.

Prior to the PIV experiments, the seeding particles in the towing tank were mixed to ensure an even particle distribution throughout the water volume. This was necessary for obtaining accurate and reliable results as PIV is a technique that relies on tracking the motion of particles in a fluid to determine flow velocity and other flow characteristics. The mixing procedure and seeding particles were the same as for the ADV experiments, previously reviewed in Section 3.5.2. These seeding particles' size was 5.5 times smaller than the polyamide particles recommended by LaVision [56]. However, Viola et al. [52] investigated the downstream wake of a turbine with the same particle size, obtaining clear images and reliable results. Thus, after consulting with LaVision, the already present seeding particles from the ADV experiments were also reused in this experiment.

Similarly to the ADV measurements, the towing velocity for the disc configuration and camera system was set to u_0 = 0.5 m/s. Each of the four cameras had an exposure time of 338 µs with a maximum image rate of 0.167 kHz. When measuring a VOI, a frequency of 150 Hz was used over a time interval of 16 s, adding up to a total of 2400 images. The image recording was manually started after approximately 15 s when the two carriages from Figure 3.16 had obtained a constant velocity. Hence, avoiding the acceleration- and deceleration phases of the carriages.

As illustrated in Figure 3.16, the multi-camera and LED illumination sources were located in the wake of the SR and MR7. The LED source was placed at a distance of $y = 1.1$ m from the camera system's focal volume, perpendicular to the camera field. Furthermore, the LED lamp was placed centrally at $y = 0$ behind the SR and MR configuration. Each illuminated VOI dimension was 350x250x140 mm, illustrated in Figure 3.17. Thus, a vertical wake profile was obtained by traversing the camera and LED source along the vertical axis. This approach differs from the ADV measurements, where a horizontal wake profile was measured. However, according to Øye [57], the vertical and horizontal wake profiles are very similar for an SR, with the curves coinciding. The only differences are at the upper half of the vertical velocity profile, where the support tower and surface effects influence the wake generation. Hence, only the lower part of the vertical velocity profile was measured before mirroring the data during the post-processing in MATLAB.

Figure 3.17 illustrates the illuminated volumes of interest in the downstream wake, including the location of the extracted wake profiles.

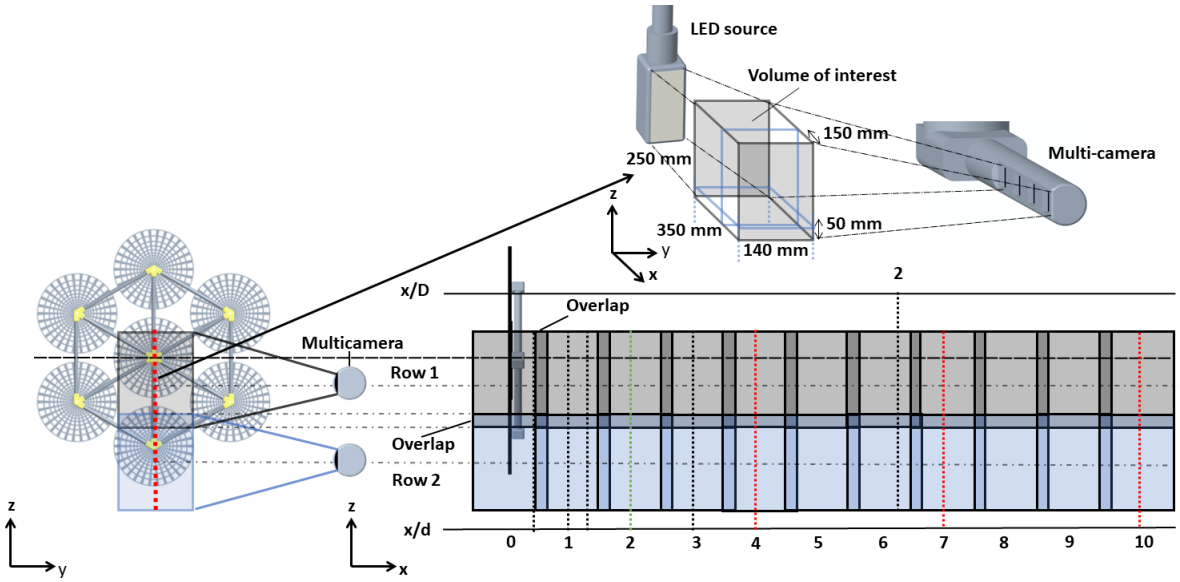

Figure 3.17: *PIV experimental procedure. Measurements at row 1 were performed for SR and MR7, while row 2 was only performed for MR7. The black, red, and green dashed line represents the location of the obtained wake profiles for MR7, SR, and both, respectively.*

As Figure 3.17 presents, the MR is rotated by 60 degrees, giving three vertically aligned actuator discs. This adjustment was necessary to ensure a valid comparison with the horizontal wake

profiles obtained from the ADV measurements. As previously illustrated in Figure 3.15, the three middle discs were horizontally aligned for the horizontal wake profile measurements. Now, they are vertically aligned for the vertical wake profile measurements. Furthermore, the camera and LED are traversed by a distance of x = 200 mm in the downstream direction, providing an overlap of 150 mm. This was done stepwise from $x = 0d$ to $x = 10d$, with these distances corresponding to the middle point of the multi-camera. In total, 11 VOIs were measured for SR and MR7, described as row 1 in Figure 3.17. However, a second row was implemented to capture the whole vertical wake for MR7. Hence, the camera system and LED were traversed by a distance of z = 200 mm in the vertical direction, described as row 2, giving an overlap of 50 mm. To distinguish each row and VOI, the first-row VOI is enumerated as 1.0 - 1.10, while the second row is enumerated as 2.0 - 2.10. The measurement data are later evaluated and stitched together in the post-processing, reviewed in Section 3.6.3. Vertical wake profiles are then extracted from full-flow field pictures. The black, red, and green dashed line in Figure 3.17 represents the location of the obtained wake profiles for MR7, SR, and both, respectively. Furthermore, Table 3.8 provides an overview of the measurement procedure of SR and MR7.

Table 3.8: *The measurement procedure for the PIV-based SR and MR7 experiment.*

SR and MR7			
z_1 = -0.8m	**x/d**	**x/D**	**[mm]**
S57	0	0	0
	1	0.3125	200
	2	0.625	400
	3	0.9375	600
	4	1.25	800
	5	1.5625	1000
	6	1.875	1200
	7	2.1875	1400
	8	2.5	1600
	9	2.8125	1800
	10	3.125	2000

For SR, the measurement procedure presented in Table 3.8 was conducted once. However, for MR7, the procedure was carried out twice at two different heights. This was done due to being able to capture the complete velocity profile. Hence, the MR configuration was lowered to z_2 = -1.0 m.

3.6 Post-processing

After acquiring all the necessary data, further post-processing was required. This process was done in MATLAB for the load cell and ADV measurements, while the software DaVis 10 provided by LaVision was used for the PIV. Section 3.6.1 - 3.6.3 describe the post-process in detail.

3.6.1 Load cell

The post-processing of the load cell data was performed using MATLAB. The procedure, which included a cropping and averaging phase, is illustrated in Figure 3.18.

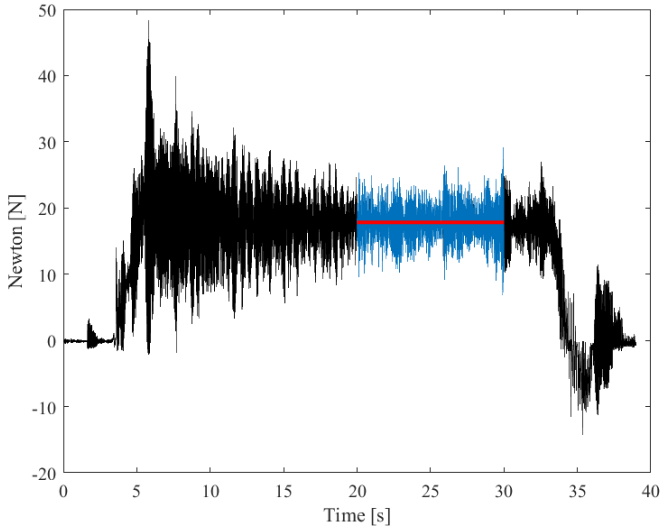

Figure 3.18: *A time series of SR with 57% solidity with a towing velocity of u_0 = 0.5 m/s.*

The figure shows a time series of the SR data with a 57% solidity with a towing velocity of $u_0 = 0.5$ m/s. Each measurement run produced a time series with over 10 000 measurements, represented as the black signal in the figure. As the figure illustrates, the signal is influenced by the acceleration and deceleration phases of the carriage. However, the signal of interest is when the carriage has reached a constant towing velocity. Therefore, the acceleration and deceleration phases were removed from the calculations.

To obtain the average value, a time interval from $t = 20$ s to $t = 30$ s was selected, which varied depending on the quality of the time-series signal and the towing velocity. Additionally, if the start and end phases did not end at zero, an adjustment was made by calculating the average

value of the start and end phase and either subtracting or adding it to the averaged value. The time interval for the average value was determined based on the appearance of the signal. If the signal was unstable, had much noise, or was in the acceleration or deceleration phase, it would give an inaccurate thrust force. This method ensured that the thrust force calculated was the most accurate representation of the force acting on the actuator disc. Equation 3.9 was used to calculate the mean thrust force.

$$\bar{F_T} = \frac{1}{N} \sum_{i=1}^{N} F_i \tag{3.9}$$

Here N is the number of samples in the cropped time series, and F_i is the thrust force at a given time in this interval. This thrust force calculation was done separately for the tower alone and the tower with the actuator disc. The thrust force for the tower was then subtracted, giving the thrust force for the actuator disc. The thrust coefficient, C_T, was then calculated based on Equation 3.8.

3.6.2 ADV

After all the experimental ADV measurements were performed in MarinLab, the acquired data were converted to data files. These files were then transferred to a MATLAB script, where all the time series filtering and calculations in terms of the average velocity reduction and turbulent kinetic energy were done. Each of the completed measurements had an associated time series. The carriage's acceleration and deceleration phase influences these time series' start and end phases. Additionally, an overshoot signal is visible when the carriage has reached a constant velocity. Hence, cropping of the time series data is necessary to eliminate these effects on the subsequent calculations.

Furthermore, the signal includes a number of very high or low outlier values which deviate from the average value. This is due to the ADV instrument missing a reflected signal from the seeding particles caused by inadequate mixing in the tank. In order to cancel out these outliers, the signal is further cleaned using a Hampel filter in MATLAB. The Hampel filter is controlled by two parameters, K and σ, respectively. The K value is the length of samples taken into account for filtering and is set to $K = 200$. Moreover, the-σ value is the multiple of

the standard deviation and is a threshold for declaring a sample as an outlier. A value of $\sigma = 4$ is consequently applied. Figure 3.19 illustrates an example of this filtering process. This time series is based on the single rotor with a disc solidity of 57% at the vertical and horizontal distances, $y = 50$ mm and $x = 2d$.

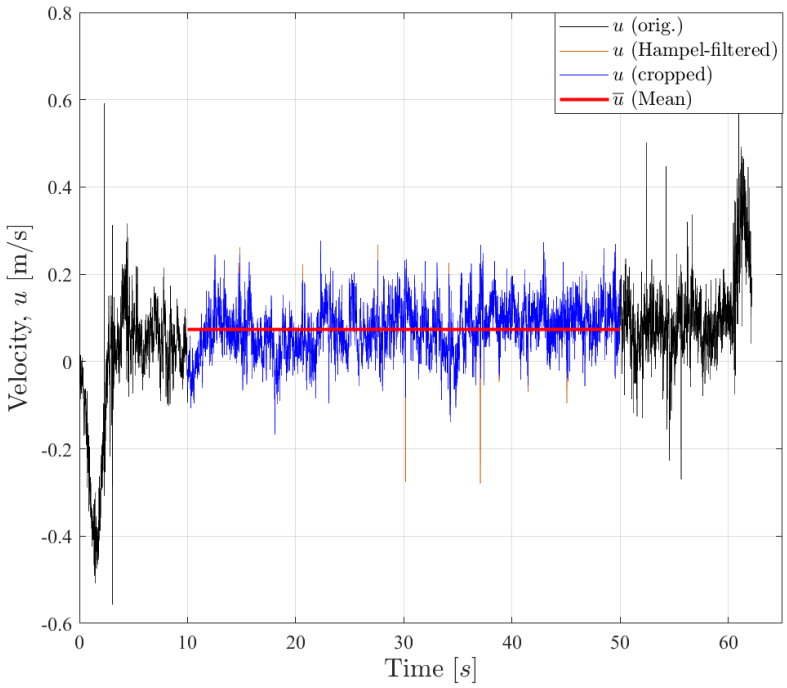

Figure 3.19: *Hampel filtered times series of SR with 57% solidity at $y = 50$ mm and $x = 2d$.*

After acquiring all the time series based on the different positions along the y-axis, the average velocities were saved and extracted from the file. This mean velocity calculation is based on Equation 3.10.

$$\bar{u} = \frac{1}{N} \sum_{i=1}^{N} u_i \tag{3.10}$$

Here N is the number of samples in the cropped time series and u_i is the measured velocity at a given time in the interval.

Then, a wake profile containing all the individual mean, normalized velocity reductions, $\bar{u}/u_0$, was established. The curve was then moved along the same axis to find a valid center point. This point is defined as the one with the most significant velocity reduction. This is necessary because the disc setup and the ADV were not always perfectly aligned. The curve was then

mirrored across the symmetry line at $y = 0$ and validated through the taken control point measurements. Figure 3.20 shows how the mirroring process was carried out for different disc configurations.

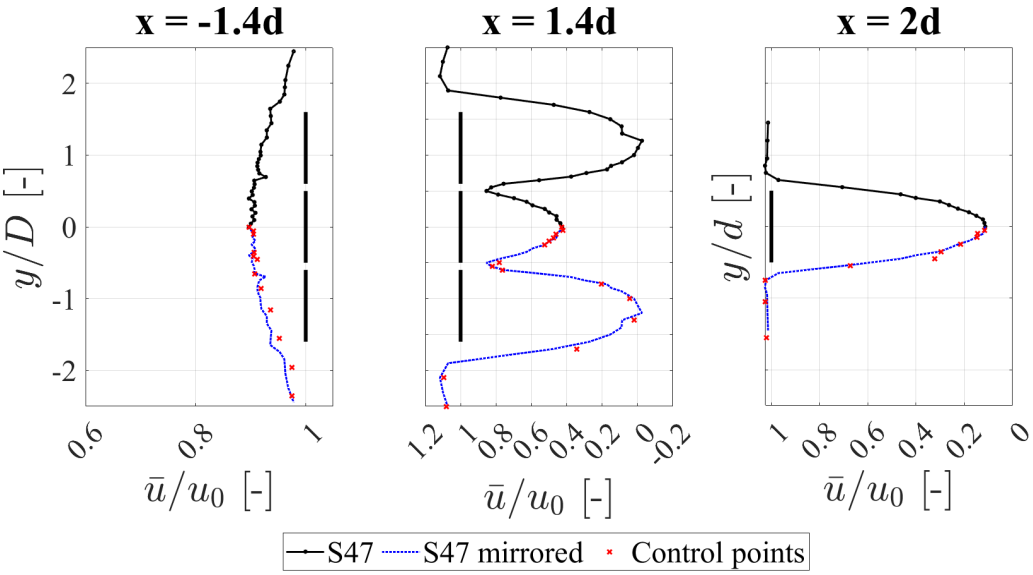

Figure 3.20: *Mirrored wake profiles for MR7 and SR with the S57 center disc. The two MR7 profiles measured at x = -1.4d, x = 1.4d, while SR profile measured at x = 2d. Control points are included for symmetry validation.*

As Figure 3.20 illustrates, the y-axis is represented as y/d for SR, with d being the diameter of a single disc. A similar approach is used for MR7 in the upstream induction zone and the very near wake. However, in the near wake and far wake, respectively, the y-axis is represented by y/D, with D being the diameter of the whole multirotor configuration, with the inter-rotor spacing taken into account. The x-axis is represented as a normalized velocity reduction, $\bar{u}/u_0$, where $\bar{u}$ is the average velocity at each given measurement point. The normalized maximum velocity reduction, $\bar{u}_{max}/u_0$, is later tabulated as an additional comparison between the upstream and downstream wakes. The turbulent kinetic energy and cross-stream will also be normalized during the presentation of results, giving tke/u_0^2 and $\bar{v}/u_0$. These parameters will give a comprehensive insight into the wake development and be a basis for comparison and analysis between the wakes.

3.6.3 PIV

This section describes the post-processing procedure for a single time series of 1200 samples at a horizontal distance of $x = 1d$. In other words, the second upper left VOI box, number 1.1, from Figure 3.17. However, it should be noted that the parameters in the different processing steps could vary for each VOI, depending on conditions such as seeding density and illumination. For MR7, the upper row was later merged together with the lower row to obtain the vertical velocity profile for the lower part of the rotor. Then, MATLAB was used to average and mirror the obtained data, similarly to the previously described ADV technique in Section 3.6.2.

The basis for preprocessing the image sequences in this thesis was a combination of different spatial filters. First, the image was preprocessed using a subtracted sliding minimum filter of 5 pixels. This filter subtracts the minimum value in a sliding window of 5 pixels from the pixel value, effectively removing noise and small-scale variations from the image. The image was then normalized with a local average and smoothed over 300 pixels, which helps to improve SNR and reduce the effect of small-scale variations in particle image intensity. The previous steps were performed for each image in the time series, with all frames normalized to the first frame. A sliding Gaussian smoothing filter was applied, and sharpening was enabled to enhance the image's contrast. Additionally, a subtract constant of 5 counts was applied to each pixel, and the pixel values were multiplied by a factor of 10 to increase the sensitivity of the measurements.

This procedure was performed twice, giving two separate data sets. The first set had an increment of 24, resulting in 100 images. This set was subsequently used for the VSC, previously described in Section 3.4. The second set contained the first 1200 samples and was used for the STB analysis. The selected number of samples was based on a convergence analysis of the velocity profile curves, which indicated that the curves converged with increasing numbers of samples, highlighted in Figure 3.21.

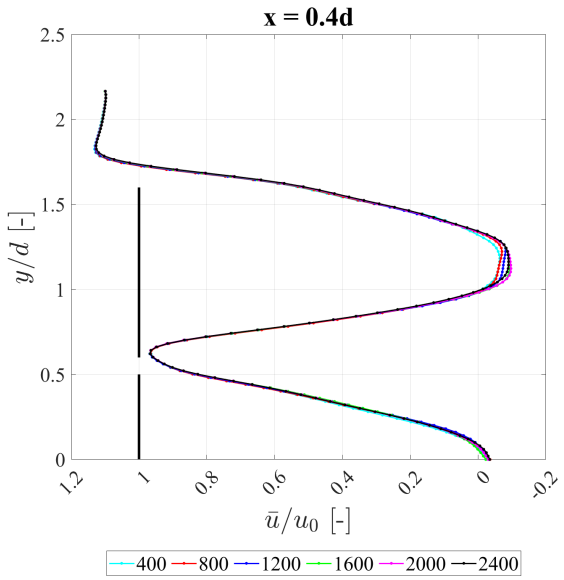

Figure 3.21: *Convergence of the curve at x = 0.4d, from 400-2400 samples.*

A visualization of the velocity profile convergence is provided in the figure. It is observable that the individual curves show little variation only in the wake centers, and therefore using the entire dataset of 2400 samples would not significantly improve the accuracy of the velocity measurements. By limiting the analysis to the subset of 1200 samples, sufficiently accurate velocity measurements were achieved while minimizing the computational resources.

The STB process was then applied to the image sequence of 1200 samples. The underlying concept behind this analysis is well documented by Viola et al. [52] and involves several steps to predict the 3D particles' positions accurately. These steps involve an iterative particle reconstruction by "shaking" the particles to determine the 3D particle positions from the camera images. The OTF obtained from the calibration procedure previously described in Section 3.4 is used for determining 3D positions by considering the optical properties. The STB module's initialization process involves triangulation, polynomial fitting, and "shaking" to optimize the match with the projected 2D particle [52].

The described post-process was carried out for each VOI before being merged together. In other words, they combined the datasets into a composite of multiple spatial volumes. This process involved several steps to ensure that the data was accurately aligned and merged. Here on, the merging process for obtaining the vertical velocity profiles at $x = 0.4d$, $1d$, and

1.4d will be reviewed. The obtained STB flow fields for VOI boxes 1.1 and 2.1, from Figure 3.17, were then merged using the "Merge Particle Track" operation. Before this merging, the upper flow field was shifted vertically by a distance of z = 200 m, ensuring a proper alignment. A spatial median filter was applied to the combined data to improve the quality of the flow field further. The median spatial filter helps to remove any remaining outliers or errors in the data by replacing each data point with the median value of its surrounding data points [58]. This merged flow field between x = 0 mm - x = 350 mm, i.e $x = 0d$ - $x = 1.75d$, is further illustrated in Figure 3.22.

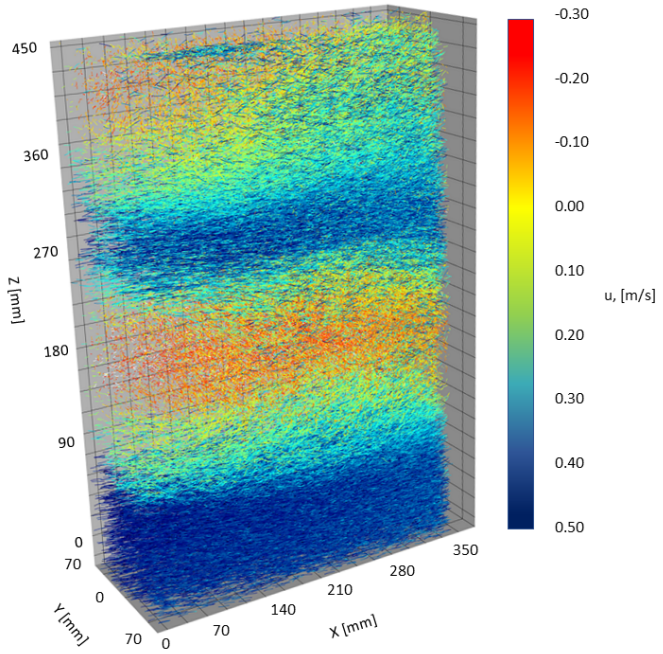

Figure 3.22: *Merged STB flow field for MR7: VOI box 1.1 and 2.1 from Figure 3.17. The illustration shows the particles tracked over a length of 120 images, corresponding to 10% of the sample set.*

Furthermore, the combined flow field was binned to map the flow properties within the VOI. This module interpolates local tracks, converting particle tracks to vector field data with a specified grid [58]. Thus, simplifying the data, making the results easier to visualize and interpret. The flow field was divided into bins of 96x96x96 voxel size, including an overlap of 87.5% between adjacent bins. One binning map was created for each of the 1200 samples. These generated bins were then averaged to a velocity field, which was the basis for the wake profile extraction. An illustration of the binning map at the midplane, y = 0, is further provided in Figure 3.23. An instantaneous velocity field from one of the bins is illustrated to the left, and an averaged velocity field based on all 1200 samples is presented to the right.

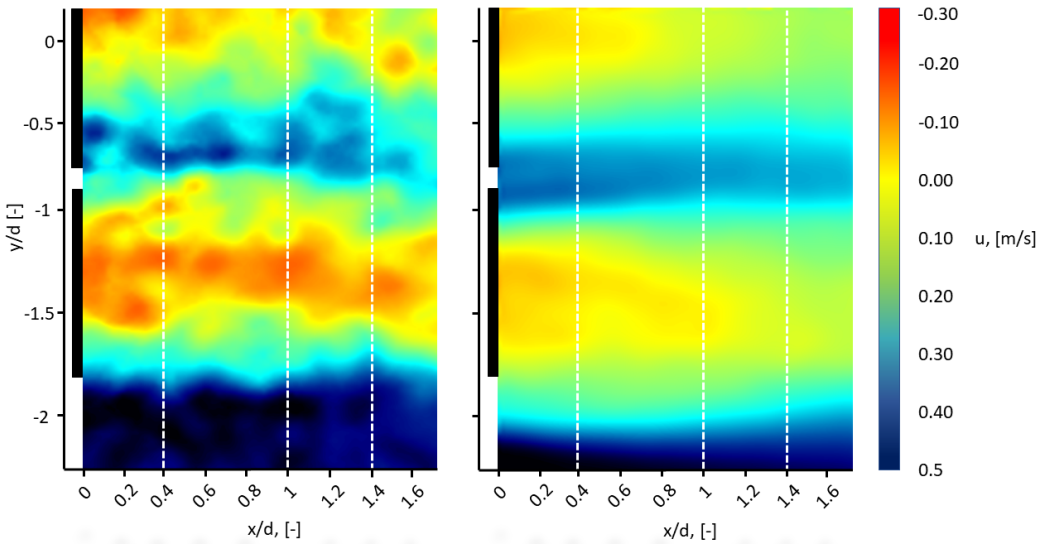

Figure 3.23: *Instantaneous velocity field to the left and averaged velocity field to the right. These binned datasets are based on the STB process from Figure 3.22. The chosen bin is taken from the midplane at y = 0. The white dashed line represents the horizontal locations where the wake profiles were extracted.*

Vertical wake profiles at different downstream distances were then extracted from this merged velocity field, providing insights into the development of the wake. The total overview of the locations at which the velocity profiles were extracted is previously given as red, black, and green dashed lines in Figure 3.17. However, Figure 3.23 illustrates the extracted velocity profiles for MR7 from $x = 0.4d$, $x = 1d$, and $x = 1.4d$. For SR, the complete vertical wake profile was captured by the Minishaker cameras. However, for MR7, only the lower half of the wake was captured. This was due to the restricted camera field and the size of the MR7, previously highlighted in Section 3.5.3. The plot operation tool from the DaVis 10 software was applied to the merged, averaged velocity fields. The subsequent results were then mirrored in MATLAB to present the different velocity ant tke profiles, later presented in Section 4.4 and Section 4.5.

3.7 Measurement uncertainty and errors

During an experimental campaign, different sources of errors and uncertainty are present. These sources can be divided into two separate categories, systematic errors and random errors, respectively. Systematic errors influence the measurements' accuracy and are mainly due to environmental, observational, and instrumental errors. Random errors influence the precision of the measurements and are linked to factors that are difficult to control and vary with each measurement [29]. In the following sections, these measurement errors will be reviewed for each measurement method.

3.7.1 Load cell

The manual mounting of the experimental equipment represents the first potential systematic error that could affect all measurement methods. Specifically, using an aluminum ruler to position the measurement instrument and the multirotor at a predetermined depth of $z = 0.8$ m can introduce uncertainty in the vertical position due to potential inaccuracies in the positioning of the apparatus. Furthermore, this manual approach can result in unintended yaw or tilt angles, deflecting the wake horizontally or vertically. If the supporting structure is not sufficiently rigid to withstand the resultant thrust forces generated during water tank towing, an additional tilt angle of the multirotor may arise, leading to a decomposition of the corresponding thrust force. Despite this decomposition, its impact on the measurement outcomes is negligible. For example, assuming a yaw angle of 5°, the resulting decomposed axial thrust force is given by Equation 3.11.

$$F_{T,dec} = cos(5°)F_T = 0.996F_T. \tag{3.11}$$

Therefore, the thrust force is only reduced by 0.4%, which has an insignificant effect on the results. The same applies to the yaw angle.

Other potential sources of systematic error include misalignment of the load cell, particularly if it is not properly mounted to the experimental setup or aligned with the thrust direction. Calibration errors may also occur if the load cell is not accurately calibrated. In this study, a two-point calibration was conducted to minimize such errors.

Random errors in load cell measurements are often associated with environmental conditions that affect the experimental setup. For instance, when towing the apparatus through the water tank, the carriages may experience vibrations caused by the wiring system, potentially affecting the resulting data. Furthermore, random noise may arise due to various factors, such as electronic interference or sensor drift, which can introduce measurement uncertainties. Such random errors may impair the precision of the load cell readings.

A mean value was computed over each time series to reduce the impact of random errors in the load cell measurements, as described in Section 3.6.1. The load cell was also subject to regular calibration and quality control checks, such as linearity and hysteresis tests, to ensure the accuracy and precision of the readings. Despite these measures, the presence of random errors in the load cell measurements cannot be entirely eliminated and may affect the reliability and validity of the results.

3.7.2 ADV

The ADV-based measurements could potentially be subject to systematic errors primarily due to the manual positioning of the instrument in the towing tank and errors associated with the ADV itself. The mounting and setup process involved manually measuring the horizontal distance downstream in the x-direction and the depth of the multirotor and ADV in the z-direction. The use of an aluminum ruler introduced human-related uncertainties. Furthermore, a proper alignment of the instrument parallel to the z-axis was crucial for obtaining representative velocity measurements for the x-, y-, and z-directions. This required a stiff support structure for the ADV to withstand the drag forces during towing and prevent system bending. Notably, these sources of systematic error are common to those previously described for the load cell measurements. These manual measurements and assessments were only performed once prior to the measurement campaign. Hence, observational errors may have occurred due to inaccurate readings and reviews during this process.

Another known systematic error with the ADV measurements is linked to the measurement instrument, with the broken in-built temperature sensor. The ADV registered a temperature of

-7°, while a thermostat measured a value of 16°. Hence, this systematic error must be considered during the post-processing of the data. As previously given in Equation 3.6, the ADV uses the speed of sound in water to compute the subsequent three-dimensional velocity vector. However, the speed of sound is dependent on the water temperature. Hence, implementing a correction factor becomes necessary. This correction factor is based on an experimental study performed by Bjørnsen [59], who discovered a difference between the towing velocity of the carriage and the subsequently registered velocity by the ADV.

A further potential systematic error of the ADV measurements is related to the particle mixing of the tank. The ADV instrument and its signal depend on a sufficient mixing of seeding particles. Thus, prior to the measurement campaign, a manual seeding of the tank was carried out. The particles were mixed by generating several waves with different amplitudes and frequencies simultaneously as the carriage was towed back and forth. This mixing step was required daily because the particles tended to aggregate at the water's surface and the bottom of the tank, despite being described as neutrally buoyant. The mixing was considered well enough when the signal was relatively stable, with an SNR ratio above ten registered in Nortek's software.

However, some aspects of particle mixing can also be considered random errors. The seeding particles continuously moved during the experiments, meaning the environmental conditions changed for each experimental run. Additionally, the seeding density could be higher in some tank regions, affecting the signal-to-noise ratio. As for the load cell measurements, a further random error is linked to the vibrations of the carriages and random noise caused by electronic interference.

The experiments were conducted only once for each measurement point. For quantifying the measurement uncertainty with respect to sample length, it is referred to Skoland [19], who calculated the standard deviation based on various time series lengths at x = 2D to investigate how various numbers of data samples influenced the accuracy of the results. More specifically, the lengths of the measurement series being analyzed were 10300, 8300, 6300, 4300, and 2300 samples, calculated as standard deviation percentages relative to the longest series of 10300 samples. Results showed that the two shortest time series deviated significantly, closer to 5%,

while the two longest time series deviated under 1.5%. Hence, in this thesis, the length of the chosen samples was between 6000-10000 samples, depending on the acquired signal. An example of such a time series is previously given in 3.19. It is important to specify that the standard deviation depends on the downstream distance, with the velocity being more stable in the far wake than in the near wake. Thus leading to lower deviation.

3.7.3 PIV

The first source of systematic error relates to the mixing procedure and the seeding particle size. Mixing the seeding particles thoroughly before the PIV experiment can help ensure that the particles have the same size and density, which is essential for accurate velocity measurements. Variations in the size or density of the seeding particles can cause errors in the velocity measurements and lead to inaccurate results. If the seeding particles are not evenly distributed, the resulting PIV images will be distorted and inaccurate. As previously highlighted, the used seeding particles were approximately five times smaller than recommended. Moreover, the seeding density was considered to be too high. Although research [52] has shown that experiments can be conducted under such conditions, the size and number of seeding particles can influence the results. When the seeding particles are too small, they may not have sufficient mass or momentum to represent the flow accurately. This can lead to a lower signal-to-noise ratio in the images, making it more challenging to determine the velocity field accurately.

When too many seeding particles are present in the tank, they can create excessive background noise in the images. This can make it more difficult to accurately determine the velocity field and make it more difficult to distinguish between particles and other background features. In addition, if the seeding density is too high, the particles may begin to interact with each other and form clusters, leading to errors in the measurement of the flow field. Moreover, the particles begin to overlap, making distinguishing and detecting the individual particles difficult.

Another possible source of error is reflectivity and external light disturbances, affecting the clarity of the obtained images. However, several measures were taken to minimize these

impacts. Firstly, the actuator discs from Figure 3.2 were 3D printed in black to reduce their reflectivity. Secondly, the tower, screws, 3D connectors, and aluminum rods were also coated in black to reduce their reflectivity further. The same was done for the tank's walls to ensure that external light sources did not interfere with the measurements. These measures helped improve the measurements' accuracy and reliability by reducing the impact of unwanted light reflections.

The human errors that can have occurred are related to the configuration and setup of the measurement system. Firstly, improper camera and LED source alignment could have affected the velocity measurements. Additionally, the multirotor setup could have a slight yaw angle and not be stiff enough to withstand the resulting drag forces, as previously explained in Section 3.7.2.

When performing the actual measurements in the PIV campaign, an uncertainty value, U_x, is calculated for each associated velocity, u. According to the DaVis 10 product manual [58], the uncertainty of each individual sample is calculated based on a default setting of 1x standard deviation, σ, which represents the uncertainty of the data within a 68% confidence interval. To further average the uncertainty based on N_v number of vectors taken into account at each grid node, Equation 3.12 is used [52].

$$U_{u_i} = \pm \frac{\sigma_{u_i}}{\sqrt{N_v}} \tag{3.12}$$

Here, the uncertainty, U, is calculated for each i-th velocity component, denoted by u_i, with σ_{u_i} representing the standard deviation for each of these components. In other words, this is the equation for calculating the instantaneous uncertainty distribution based on one bin. To further calculate the uncertainty of the average velocity from the total of 1200 bins, DaVis 10 uses Equation 3.13 [58]:

$$U_{\bar{u}} = \pm \frac{\sqrt{\sum U_u^2 / N_s}}{\sqrt{N_s}} \tag{3.13}$$

where $U_{\bar{u}}$ is the uncertainty of the average velocity, U_u is the uncertainty of each individual velocity sample, and N_s is the total number of samples. The averaged velocity calculations

are based on Equation 3.10.

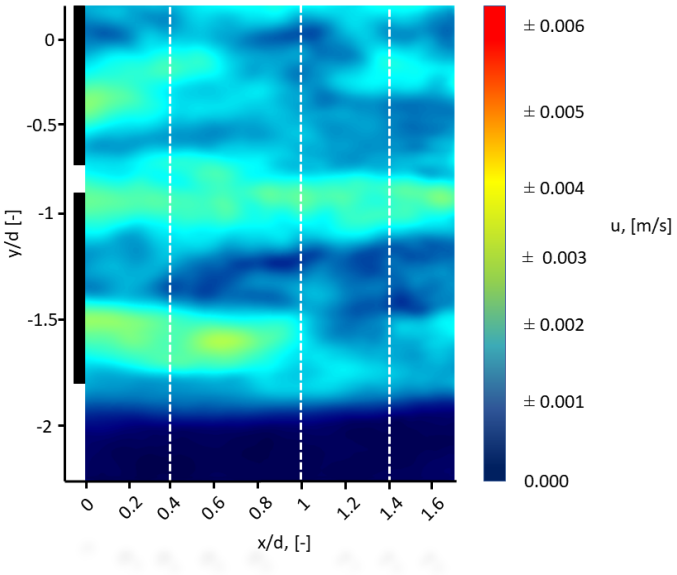

Figure 3.24: *The averaged uncertainty distribution, based on the averaged velocity field from Figure 3.23. The map illustrates the uncertainty of the horizontal velocity component, based on Equation 3.13.*

In the region corresponding to the free stream, the observed uncertainty is reduced compared to the adjacent shear layer. The highest uncertainty occurs in the in-between jet stream and along the edge of the outer disc. This is due to these regions being influenced by higher velocity gradients. An average uncertainty value for the complete velocity field was found to be $U_u = \pm$ 0.002 m/s, corresponding to 0.4% of the free stream velocity of $u_0 = 0.5$ m/s. Furthermore, a maximum uncertainty value was $U_u = \pm$ 0.0045 m/s, corresponding to a value of 0.9% of the free stream value. Generally, the uncertainty is low throughout the experimental campaign. For the remainder of this thesis, the velocity data will be presented without the accompanying error bars, simplifying the analysis of the actual measurements.

This page is intentionally left blank.

Chapter 4

Results and Discussion

The following section will present the results from the experimental campaign performed by the load cell, ADV, and PIV. Furthermore, the ADV- and PIV-based results will be compared and put in perspective to previous experimental work by Skoland [19] and Koi [20].

4.1 Thrust force measurements

Figure 4.2 presents the measured force at each towing velocity for each of the different discs' solidities.

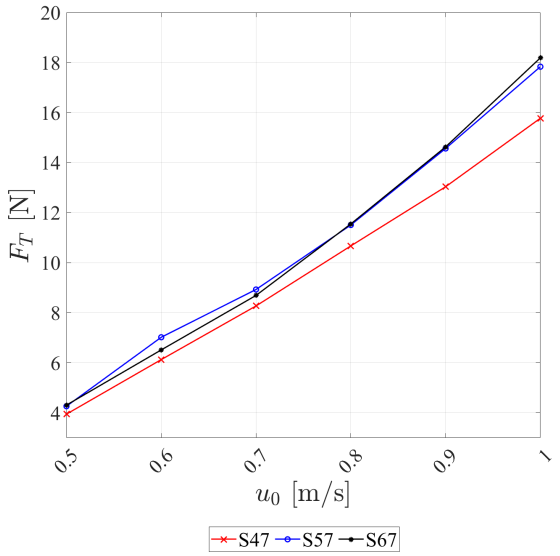

Figure 4.1: *The thrust force, F_T, as a function of the towing velocity, u_0.*

As expected, the thrust force increases as the towing velocity and solidity increase. The curves

show that S47 experiences the lowest thrust force, while S57 and S67 are higher. However, at towing velocities of u_0 = 0.6 m/s and u_0 = 0.7 m/s, S57 exhibited a higher thrust force compared to S67. This discrepancy could be due to various systematic or random errors, as discussed in Section 3.7.1. Furthermore, Figure 4.2 compares the thrust coefficient for each disc solidity as a function of the associated Reynolds number.

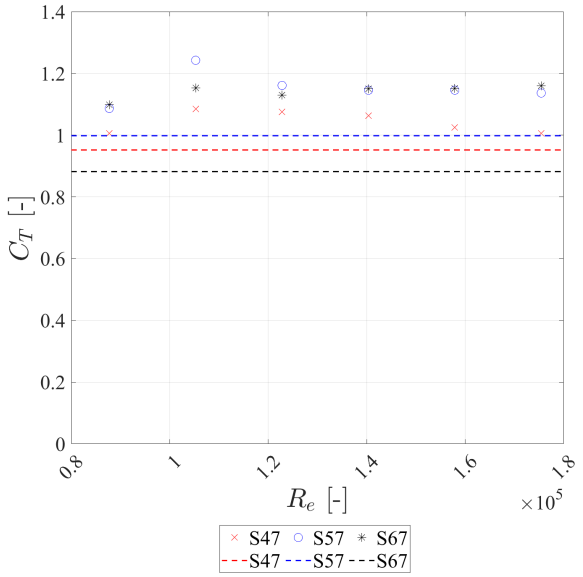

Figure 4.2: *The thrust coefficient, C_T, as a function of Reynolds number, R_e. The markers represent the experimental load cell measurements, while the dashed lines represent the theoretical values from Table 2.2.*

The figure clearly demonstrates that as the Reynolds number increases, the measured thrust coefficient for S47 approaches a value of 1. Similarly, the experimental values for 57 and S67 are slightly higher but also in close proximity. Consequently, achieving an exact match between the Reynolds number of a full-scale wind turbine and the experimental setup is not critical. The thrust force appears to be independent of the Reynolds number, aligning with the findings presented in Figure 2.10 of Section 2.8. This observation is consistent with the phenomenon described in the literature [45], where the drag force becomes independent of the Reynolds number once it exceeds a threshold of 1000. Moreover, the theoretical C_T values, as derived from Table 2.2, consistently appear lower than the experimental measurements. This discrepancy suggests that increasing the disc solidity leads to a decrease in the calculated thrust coefficient. However, it is important to note that this trend contradicts the physical reality, where increasing the solidity of the disc would logically increase the thrust coefficient.

4.2 ADV measurements of SR

The experimental campaign started by measuring the velocity reduction and the turbulent kinetic energy for a single disc in the downstream wake. An ADV instrument was used at a distance of $2d$, $4d$, $7d$, and $10d$ in the near and far wake, respectively. The measurements were based on three different discs with different solidities of 47%, 57%, and 67%, as previously reviewed in Section 3.5.2. The basis for the collected data was done per Table 3.6. The following sections will present the results for the ADV downstream measurements performed on SR. Initially, the individual flow fields will be reviewed, followed by the associated velocity, turbulence, and cross-stream profiles.

4.2.1 Full-field mean velocity

The downstream measurements of the different single rotors with respect to the different disc solidities are illustrated in three separate flow fields, summarized in Figure 4.3-4.5. It is essential to specify that the horizontal distances at which the measurements were taken are marked with a white dashed line. In between these horizontal distances, the obtained values are based on an interpolation approach, the *makima* function, in MATLAB during the data processing phase.

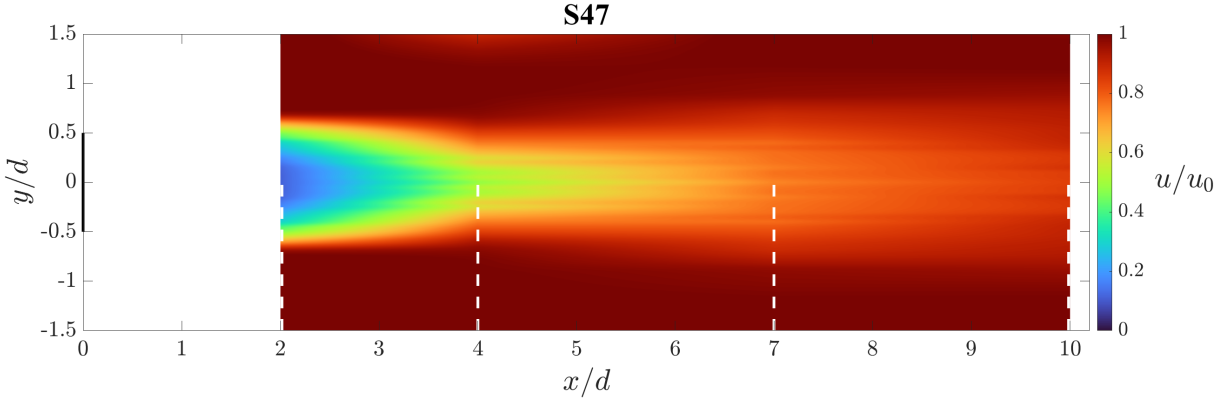

Figure 4.3: *Normalized mean velocity, u/u_0, in the wake of SR47.*

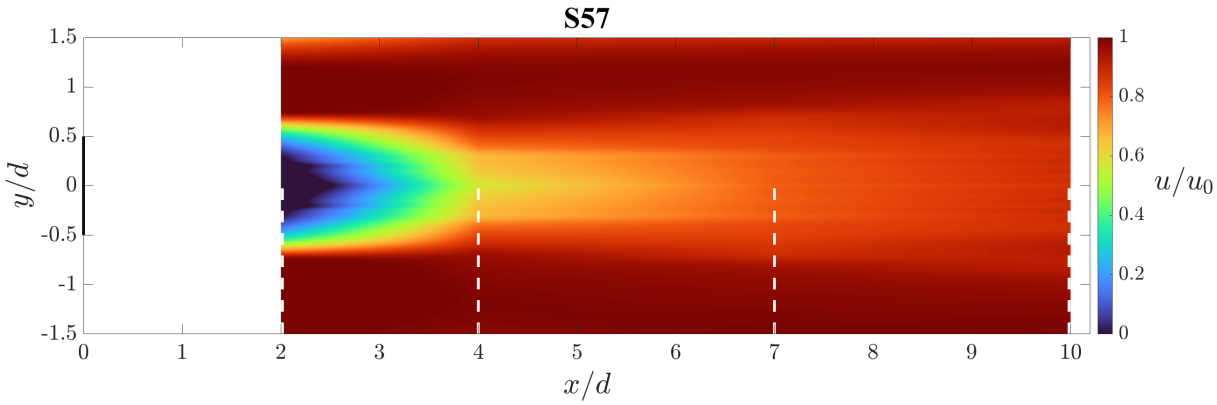

Figure 4.4: *Normalized mean velocity, u/u_0, in the wake of SR57.*

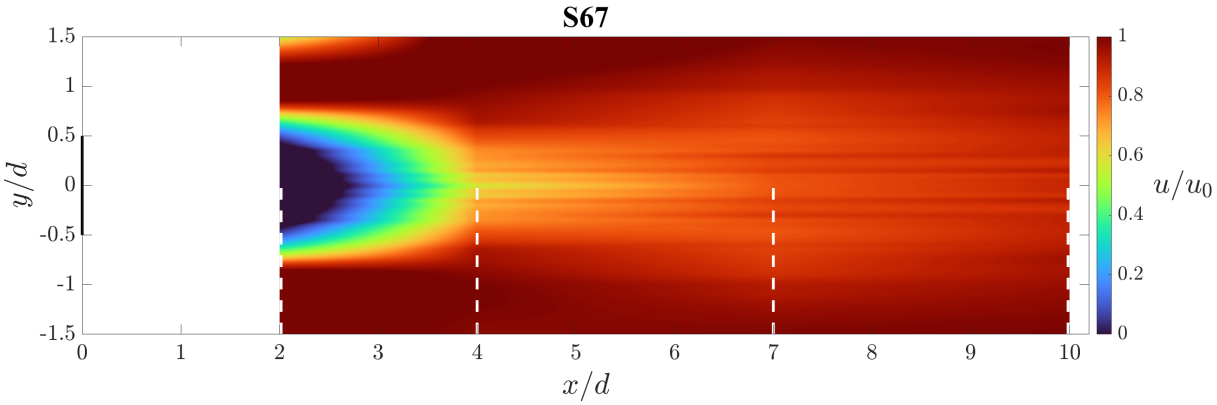

Figure 4.5: *Normalized mean velocity, u/u_0, in the wake of SR67.*

By comparing the results, it is clear that the downstream velocity reduction increases with increasing disc solidity. S47 has the lowest velocity reduction, while S67 has the biggest. Furthermore, the width of the wake gets noticeably wider as the solidity increases. As specified, the measurements were performed at $2d$, $4d$, $7d$, and $10d$, marked with a white dashed line in the above figures. Next, it will be interesting to compare the velocity, turbulence, and cross-stream profiles at each marked distance.

4.2.2 Downstream mean velocity reduction

In order to obtain a more detailed understanding of how the velocity reduction develops as the flow moves from the near wake to the far wake region, it is of interest to acquire and present the different velocity profiles. Hence, Figure 4.6 illustrates how the velocity reduction acts for each disc solidity.

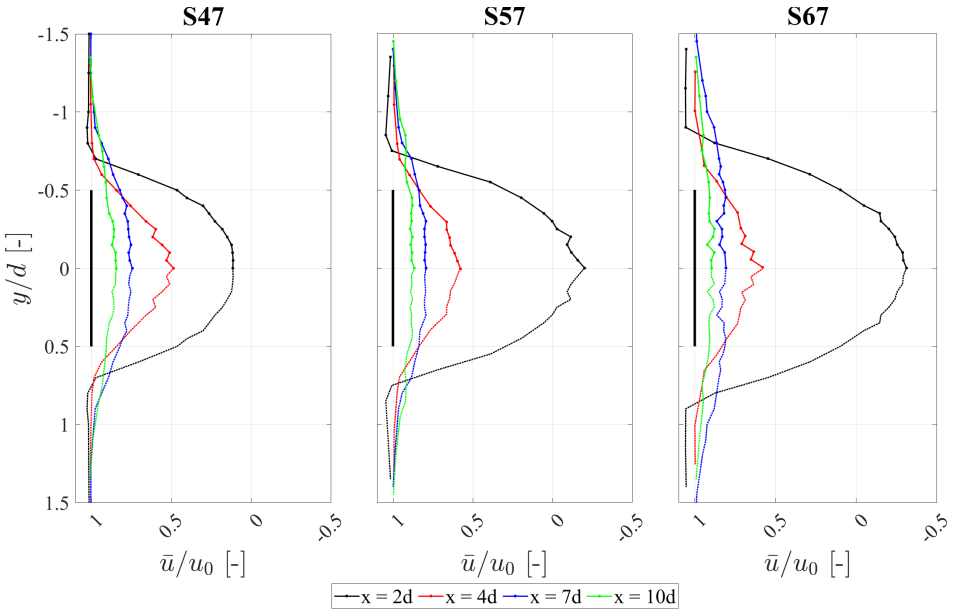

Figure 4.6: *Velocity reduction for S47, S57 and S67 at the downstream distances of* $x = 2d$, $x = 4d$, $x = 7d$ *and* $x = 10d$.

As expected, the velocity reduction increases with the horizontal distance. The most significant change in velocity occurs between $x = 2d$ and $x = 4d$ in the near wake. However, in the far wake region, the difference in velocity gets considerably smaller from $x = 7d$ and $x = 10d$. Furthermore, Figure 4.7 compares these results for each horizontal distance.

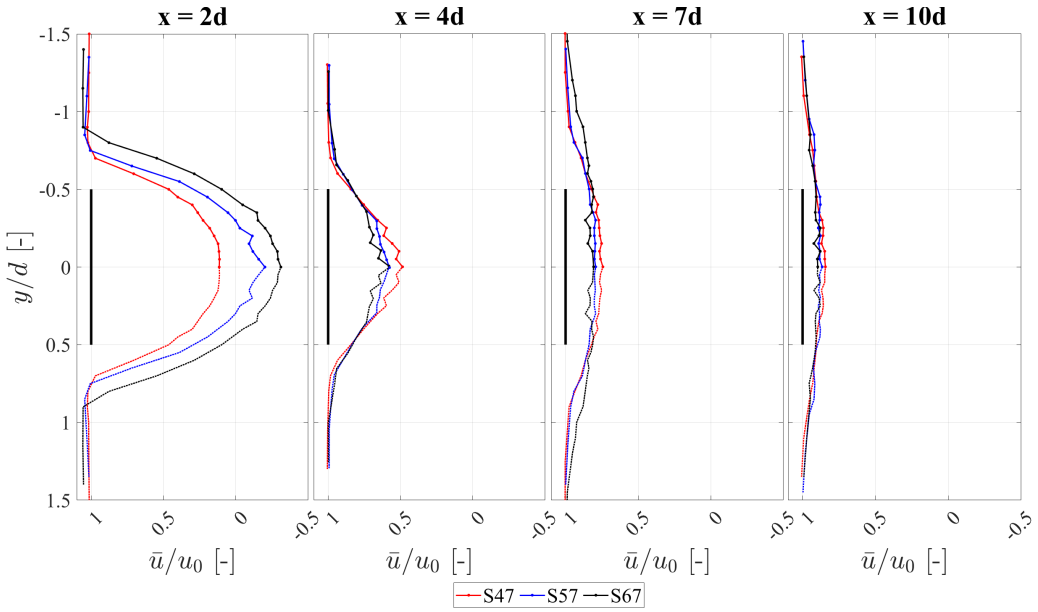

Figure 4.7: *Velocity reduction factor u/u_0 for S47, S57 and S67 at the downstream distances of $x = 2d$, $x = 4d$, $x = 7d$ and $x = 10d$.*

As the figure clearly illustrates, the most significant difference in the velocity reduction is visible in the near wake region, especially at a distance of $x = 2d$. At this horizontal location, the biggest reduction is present for the disc configuration with the highest solidity of 67%, represented as the black curve. S67 is then followed by S57 and then S47. As expected, we have a bigger velocity, the bigger the porosity as we increase the passage possibilities for the flow. Another visible effect is the width and shape of the wake. As the solidity increases, the wake expands. This phenomenon is closely related to the increase of the local blockage ratio, B_L. When the solidity increases, a bigger part of the flow is forced around the structure, creating a wider wake, which is also visible in the downstream region. At a distance of $x = 4d$, S47 and S67 experience rapid fluctuations close to the symmetry line. This could be a case of a high signal-to-noise ratio due to inadequate mixing. Another potential explanation is that the specific measurement point is localized in a jet stream behind one of the holes in the disc structure.

As the flow moves further downstream, the difference in this width shape is less noticeable. As for the velocity reduction, the situation has turned around. The figure shows that the highest velocity reduction is present for S47, closely followed by S57 and S67. This is also the case further downstream, but the curve difference is less comprehensive. In the far wake region at $x = 10d$, the velocity reduction is very similar and closes in on the incoming velocity, u_0.

An overview of the maximum velocity reduction and the wake recovery is presented in Table 4.1. It is essential to specify that the velocity reduction is calculated as one minus the velocity reduction factor (u/u_0).

Table 4.1: *Comparison of max velocity reduction percentage and wake recovery percentage of S47, S57, and S67. Velocity reduction is calculated as 1-(u/u_0)·100%.*

Disc solidity	x/d [-]	Max velocity reduction [%]
S47	2	88.7
	4	51.4
	7	25.7
	10	15.7
S57	2	120.1
	4	42.4
	7	20.8
	10	13.4
S67	2	131.1
	4	42.0
	7	19.3
	10	12.2

It is quite evident that the highest maximum velocity reduction occurs for the S67 at the closest downstream distance, with a velocity reduction of 131.1%. A negative velocity is present, indicating a backflow in the very near wake. However, the wake appears to recover faster, with a reduction of 89.1% in the velocity reduction from $x = 2d$ to $x = 4d$.

Next, the cross-flow profiles are presented in Figure 4.8.

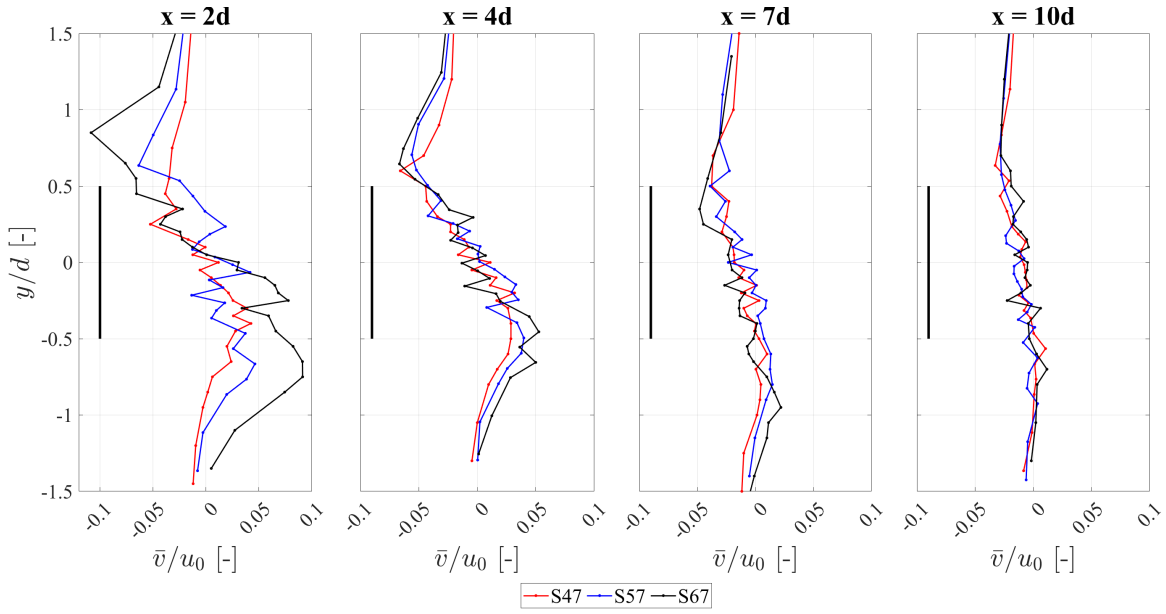

Figure 4.8: *Crossflow comparison between S47, S57 and S67 at the downstream distances of* $x = 2d$, $x = 4d$, $x = 7d$ *and* $x = 10d$.

The figure shows that the cross-flow, $\bar{v}/u_0$, is at its highest in the near wake, at a downstream distance of $x = 2d$. Just outside of the edges of the disc, the vertical velocity component, $\bar{v}$, has its maximum value, corresponding to approximately 10% of the incoming horizontal velocity u_0 for S67. Hence, this leads to higher entrainment from the free stream area, ultimately causing the wake to narrow down, as previously presented in Figure 4.7. The cross-flow reduces as the flow moves further downstream, and the wake expands. Nonetheless, the cross-flow profiles provide a good agreement with the development of the wake's width from the near- to the far wake region.

4.2.3 Turbulent kinetic energy

In order to fully understand the development of the downstream wake, the illustrated velocity profiles must be considered in light of the associated turbulent kinetic energy and cross-flow profiles. These profiles are closely related, providing valuable information on the flow development from the near wake to the far wake. Thus, Figure 4.9 presents the turbulent kinetic energy profiles at the same horizontal distances of $x = 2d$, $x = 4d$, $x = 7d$, and $x = 10d$.

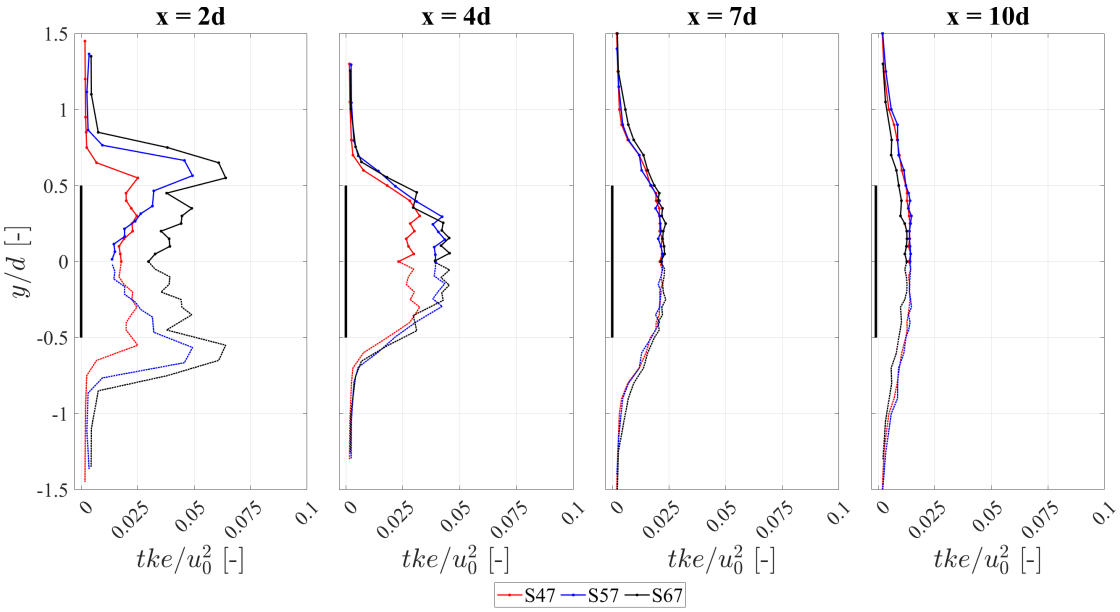

Figure 4.9: *Turbulent kinetic energy for S47, S57, and S67 at the downstream distances of x = 2d, x = 4d, x = 7d, and x = 10d.*

As expected, the highest level of turbulence is present in the near wake at the distances of $x = 2d$ and $x = 4d$. The turbulence increases with an increased solidity, meaning that the highest level of tke is present for the S67 disc. Consequently, S67 experiences a faster recovery of its wake. Hence, explaining why the velocity reduction profile is surpassed by S47 and S57 from $x = 2d$ to $x = 4d$ in Figure 4.7. All curves experience a drop in turbulence as they approach the symmetry line, while the maximum point is localized closer to the edge of the discs. Here, the strongest vortices are expected. As the flow moves further downstream, the difference in turbulence is less significant. However, the turbulence gets reduced as the horizontal distance increases. Additionally, the curves follow a more Gaussian profile, with the turbulence increasing towards the center of the discs.

4.2.4 Shear stresses

In wind turbines, wake recovery is an essential factor that affects the efficiency of energy production. As previously reviewed in Section 2.4, Van der Laan et al. [26] investigated the mechanisms of wake recovery by analyzing the stress divergence for a single rotor. The results showed that the lateral and vertical shear stresses, rather than the normal stresses, were the main contributors to wake recovery. Thus it is important to analyze the lateral shear stress, $u'v'$, and vertical shear stress, $u'w'$, in the downstream wake. Figure 4.10 presents these results at a downstream distance of $x = 2d$.

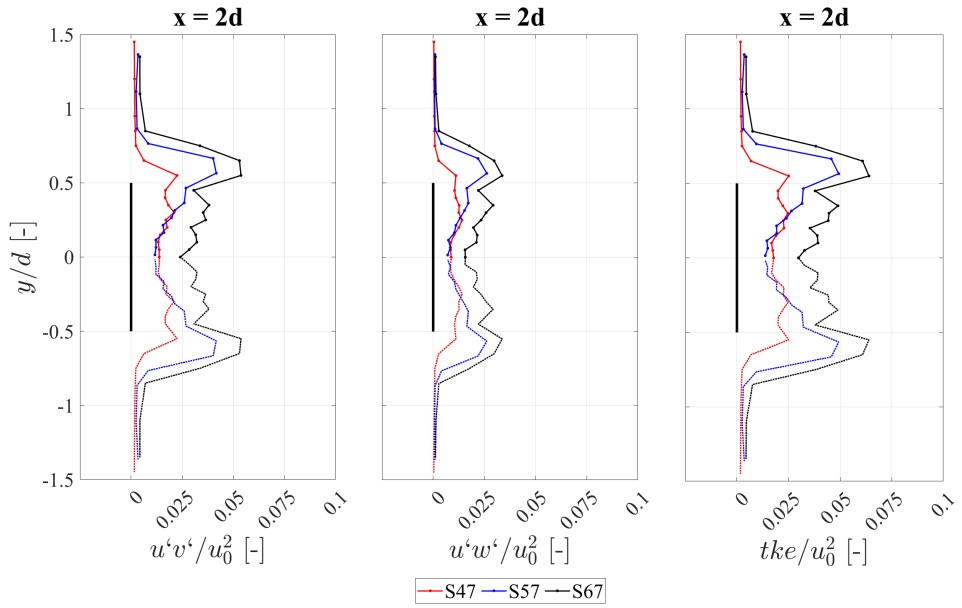

Figure 4.10: *A comparison between the shear stresses $u'v'$, $u'w'$, and tke for S47, S57, and S67 at the downstream distance of $x = 2d$.*

Figure 4.10 shows that the highest shear stresses occur at the disc's edges. This is as expected as the wake mixes with the free stream region, resulting in higher velocity fluctuations. Notably, the lateral shear stress surpasses the vertical shear stress, aligning with the findings commonly observed in turbulent flows [26]. In turbulent flows, energy transfer predominantly occurs in the lateral direction, yielding greater lateral velocity gradients and, consequently, elevated lateral shear stress levels. The highest shear stresses here have the same location as normal stresses in tke,

4.3 ADV measurements: MR7

The following subsections will present the ADV-based results for the velocity reduction and turbulent kinetic energy in the wake of MR7. Initially, an overview of the different obtained full-flow field measurements will be illustrated before differences and similarities between wake profiles will be reviewed. The results will then be a subject of discussion in light of similar, previous research performed by Koi [20] and Skoland [19]. These results will be considered and discussed from an upstream and downstream perspective.

4.3.1 Full-field mean velocity

The downstream and upstream measurements in the experimental campaign were done in accordance with the method explained in Section 3.5.2 and Table 3.7. All the obtained data were then gathered and presented as wake profiles, which will be further reviewed in Section 4.3.2 and 4.3.3. However, the following two Figures, 4.11 and 4.12, illustrate the velocity reduction from a bigger perspective. These flow fields are based on both the performed upstream and downstream measurements. Once again, it is important to specify that the horizontal distances at which the actual measurements were done are marked with a white dashed line. In between these horizontal distances, the obtained values are based on an interpolated approach, the *makima* function, in MATLAB during the post-processing phase.

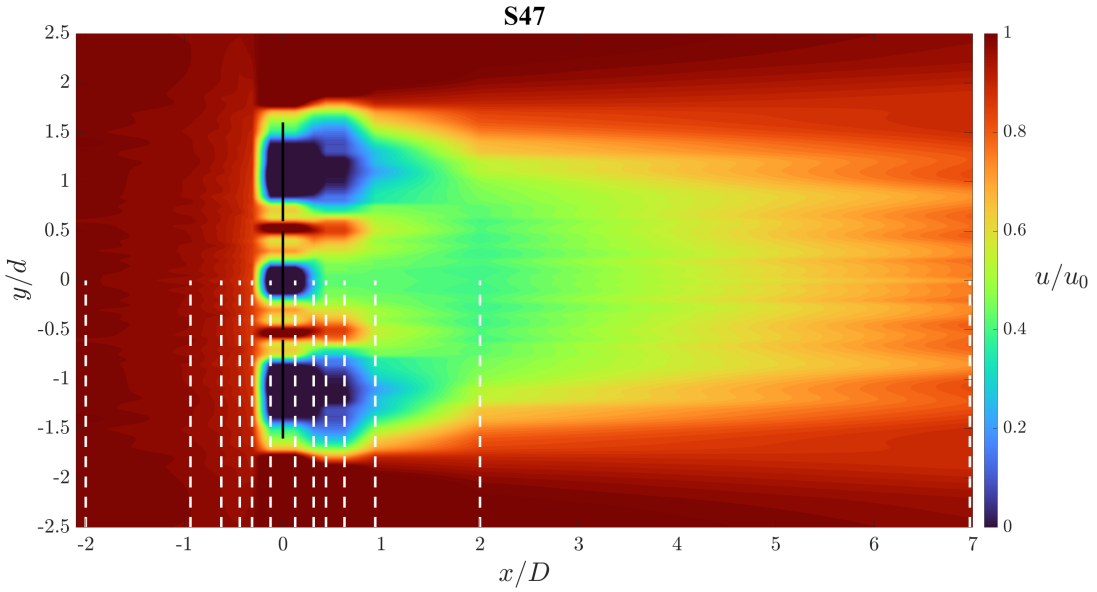

Figure 4.11: *Full flow field for S47 illustrating the velocity reduction, u/u_0, from x = -2D to $x = 10D$. The horizontal distances for the measurements are represented as a white dashed line, while the in-between regions are based on interpolated values.*

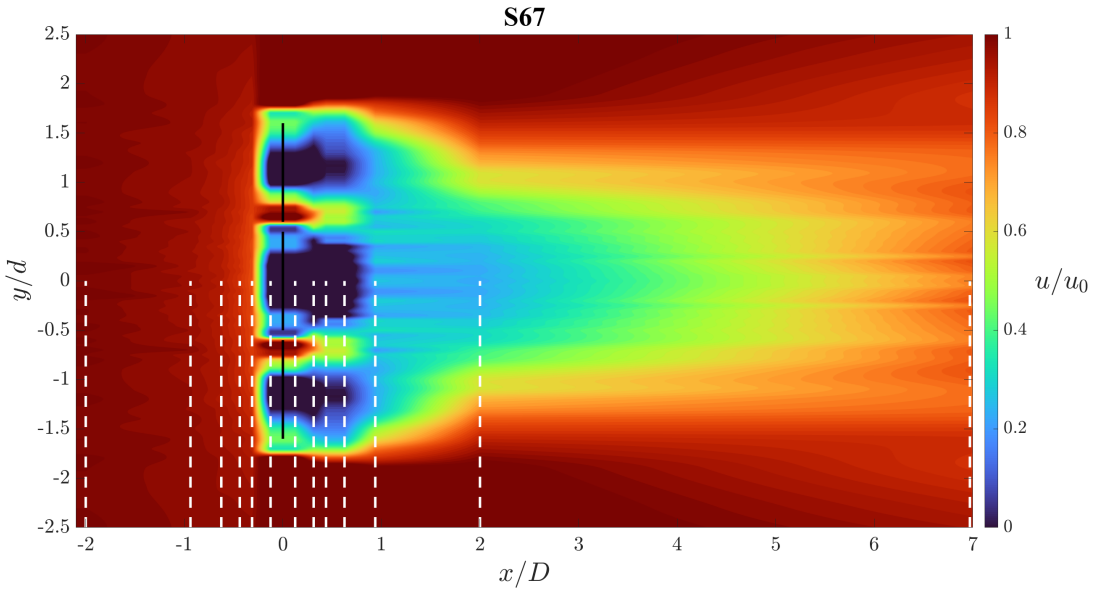

Figure 4.12: *Full flow field for S67 illustrating the velocity reduction, u/u_0, from x = -2D to $x = 10D$. The horizontal distances for the measurements are represented as white dashed lines, while the in-between regions are based on interpolated values.*

The above figures illustrate a clear difference in how the velocity acts at different regions, both from an upstream and downstream perspective. Generally, the velocity reduction is higher for S67 compared to S47. This is especially visible towards the center of the disc configuration, where the difference in solidity lies. The velocity reduction is more excessive in both vertical and horizontal directions along the symmetry line. However, at the locations closer to the edges of the discs, the difference in velocity shape is less significant. Due to the increase in solidity, the width of the wake is expanded. The local blockage increases by increasing the solidity, displacing the local jet stream between the lateral discs. The following subsections will highlight this, where the associated velocity and tke profiles will be reviewed extensively.

4.3.2 Upstream flow measurements

The upstream measurements of the velocity reduction were performed in accordance with Table 3.7. The flow field results are illustrated further in Figure 4.13.

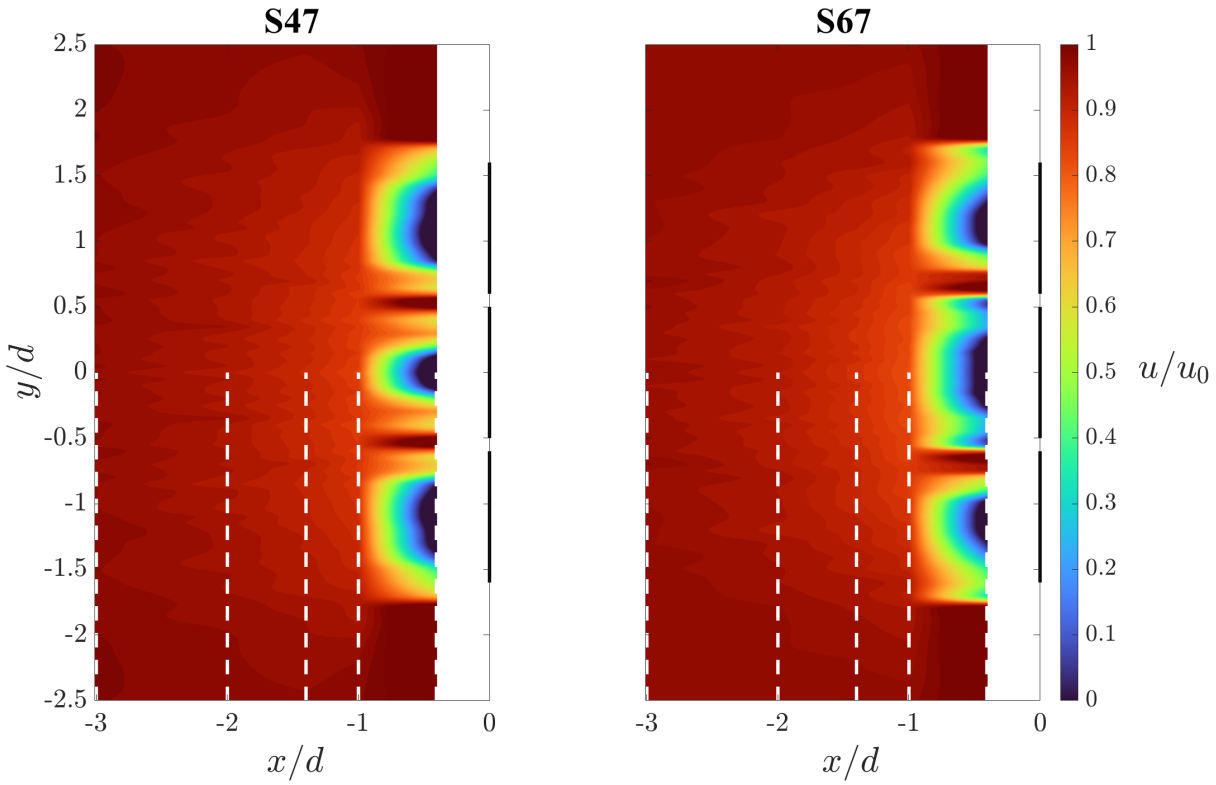

Figure 4.13: *The upstream flow field of the velocity reduction for S47 and S67, from x = -3d to x = 1d. The white dashed lines represent the measurement points, while the in-between regions are based on interpolated values.*

The figures above show an overview of the upstream measurements of the velocity reduction based on a flow field. The vertical dashed lines represent the performed measurements, while the rest is based on interpolated values. As the figures clearly illustrate, the blockage effect occurs at the same horizontal distance, drastically increasing the reduction from a distance of x = -1d. Although the reduction follows a similar pattern in terms of how it varies with the horizontal distance, the extent of the reduction is more significant for S67 compared to S47. Due to the higher blockage ratio, the upstream velocity reduction is visibly wider for S67, causing the wake to expand. This is further highlighted in Figure 4.14, illustrating the individual upstream profiles for S47, S57, and S67, respectively.

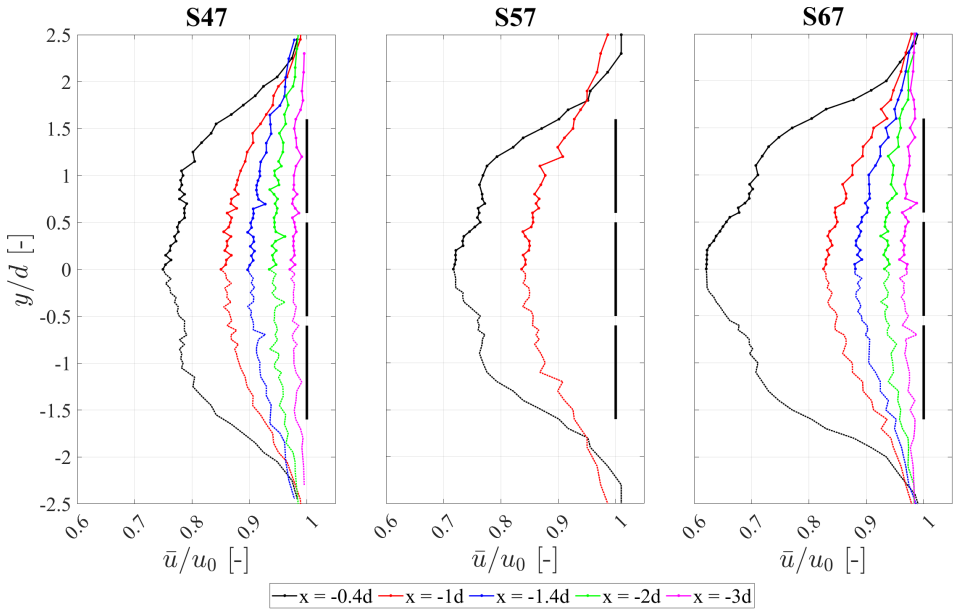

Figure 4.14: *Upstream velocity reduction measurements for MR7 with a center disc solidity of 47%, 57%, and 67%, respectively.*

The figure illustrates the horizontal locations where the upstream profiles were measured. All the curves follow a consistent pattern, with the velocity reduction increasing as the measurement location gets closer to the disc configuration. Additionally, the curve difference gets more prominent as the flow approaches the discs. In order to gain further insights into the variations in reduction based on different center disc solidities, it is valuable to compare the results at each isolated distance. Hence, Figure 4.15 shows these comparisons.

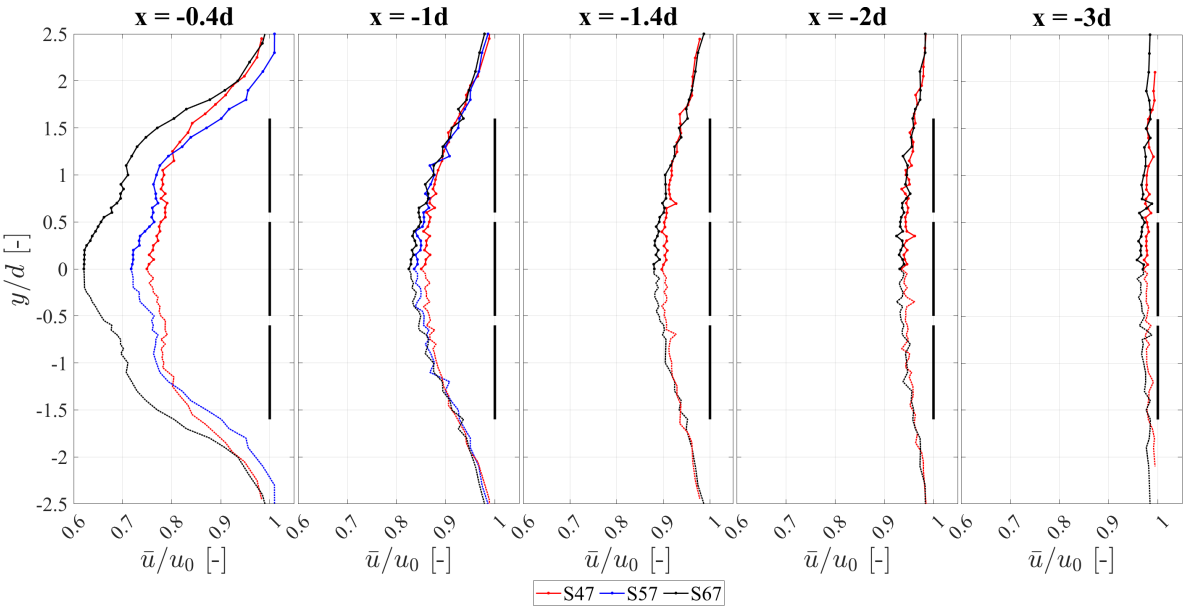

Figure 4.15: *A comparison between the wake profiles of S47, S57 and S67 at the downstream distances of x = -0.4d, x = -1d, x = -1.4d x = -2d, and x = -3d.*

As expected, the velocity reduction is more prominent for the multirotor configuration with the highest center disc solidity of 67% due to the increasing local blockage ratio and thereby increasing the resulting induction factor, a. This velocity difference is considerably larger at the nearest upstream distance of $x = 0.4d$. However, the difference between the velocity reduction decreases for the remaining upstream distances. Furthermore, Table 4.2 presents the maximum velocity reduction percentage of the incoming velocity u_0, based on the different disc solidities and upstream distances.

Table 4.2: *Comparison of max velocity reduction percentage of MR7 with the different centre disc solidities of S47, S57, and S67.*

Disc solidity	x/d [-]	Max velocity reduction [%]
S47	-0.4	25.1
	-1	15.0
	-1.4	10.3
	-2	6.6
	-3	3.0
S57	-0.4	28.3
	-1	16.4
	-1.4	-
	-2	-
	-3	-
S67	-0.4	37.9
	-1	17.5
	-1.4	12.0
	-2	7.5
	-3	4.2

The table shows that the most significant difference in maximum velocity reduction percentage is between S57 and S67. By increasing the disc solidity by 10% from S57 to S67, the reduction also increases by 10%. Next, it will be of interest to investigate how the increased blockage effect upstream influences the flow further downstream. Hence, the following sections will look at this from a downstream perspective.

4.3.3 Downstream mean velocity reductions

The downstream measurements were done in the same procedure as the upstream measurements. The recordings were registered as the carriage was moved back to its starting position. The first measurements, illustrated in Figure 4.16, show how the velocity reduction varies with the horizontal downstream distance for each center disc setup.

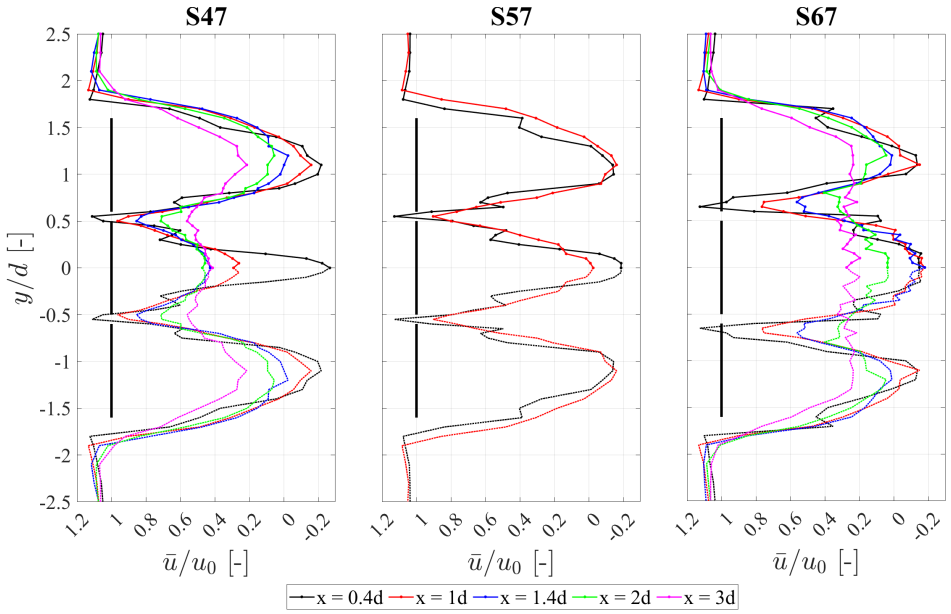

Figure 4.16: *Very near wake velocity reduction for MR7 for S47, S57, and S67.*

As expected, the velocity reduction is most prominent at the nearest downstream location of $x = 0.4d$. As the flow moves further downstream, this reduction gets reduced. Furthermore, each wake profile will be compared at the isolated downstream distances in Figure 4.17.

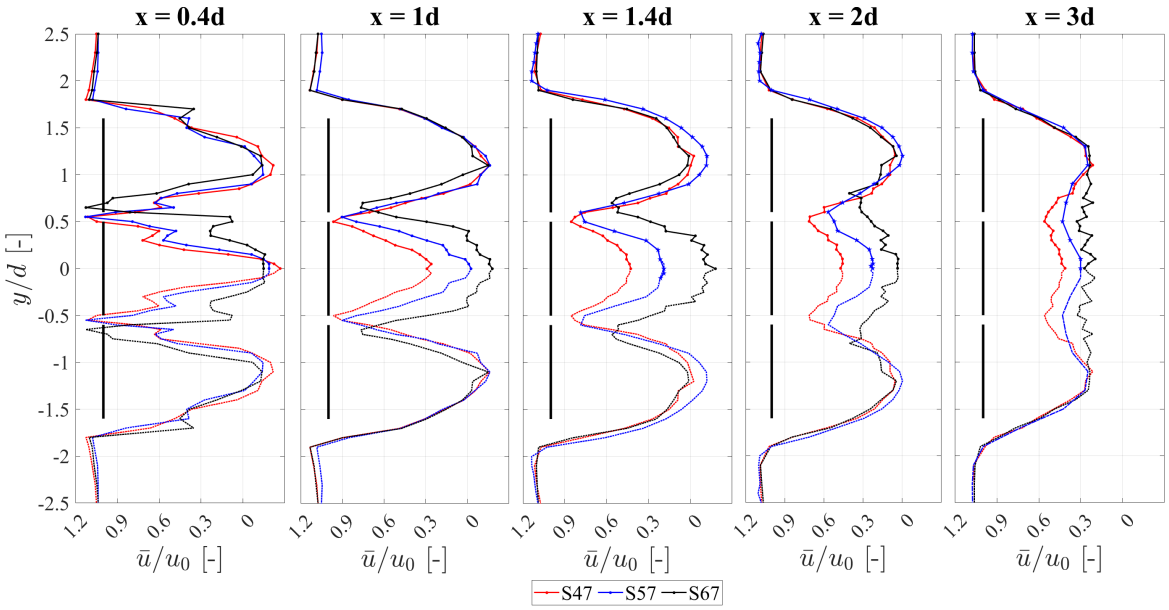

Figure 4.17: *A comparison between the very near wake profiles of S47, S57, and S67 at the downstream distances of $x = 0.4d$, $1d$, $1.4d$, $2d$, and $3d$. The S57-based measurements between $x = 1.4d$ - $x = 3d$ is provided by Skoland [19].*

Based on the curves from the above figure, it is evident that S67 has the biggest reduction in velocity, followed by S57 and S67. A key result from the wake development is how the jet

streams localized between the discs expand as the disc solidity and blockage ratio increases. The bigger the blockage and center disc solidity, the wider the wake around the center disc. However, the wake around the discs at the configuration's edges does not expand, leaving the shape of the local wake unchanged. Nonetheless, the increased center disc solidity contributes to a wider wake around the center disc, a repetitive pattern through all horizontal downstream distances. A smaller difference in the velocity reduction is observed at a downstream distance of $x = 3d$, while the curve representing S67 is more evened out.

The increased blockage clearly affects the velocity in the very near wake region. Furthermore, it will be interesting to observe what happens further downstream, in the near and far wake, respectively. Figure 4.18 represents the obtained data for S47, S57, and S67 for $x = 2D$ and $x = 7D$, while Figure 4.19 further compares them based on each downstream distance.

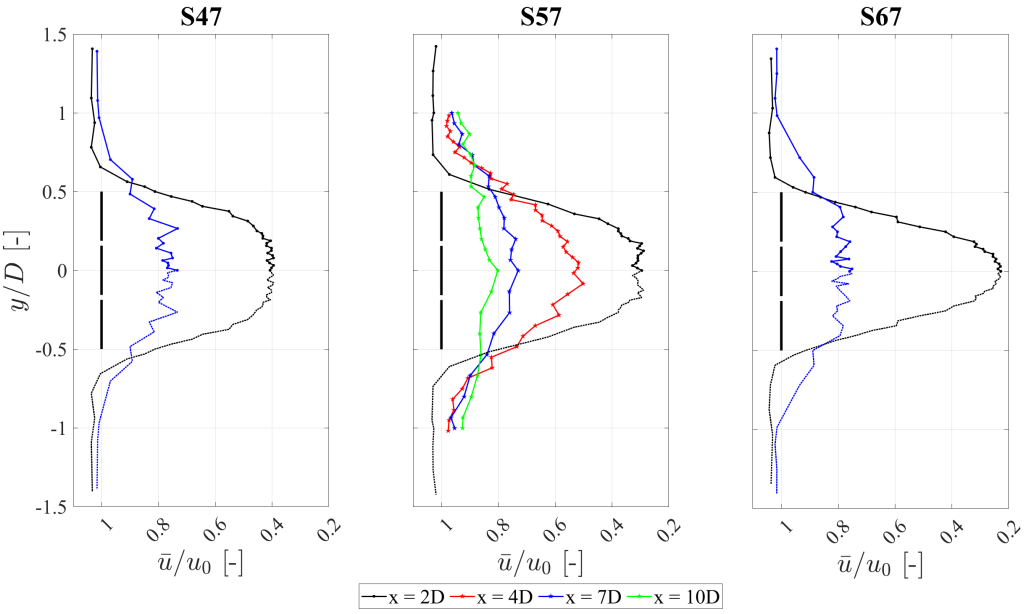

Figure 4.18: *Downstream velocity reduction measurements at x = 2D and x = 7D, for S47, S57, and S67.*

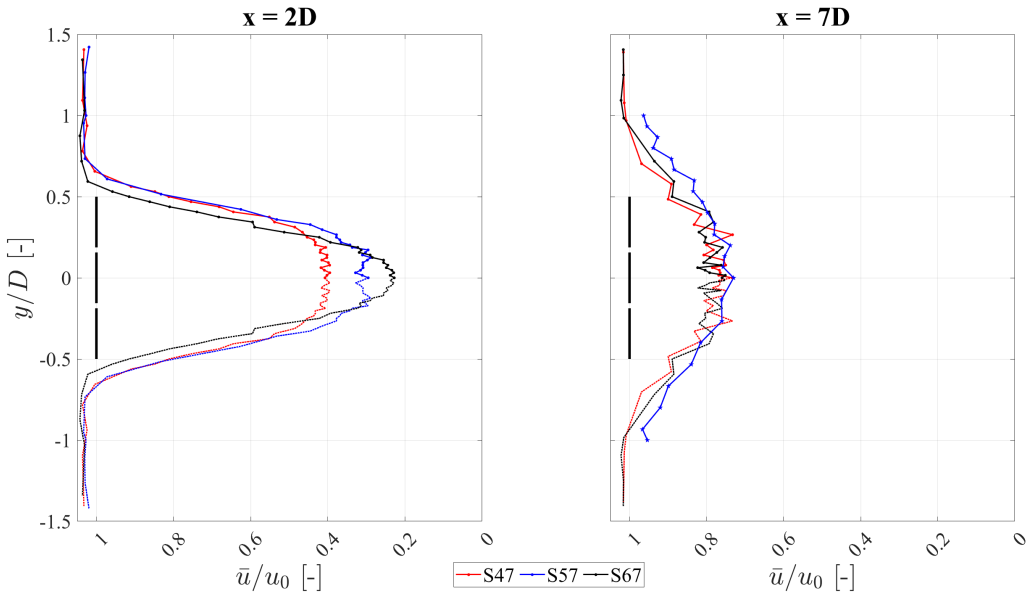

Figure 4.19: *Downstream velocity reduction measurements at x = 2D and x = 7D, for S47, S57, and S67. The S57-based measurement at x = 7D is provided by Skoland [19].*

The velocity reduction gets considerably lower as the flow moves from the near wake to the far wake. Additionally, the shape of the wake gets wider. The curve representing S67 has the highest velocity reduction in the near wake at $x = 2D$. However, at a distance of $x = 7D$, the curves more or less coincide, indicating a faster recovery of the wake for the higher center disc solidity. Table 4.3 summarizes the results for the maximum velocity reduction from the very near wake to the far wake.

Table 4.3: *Comparison of the velocity reduction in percentage ($(1-(u/u_0))\cdot 100$).*

	S47		**S57**		**S67**	
x/d (very near wake) [-]	**Center**	**Edgde**	**Center**	**Edge**	**Center**	**Edge**
0.4	126.8	121.8	118.8	114.4	114.9	113.7
1	74.0	115.9	102.6	116.2	118.0	115.0
1.4	57.3	102.5	-	-	118.0	98.9
2	54.3	94.5	-	-	96.9	95.5
3	58.8	78.6	-	-	80.3	77.2
x/D (far vs near wake) [-]	**Center**		**Center**		**Center**	
2	60.5		70.5		77.2	
7	26.6		-		24.9	

As both the curves and table values indicate, the most considerable maximum velocity reduction appears for S47 at the closest downstream distance of $x = 0.4d$. As the flow moves further downstream, S67 has the highest reduction, surpassing S47. Another interesting point

is where the maximum point appears. For S67, the maximum velocity reduction occurs for the center disc, with the lower reduction at the neighboring discs. However, for S47 and S57, the situation is turned around, with the maximum velocity reduction located at the outer discs of the MR7 configuration.

Furthermore, an examination of the cross-flow profiles becomes crucial for studying the relationship between wake shape development and the velocity profiles depicted in Figure 4.17.

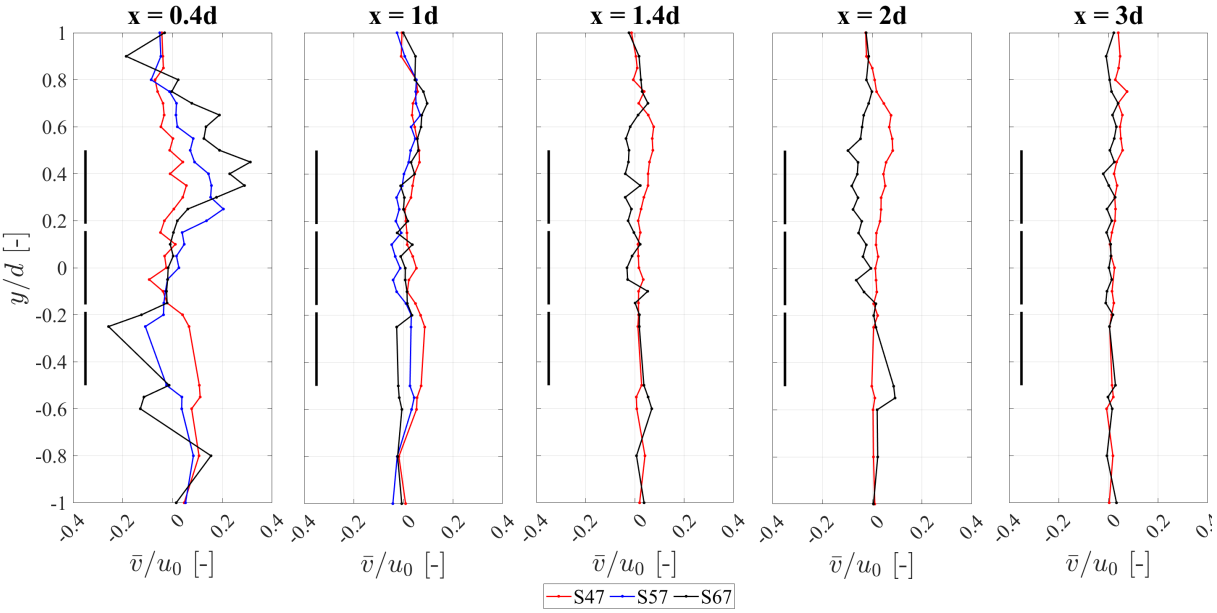

Figure 4.20: *Crossflow MR7 comparison between S47, S57 and S67 at the downstream distances of x = 0.4d, 1d, 1.4d, 2d, and 3d.*

A higher cross-flow is present for the S67 configuration, closely followed by S57 and S47. Thus, a higher flow entrainment from the free stream appears for S67, leading to a more narrow wake. This could explain why the velocity profile curves coincide around the outer discs in Figure 4.17. Due to the higher center disc solidity, the wake expansion for S67 is higher around the center disc. A similar pattern around the outer disc was expected. However, the significantly larger cross-flow around the outer disc could contribute to narrowing down the wake expansion, causing a similar curve pattern at this location.

In order to fully understand the development of the flow in the wake, the turbulent kinetic energy and shear stresses need to be reviewed. Thus, the next section will investigate these profiles and put them into the context of the velocity profiles.

4.3.4 Turbulent kinetic energy

Figure 4.21 provides an overview of the turbulent kinetic energy in the near wake.

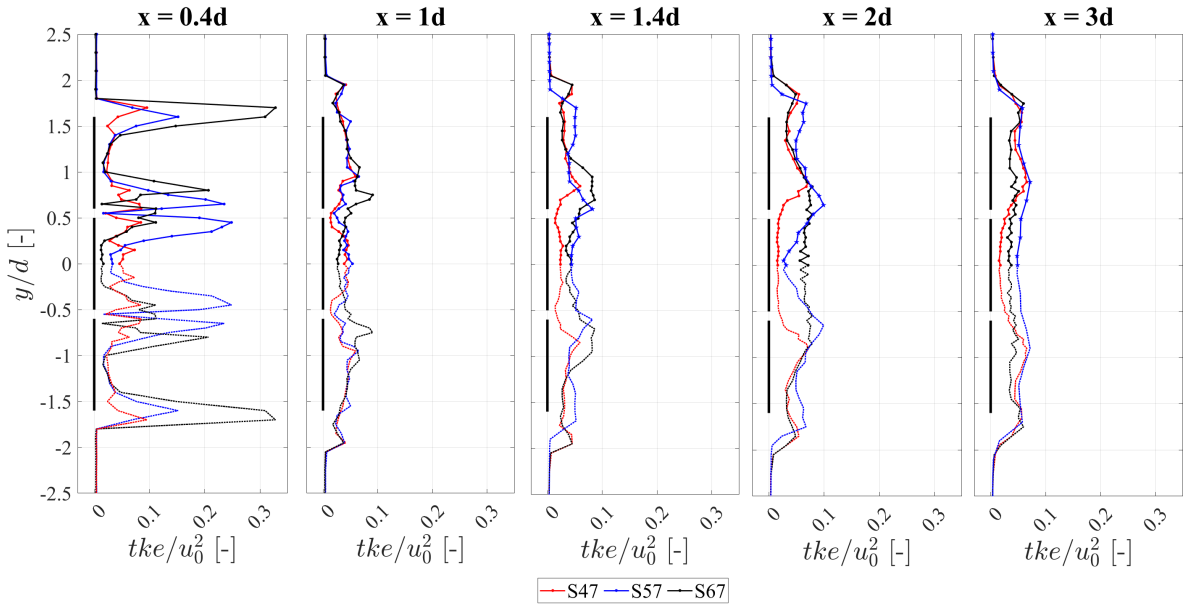

Figure 4.21: *Turbulent kinetic energy at x = 0.4d, 1d, 1.4d, 2d, and 3d for the MR7's different center disc solidities.*

The highest turbulent kinetic energy appears in between the discs, as well as at the edge of the outer discs. The kinetic energy is lower in the middle of the center disc and the lateral discs. At a downstream distance of $x = 0.4d$, S67 has the highest tke for the outer discs, while S57 has the highest tke between the discs. As the flow moves further downstream in the very near wake, the differences are more evened out, with the tke of the S67 disc being slightly higher. A clear relation is evident by studying these details in light of the velocity profiles given in Figure 4.17. Due to the tke being higher for S67, a faster recovery of the velocity reduction occurs. This is because the difference between the velocity profiles gets reduced more and more as the wake moves up to $x = 3d$.

Furthermore, the tke for the near and far wake is compared in Figure 4.22.

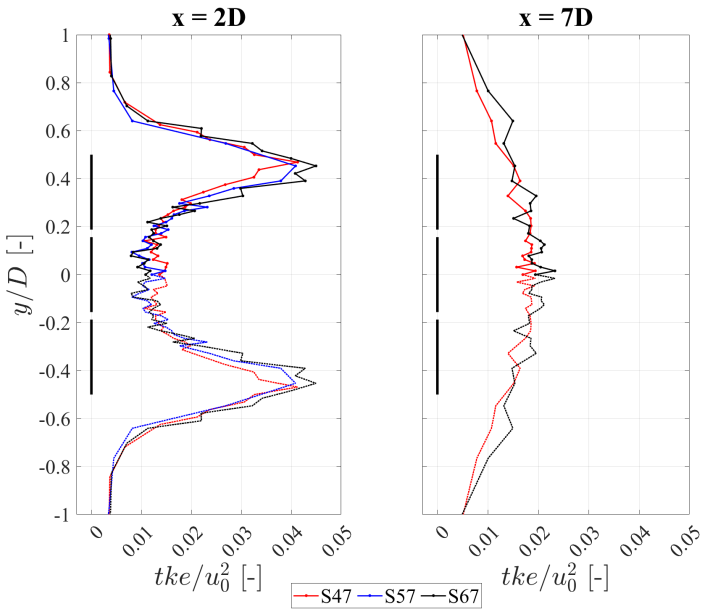

Figure 4.22: *Turbulent kinetic energy for MR7 at the downstream distances of $x = 2D$ and $x = 7D$.*

As Figure 4.22 shows, there is no significant difference in tke level between the different multirotor setups at either of the downstream distances. The difference between the curves was more comprehensive around a single disc. However, despite different center disc solidities, these differences are reduced when introducing lateral disc in an MR7 setup. When moving from $x = 2D$ to $x = 7D$, the tke level decreases, as expected.

4.3.5 Shear stresses

As previously highlighted in Section 4.2.4, the lateral and vertical shear stress is the main mechanism behind wake recovery. Figure 4.23 presents these results for MR7 at a downstream distance of $x = 1d$.

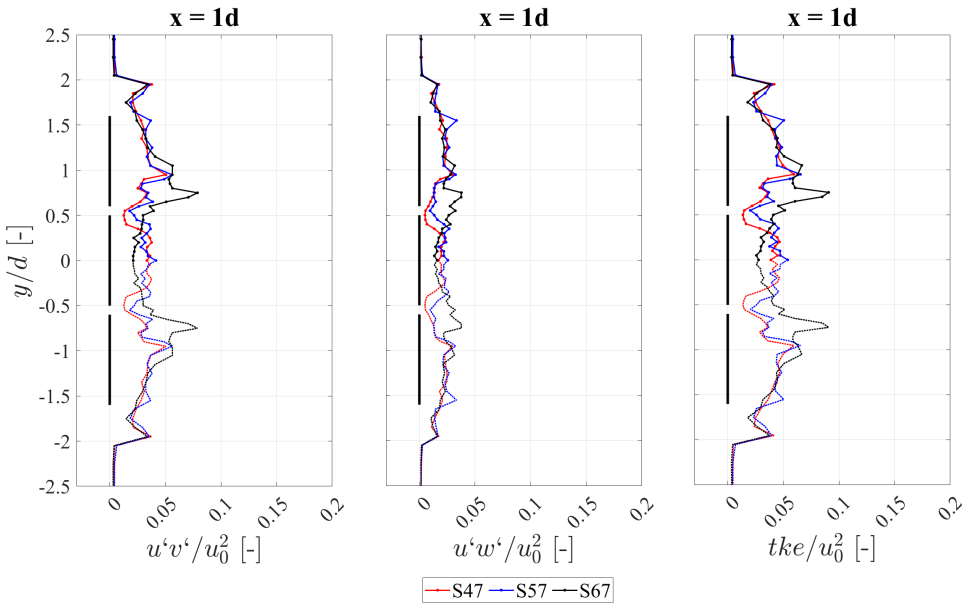

Figure 4.23: *A comparison between shear stresses $u'v'$, $u'w'$, and tke for S47, S57, and S67 at the downstream distance of $x = 2d$.*

Similar to the SR results, the lateral shear stress is dominant for the MR7 wake. The tendencies of the curves, with the highest shear stresses occurring near the discs' edges, are consistent with the turbulent kinetic energy results.

4.4 PIV measurements in the SR wake

The PIV measurements were done in accordance with the procedure described in Section 3.5.3. Figure 4.24 presents the full flow field based on the acquired vertical velocity profiles taken by the PIV system. Similar to the ADV measurement campaign, the *makima* function from MATLAB is used to calculate the interpolated values between the horizontal distances at which the measurements were performed.

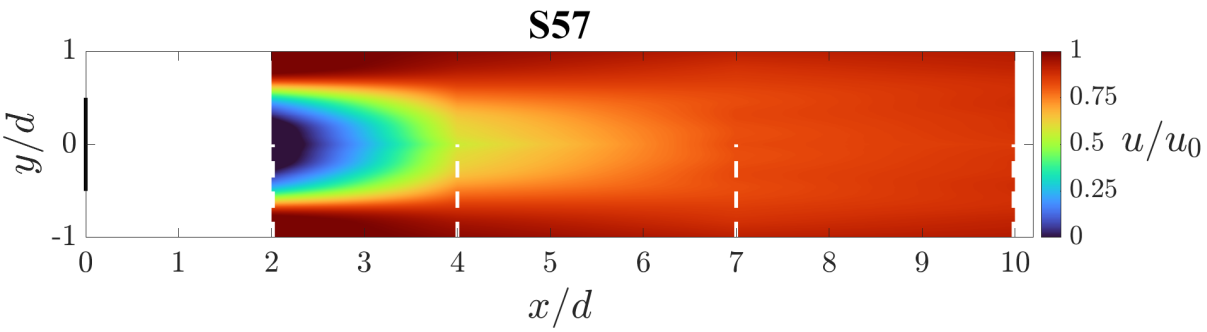

Figure 4.24: *Full-field mean velocity reduction in the wake of SR (S57) based on the PIV measurement campaign. The white dashed lines represent the horizontal distances at which the measurements were performed.*

Based on the acquired particle tracks from the STB module, vertical velocity profiles at given distances, previously highlighted in Figure 3.17, were extracted. Figure 4.25 summarizes the velocity reduction profiles for SR at these downstream distances.

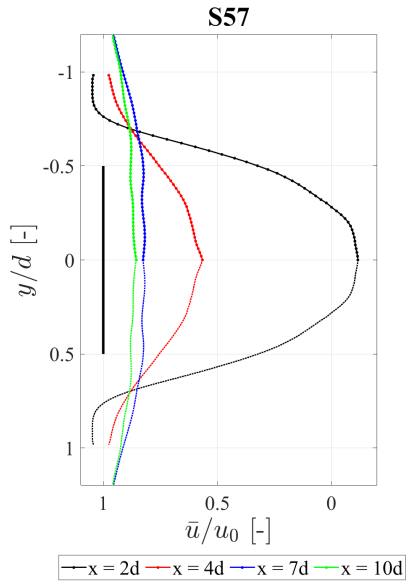

Figure 4.25: *Comparison between the velocity reduction PIV-results for SR, at x = 2d, 4d, 7d, and 10d.*

The velocity reduction gets higher as the flow moves further downstream. Additionally, the wake expands. Furthermore, the maximum velocity reduction percentage is presented in Table 4.4.

Table 4.4: *Comparison of the velocity reduction in percentage* $((1-(u/u_0))\cdot 100)$

S57	**SR**
x/d (near and far wake) [-]	**Center**
2	111.6
4	43.5
7	18.2
10	14.5

Table 4.4 shows that the velocity reduction from $x = 2d$ to $x = 4d$ is reduced by almost 60%, before eventually stabilizing in the far wake at $x = 10d$.

Furthermore, the tke results for SR are illustrated in Figure 4.26.

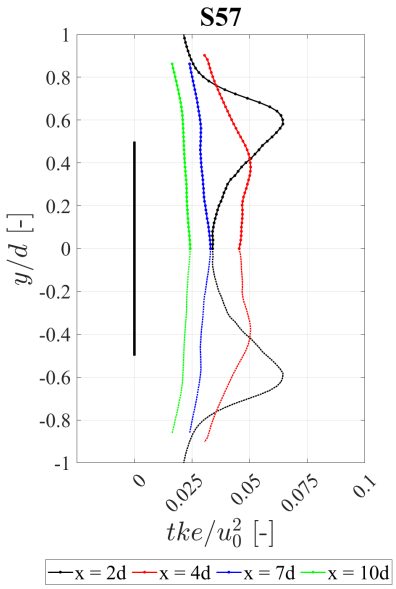

Figure 4.26: *Comparison between the tke PIV-results for SR, at* $x = 2d$, $4d$, $7d$, *and* $10d$.

Figure 4.26 shows that the tke is highest at a distance of $x = 2d$, more specifically at the edges of the disc. Further down the wake, the tke level drops, as expected. However, the tke curves were expected to converge to zero in the free stream region, which was not the case. This will be further discussed in Section 4.6.1.

4.5 PIV measurements in the MR7 wake

Figure 4.27 presents the full-field mean velocity based on the acquired vertical velocity profiles taken by the PIV system. The data evaluation focuses on the near wake up to $x = 2D$, while results measured at $x = 4D$-$10D$ have not yet been evaluated due to time restrictions. Similar to the ADV measurement campaign, the *makima* function from MATLAB is used to calculate the linearity between the horizontal distances at which the measurements were performed.

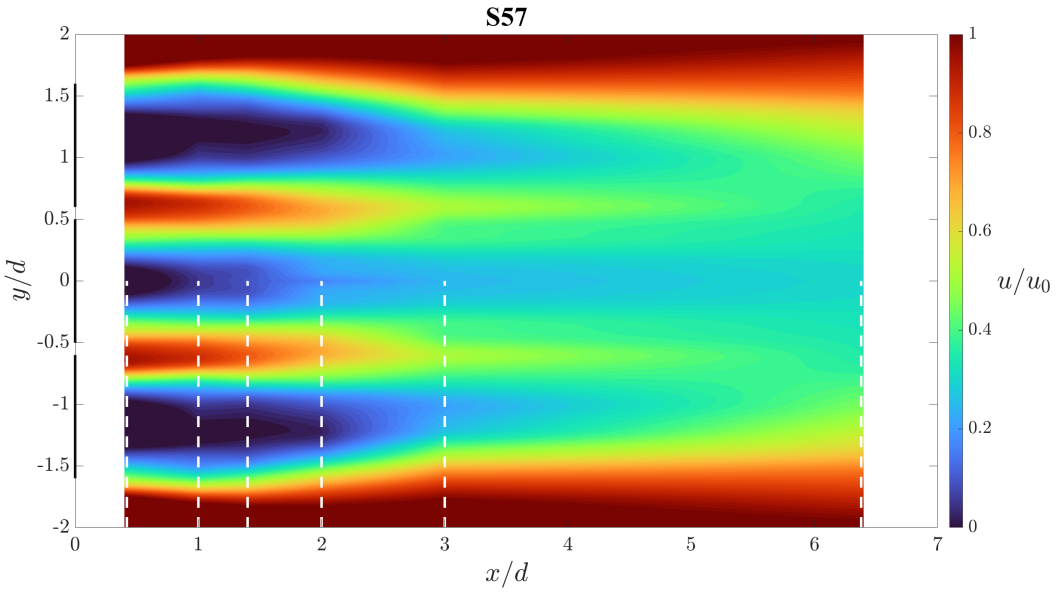

Figure 4.27: *Full-field mean velocity reduction in the wake of MR7 (S57) based on the PIV measurement campaign. The white dashed lines represent the horizontal distances at which the measurements were performed.*

Figure 4.28 illustrates the results for each downstream distance from $x = 0.4d$ to $2D$.

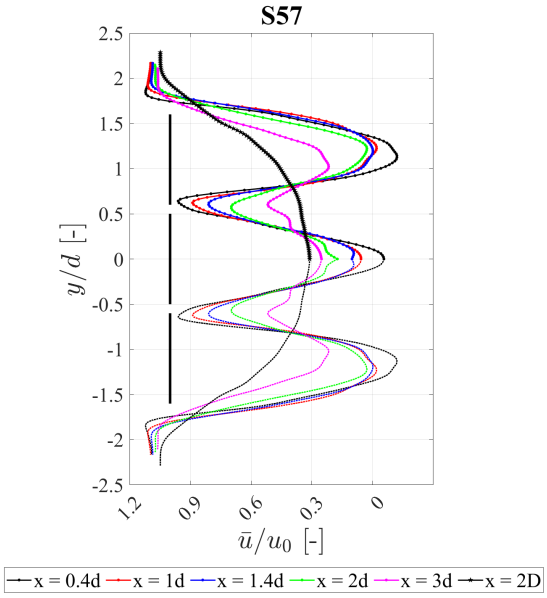

Figure 4.28: *PIV velocity reduction results for MR7, at x = 2d, 4d, 7d, 10d, and 2D.*

The above wake profiles have a consistent trend. The velocity reduction behind the center and outer discs reduces by increasing the downstream distance. The highest jet stream velocity is at the nearest downstream distance of $x = 0.4d$. A high turbulent kinetic energy and mixing are present in the very near wake region. Hence the jet stream velocity reduces by increasing the downstream distance before being completely wiped out at $x = 2D$. Furthermore, Table 4.5 presents the maximum velocity reduction in percentage, both at the discs' edge and center.

Table 4.5: *Comparison of the velocity reduction in percentage: (1-(u/ u$_0$))·100.*

MR7	**S57**	
x/d (very near wake) [-]	**Center**	**Edgde**
0.4	126.8	121.8
1	74.0	115.9
1.4	57.3	102.5
2	54.3	94.5
3	58.8	78.6
x/D (near wake) [-]	**Center**	
2	60.5	

As the table highlights, the velocity reduction is higher at the center of the MR7 configuration at $x = 0.4d$. When moving further downstream, the velocity loss is consequently higher at the center point of the outer discs. Up to $x = 1.4d$, the flow is actually still moving in a negative x-direction. At $x = 2D$, the distinct velocity wakes surrounding the outer discs are evened out.

The PIV-based tke results for MR7 are further illustrated in Figure 4.29.

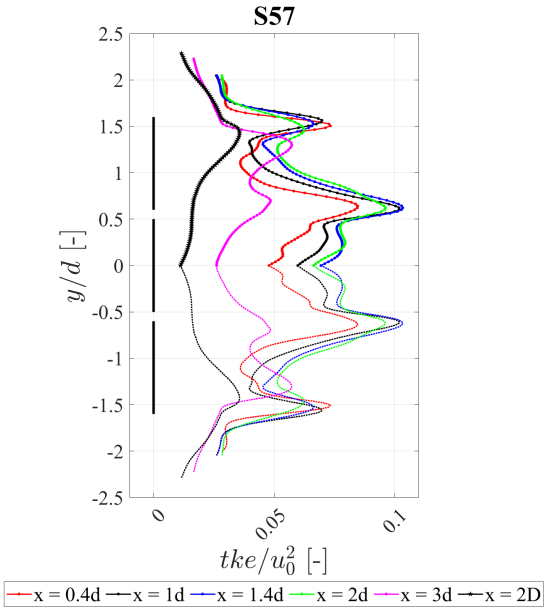

Figure 4.29: *PIV tke results for MR7, at x = 2d, 4d, 7d, 10d, and 2D.*

As the figure demonstrates, the tke level drops by an increased downstream distance. The highest peaks are present between the discs, enhanced by the local jet streams. This peak reduces as the flow progresses, before being evened out at $x = 2D$. A lower peak is observable in the shear layer between the wake and free stream. Similar to the SR results, none of the curves converge to zero in the free stream region. This will also be discussed in Section 4.6.2.

4.6 Discussion

In the following section, the results will be analyzed and discussed. First, the ADV- and PIV-based results will be compared. Then, the wake recovery will be compared between SR and MR7 before being placed in the context of previous experimental research.

4.6.1 Comparison between the ADV- and PIV- based SR results

The results from the ADV- and PIV-based experiments for SR will now be compared and analyzed in detail. Figure 4.32 compares the obtained velocity profiles.

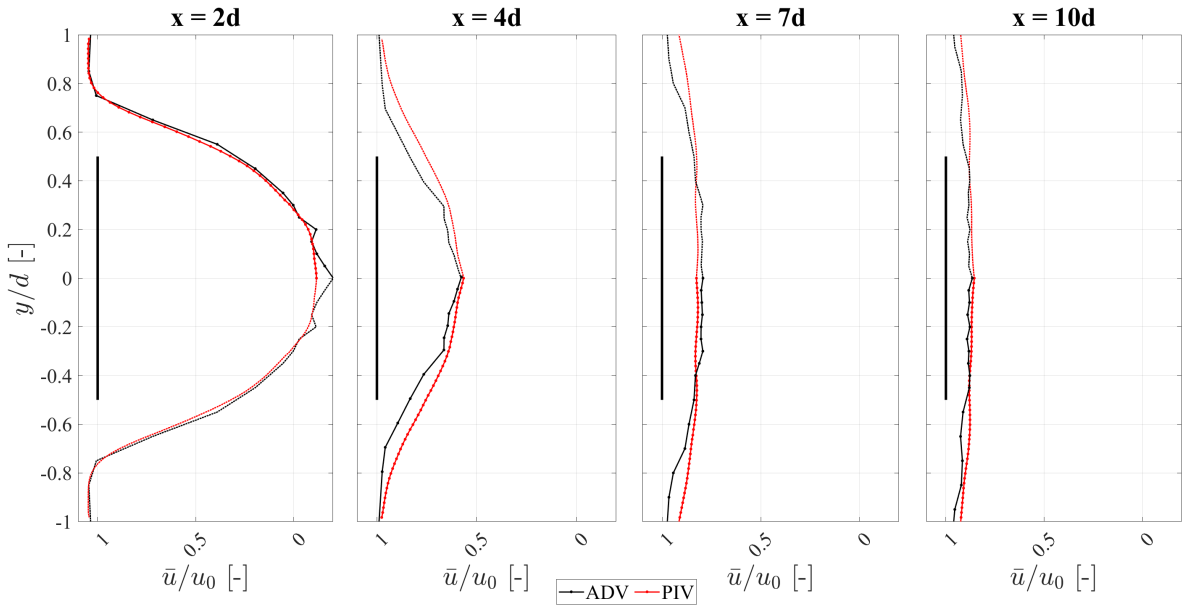

Figure 4.30: *Comparison between ADV and PIV results for SR, at $x = 2d$, $4d$, $7d$, and $10d$.*

By studying the figure, it is evident that both techniques yield consistent outcomes regarding velocity reduction throughout the range of x values from $2d$ to $10d$. The profiles match in terms of velocity reduction and wake width at $x = 2d$. However, in proximity to the symmetry line, the ADV curve exhibits sudden fluctuations observed in numerous ADV measurements. Conversely, the PIV curve displays a smoother pattern. This difference may be due to the small sample size for the ADV. Only one experimental run was executed for each point along the y-axis, which could have been inadequate in terms of generating more representative data.

As the flow progresses towards the far wake, the velocity reduction goes down while the wake width increases. This width is slightly higher for the PIV measurements, indicating a slower wake recovery around the discs' outer edges. The biggest wake recovery appears in the near wake region between $x = 2d$ and $4d$ due to the higher Reynold's shear stress, turbulent kinetic energy, and cross-stream, previously highlighted in 4.2.3.

Furthermore, the acquired tke results from the ADV and PIV measurements are compared in Figure 4.32.

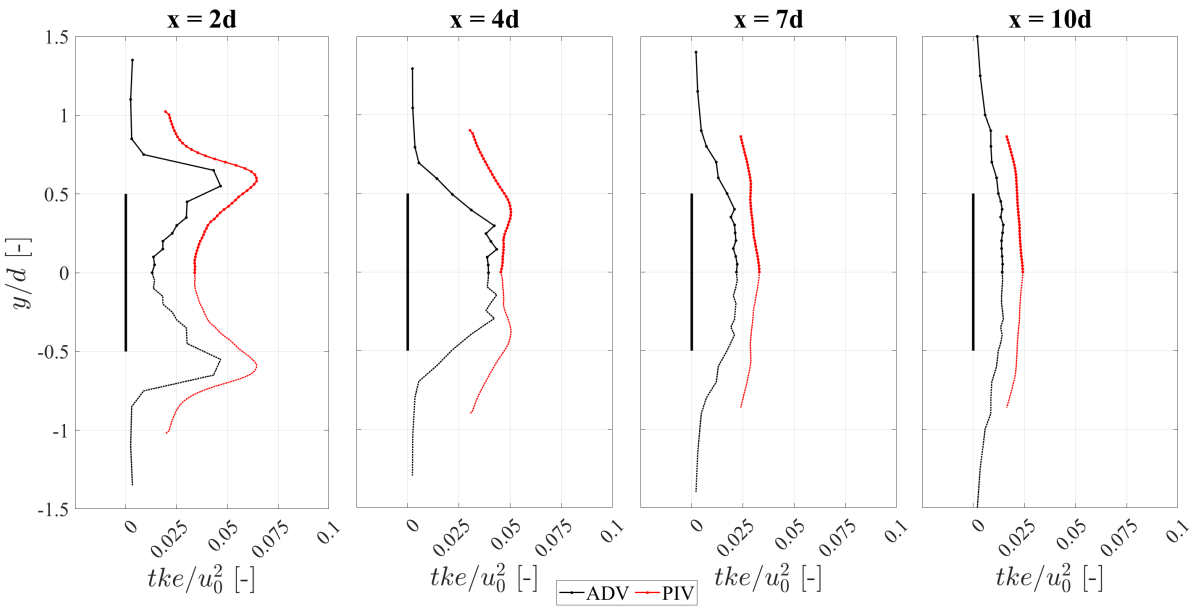

Figure 4.31: *Comparison between ADV and PIV tke results for SR at x = 2d, 4d, 7d, and 10d.*

As shown in the figure, the tke values obtained from PIV are significantly higher than those from ADV. Moreover, unlike the expected behavior of approaching zero in the free-stream region outside the discs, the tke values do not converge to zero. This observation raises a question about the underlying causes of the significant difference in tke results. In order to investigate this issue, the individual normal stresses were isolated by analyzing each of the three velocity components, as illustrated in Figure 4.32.

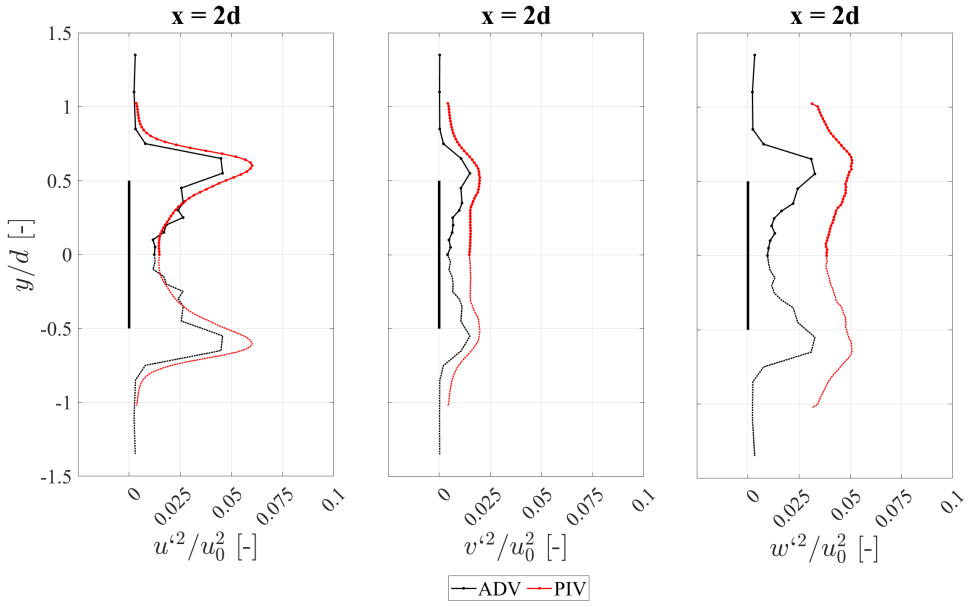

Figure 4.32: *Comparison between ADV and PIV normal stress results for SR at x = 2d.*

The figure shows that the normal stresses $u'u'$ and $v'v'$ are similar, with expected zero values

in the free-stream region outside the discs. However, a notable difference in the third normal stress, $w'w'$, explains the mismatch in tke values. A possible explanation for this behavior can be traced back to an observed oscillation of the submerged multi-camera during the experiment. The weight of the multi-camera setup was too heavy for the aluminum arm on which it was mounted, resulting in induced vibrations and a heave motion in z-direction. Therefore, the multi-camera oscillated during the experiment, potentially influencing the w-component of velocity, which led to the observed differences in tke values between the PIV and ADV results.

4.6.2 Comparison between the ADV- and PIV- based MR7 results

The ADV- and PIV-based results for the very near wake will now be analyzed and compared in detail. Figure 4.33 summarizes these results for each isolated distance.

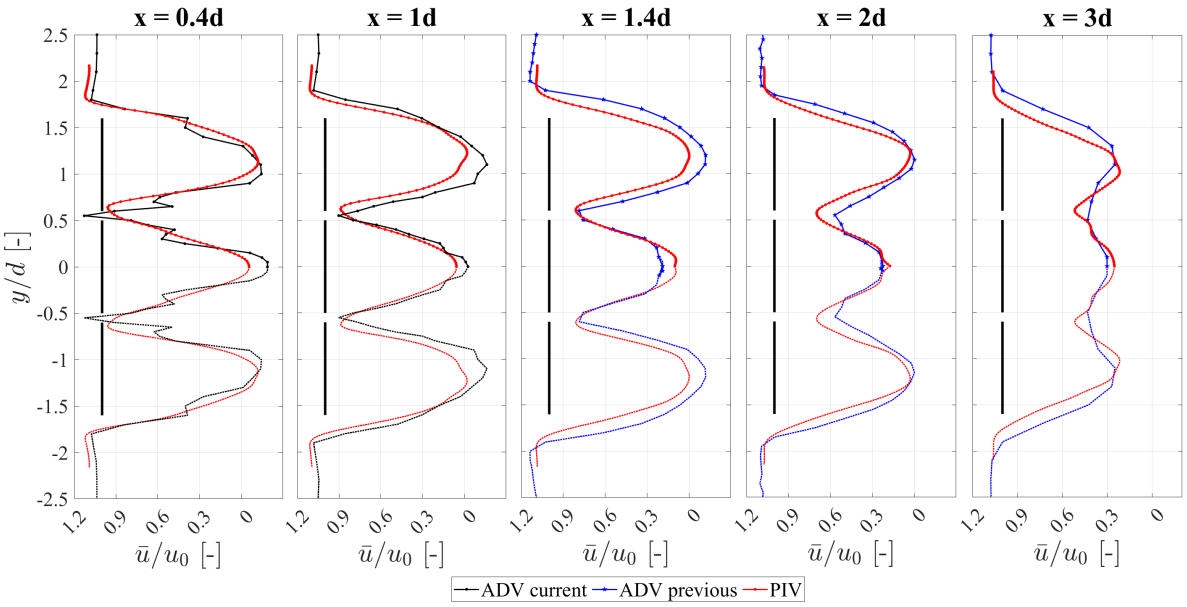

Figure 4.33: *Very near wake velocity reduction comparison between ADV and PIV results for MR7, at $x = 0.4d$, $1d$, $1.4d$, $2d$, and $3d$. Measurements at $x = 1.4d$ to $x = 3d$ provided by Skoland [19].*

The curves from the two different measurement techniques show good consistency in the shape of the velocity reduction. Both profiles indicate a distinct velocity drop behind the center point of each actuator disc in the setup. This velocity drop reduces as the downstream distance increases. Although the velocity trend is similar, the wake expansion and the velocity reduction are slightly different around each disc in the multirotor configuration. At $x = 0.4d$

and $x = 1d$, the velocity reduction is higher for the ADV curve. Additionally, a faster in-between jet stream is present for ADV at $x = 0.4d$. The ADV profiles at $x = 1.4d$ to $3d$ are provided by Skoland [19]. Observing the outer discs shows that the ADV method gives a wider wake than the PIV method. On the contrary, the wake expansion for the center disc is only marginally higher for the PIV method, shifting the location of the in-between jet stream. However, the velocity reduction behind the center disc is more consistent, with the only noticeable exception being at $x = 1.4d$, where the PIV shows a higher velocity reduction.

A possible explanation for these differences could be a small mismatch in terms of the horizontal or vertical location downstream at which the measurements were conducted, i.e if the profiles were measured in the wake center or slighly off. Even a small difference could have a big impact on the obtained velocity profile, with the very near wake being very sensitive to changes in velocity. Moreover, the sampling length for the ADV campaign could have been too small again, explaining the rapid fluctuations, especially observable at $x = 0.4d$. This could also have been the case for the PIV measurements. However, as Figure 3.21 highlights, the convergence analysis did not reveal any significant difference between the various sample lengths. Therefore, the selected length of 1200 samples was deemed sufficient.

Furthermore, the obtained tke results for the very near wake from the ADV and PIV measurements are compared in Figure 4.34.

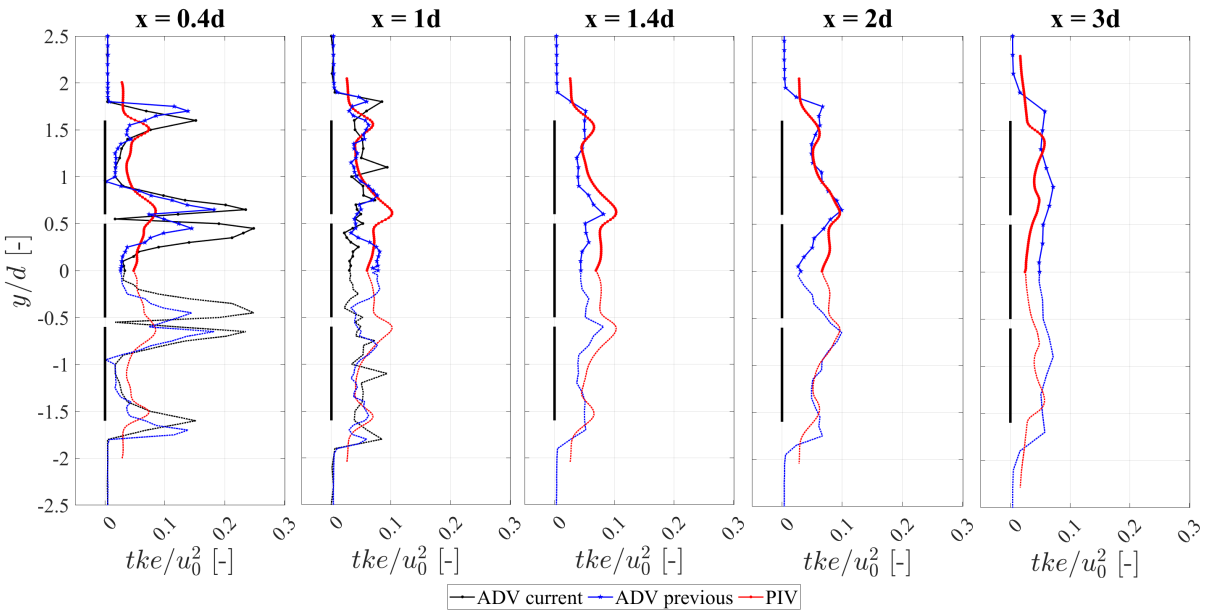

Figure 4.34: *Very near wake tke comparison between ADV and PIV results for MR7 at $x = 0.4d$, $1d$, $1.4d$, $2d$, and $3d$. [19].*

In this figure, the previous ADV results from Skoland [19] are included for comparison. At $x = 0.4d$, a significant difference in the current and previous ADV results is observed. However, the shape of the curves and peak tendencies are similar. As described in Section 3.7, the performed measurements from this campaign could have happened at an even closer downstream distance. On the other hand, the PIV results indicate a significantly lower tke at this distance, although the peak patterns align with those observed between the discs and at the edges of the outer discs. Explaining this difference is challenging. However, high tke values are expected in the immediate wake of the turbine, as this region is highly anisotropic with complex wake interactions between the discs. Thus, the discrepancies in tke values between ADV and PIV measurements in this region might be due to the challenges associated with accurately characterizing the turbulent flow in such a complex and dynamic environment. By studying the flow further downstream from $x = 1d$ to $x = 3d$, the curves are more similar.

Nevertheless, as the SR comparison results from Figure 4.32, the PIV curve is not converging to 0 in the free stream region. Again, the individual normal stresses are investigated in Figure 4.35 to isolate the three velocity components.

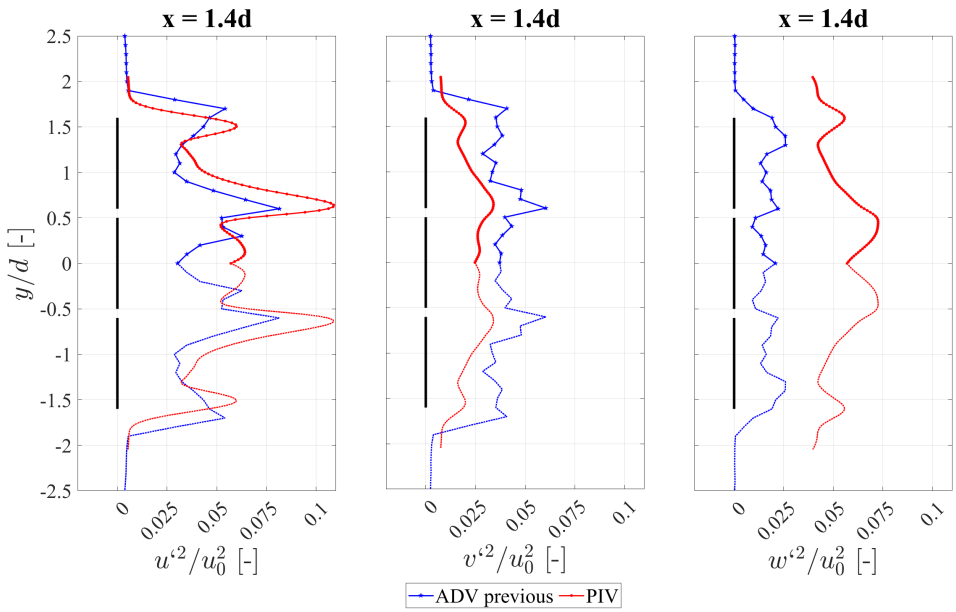

Figure 4.35: *Very near wake normal stress comparison between ADV and PIV results for MR7 at $x = 1.4d$ [19].*

Figure 4.35 confirms the previously observed pattern. Once again, the w'^2-component is seemingly too high, influencing the tke results. Like the SR experiments, the multi-camera was vertically oscillating. Thus, the added heave motion is suspected to have influenced the results.

Furthermore, Figure 4.36 shows the velocity reduction comparison in the near wake at $x = 2D$, where the individual disc wakes have merged into one large wake profile.

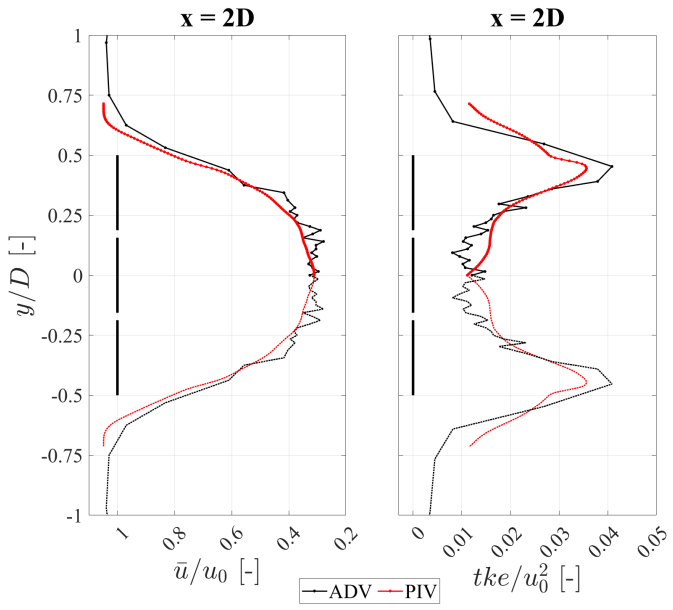

Figure 4.36: *Near wake velocity reduction and tke comparison between ADV and PIV results for MR7 at x = 2D.*

The figure gives consistent outcomes for both measurement methods' velocity reduction and wake width. However, closer examination of the ADV curve once again reveals some fluctuations in the wake center, a common observable pattern in many ADV measurements. In contrast, the PIV curve displays a smoother pattern. As for the tke curves, the shape and turbulence level is quite consistent, with a lower turbulence at the center of the multirotor and a higher turbulence occurring at the edges of the outer discs. However, the ADV curve gives a slightly higher peak value of 13%.

4.6.3 ADV comparison between MR7 and SR

In the following subsection, the SR and MR7 ADV results will be compared. This has previously been done in previous studies such as Skoland [19], where the results indicated that a lower initial velocity deficit was present for SR compared to MR7. However, the downstream wake of SR recovered faster, revealing a lower velocity deficit in the far wake at $x = 10d$. This study will further compare the various center disc solidity cases, investigating how this parameter affects the wake characteristics and recovery process.

The downstream wake characteristics are clearly different between SR and MR7. Figure 4.37 shows this difference for each disc solidity configuration at the same downstream distance of $x = 2d$.

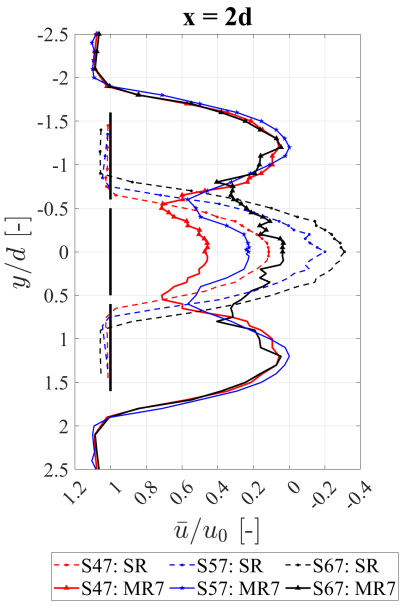

Figure 4.37: *Comparison between SR and MR7 at $x = 2d$.*

As the figure illustrates, it is observable that a higher velocity reduction is present for SR compared to MR7 for all the cases in the center. Additionally, MR7 has a considerably wider wake due to the outer discs in the MR setup. The differences become more apparent by further separating these velocity profiles with respect to each center disc solidity. Hence, Figure 4.38 illustrates a further comparison.

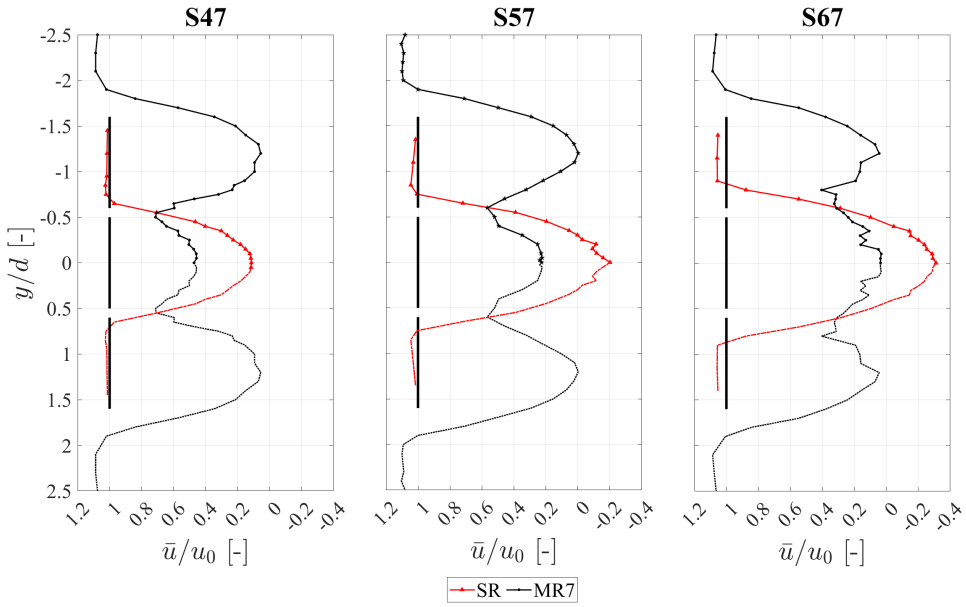

Figure 4.38: *Comparison between SR and MR7 at x = 2d.*

From Figure 4.38, it is observable that the SR has a higher velocity reduction compared to the center disc in the MR setup. However, for S47, the outer disc has a slightly higher velocity loss. This is as expected due to the outer disc having a solidity of 57%, thereby blocking more of the flow than an SR with a lower solidity percentage. For S57 and S67, the velocity reduction is higher for SR than for the center and outer discs. For each solidity case, the SR's wake is wider than the center disc in the configuration. This is due to the jet stream between the lateral discs causing a narrower wake than an isolated disc.

Furthermore, it will be interesting to review the wake differences by considering the downstream distance with respect to the total diameter of the arrangement. Thus, comparing the near wake, $x = 2D$ and $x = 2d$, and far wake,$x = 7D$ and $x = 7d$. Figure 4.39 shows this overview.

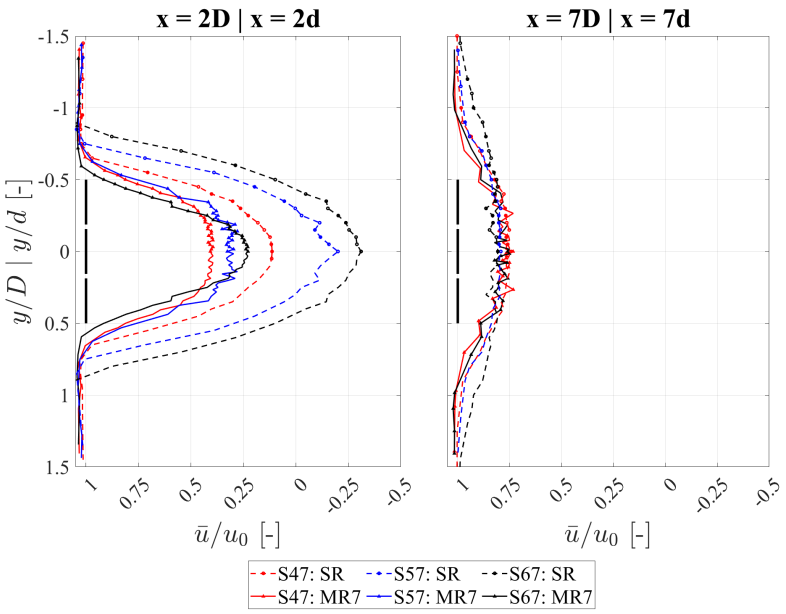

Figure 4.39: *Comparison between MR7 and SR at downstream distances of $x = 2d$ and $x = 2D$, $x = 7d$ and $x = 7D$.*

The near-wake development at $x = 2D$ and $x = 2d$ follows a clear pattern. The velocity reduction gets higher by increasing the disc solidity for MR7. The reduction for SR is even higher, also increasing with the solidity. This pattern also applies to the width of the wake. Hence, by considering the normalized downstream distance with respect to the associated diameter, it becomes clear that the MR7 wake recovers faster in the near wake. On the contrary, in the far wake, the differences between the wake profiles are only marginal at $x = 7D$ and $x = 7d$. Thus, the wake recovery of SR has caught up with MR7. These results are consistent with previous experimental research by Skoland [19] and Jørs & Mjåtveit [28], who stated that the in-between jet streams enhanced wake recovery. Furthermore, Bastankhah & Abkar [17] found that an increased number of rotors could lead to a faster recovery in the near wake.

The differences in velocity reduction are again more explicit by separating the velocity profiles with respect to each center disc solidity. Hence, Figure 4.40 further compares the near-wake at a distance of $x = 2D$ and $x = 2d$.

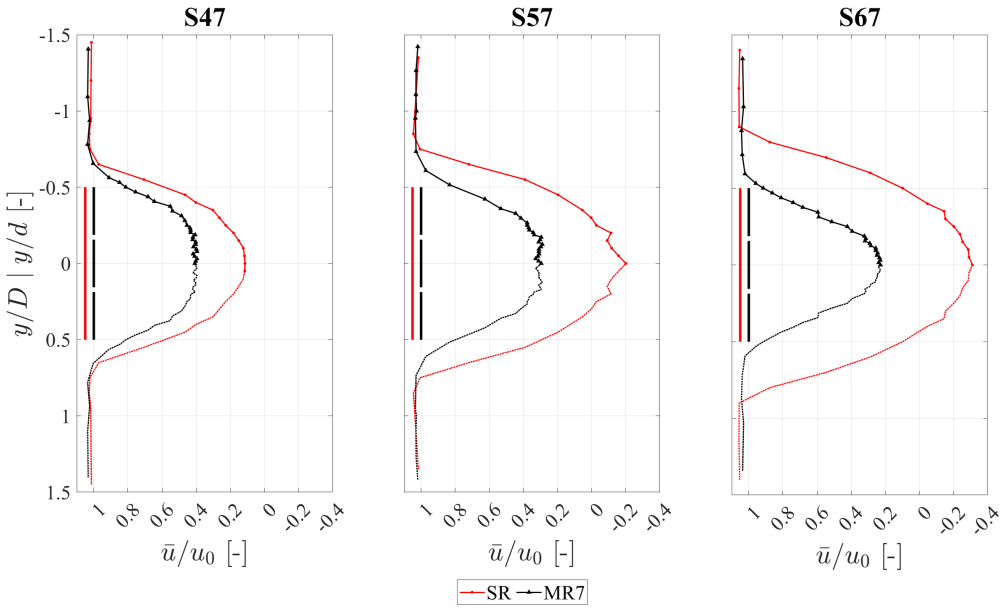

Figure 4.40: *Comparison between MR7 and SR at downstream distances of $x = 2d$ and $x = 2D$, respectively.*

An interesting takeaway from Figure 4.40 is that both the differences in velocity reduction and wake width of SR and MR7 increase by an increased disc solidity. An isolated analysis of the velocity profiles at a downstream distance of $x = 7D$ and $x = 7d$ was not performed, as the differences far wake is less comprehensive.

4.6.4 Comparison with previous experimental results

As previously specified, this ADV-based experimental approach has been used in previous research [20], [19], [57]. Thus, comparing the ADV and PIV results for SR and MR7 from the current campaign with previous campaigns will be interesting. First, the results for SR will be compared to a previous experimental study performed by Øye [57]. Hence, Figure 4.41 summarizes this comparison for S57.

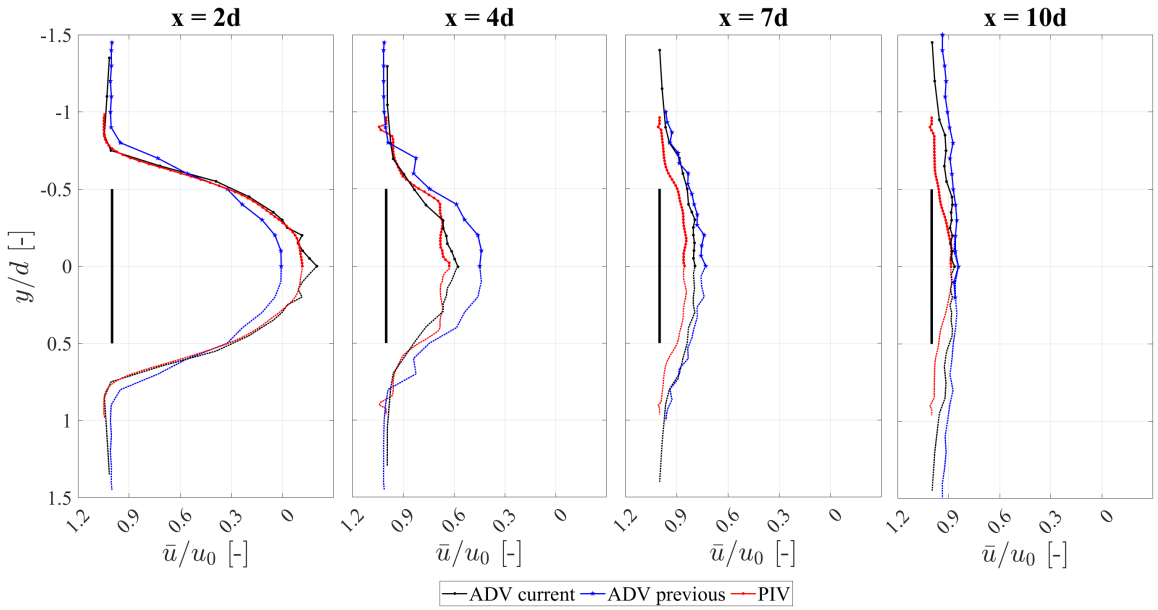

Figure 4.41: *Comparison between current and previous [57] experimental campaign for downstream measurements at $x = 2d$, $4d$, $7d$, and $10d$.*

A clear trend from Figure 4.41 is that the current campaign's velocity reduction is higher in the near wake at $x = 2d$. Subsequently, the wake recovers faster, confirmed by the smaller velocity reduction at $x = 4d$. By further studying the curves in the far wake, the difference is less significant, with the curves coinciding. As previously highlighted, velocity measurements are very sensitive to the vertical location and downstream distance at which the measurements were conducted. Hence, a slight mismatch in measurement location in x- or z-direction could potentially explain the differences in the near wake.

Koi [20] also investigated the upstream induction zone. This was done by taking several upstream velocity measurements based on the same horizontal distances from $x = 0.4d$ to $x = 3d$. Her goal was to investigate how this induction zone changed by varying the inter-rotor spacing in the multirotor setup. The spacing was set to a distance of $s = 0d$, $s = 0.1d$, and $s = 0.4d$, respectively. However, the solidity of the center disc remained the same throughout her experimental campaign, with a solidity of $s = 57\%$. Thus, comparing some of her measurements with those taken in this research campaign will be interesting. Figure 4.42 compares these experiments with the same center disc solidity and inter-rotor spacing.

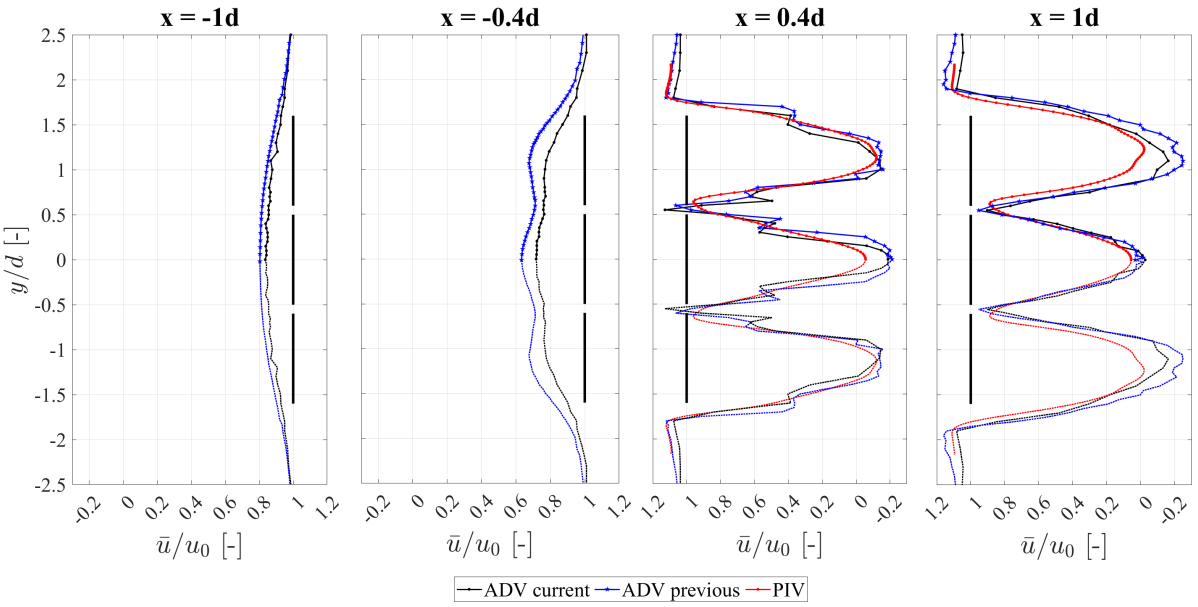

Figure 4.42: *Comparison between current and previous [20] experimental campaign for upstream and downstream measurements for x = -1d, -0.4d, 0.4d, and 1d.*

As the figure clearly illustrates, there is a small difference between the velocity relationships between the experimental campaigns. Generally, the velocity reduction in previous experiments seems to be higher for all the different distances, further confirmed by Table 4.6.

Table 4.6: *Comparison between the current and previous experimental campaign.*

	Max. u/u0 [%]		**Max. velocity reduction [%]**	
x/d	**Previous**	**Current**	**Previous**	**Current**
-1	80.42	83.61	19.58	16.39
-0.4	63.24	71.73	36.76	28.27
0.4	-21.20	-18.81	121.2	118.81
1	-24.77	-16.18	124.77	116.18
x/d	**Comparison**			
-1	-3.19		3.19	
-0.4	-8.49		8.49	
0.4	-2.39		2.39	
1	-8.59		8.59	

As the table illustrates, the maximum velocity reduction is consequently higher for the previous experiment, with the highest difference at x = -0.4d and x = 1d. The reasons behind this difference are complex, as several different factors could have had an impact. One reason could be an offset of the position of the ADV in the z-direction. The ADV instrument is very sensitive, and only a difference of 1 cm could have a major influence on the performed measurements. Another reason could be a different stiffness in the support structure of the

multirotor setup. Both the ADV and the multirotor are towed through the tank. The multirotor configuration will then experience a drag force that the support structure needs to withstand. If this is not properly taken into account, then a structure bending can appear, leading to inaccurate measurements. Only a visual check from outside the tank was done to evaluate this effect. Nevertheless, it is difficult to say how much bending occurred and how this differed from Koi's experiments.

Furthermore, Koi used a towing velocity of $u_0 = 0.4$ m/s, while this experiment was based on a towing velocity of $u_0 = 0.5$ m/s. Even though a difference of $u = 0.1$ m/s should not have a great impact on the normalized results, the increased velocity could lead to a higher drag force. Hence contributing to a bigger tower bending and smaller distance between MR7 and ADV.

This page is intentionally left blank.

Chapter 5

Conclusion

The multirotor concept is still in the research stage, where more knowledge related to upstream and downstream flow interactions is necessary for designing an optimal rotor design. Through this thesis, a parameter study of different center disc solidities for lab-scaled SR and MR7 configurations has been conducted experimentally using an ADV- and PIV-based measurement approach. By increasing the center disc solidity and, thereby, the local blockage ratio, the upstream region experiences a higher thrust force and induction zone. Additionally, the width of the downstream wake increased, with a higher velocity reduction in the very near wake region. As the flow moved further downstream, a faster wake recovery for the higher solidity center disc was observable. This wake development was due to higher shear stress, turbulent kinetic energy, and cross-stream in the near wake region. Thus having a center turbine of greater solidity means higher thrust force and faster wake recovery. However, it also means higher thrust force and associated tke, which could lead to more energy loss due to turbulence and vortices in the downstream flow. Therefore, a trade-off exists between the advantages and disadvantages of increased solidity, which must be carefully considered in the design process.

When considering the viability of multirotors versus single rotors for wind turbines, the experimental campaign shows that the multirotor configuration has advantages regarding wake recovery in the near wake region. Further downstream, the velocity reduction is similar at $x = 7d$ for the SR and $x = 7D$ for the MR7. Thus the SR wake experiences a faster wake recovery.

Nevertheless, the ADV and PIV results showed good agreement across the different measurements, both for SR and MR7. However, the PIV measurements showed too high tke values caused by induced vibrations from the submerged multi-camera during the towing of the experimental equipment in the tank. Thus influencing the w-component in the flow of the measurements. By improving the experimental setup with a more robust camera platform, more reliable results can be obtained.

Overall, this study demonstrates that PIV is a powerful tool for wake measurements in MarinLab. Its integration into future experimental campaigns will provide valuable insights into multirotor wind turbine arrangements' flow characteristics and wake behavior. In combination with computational fluid dynamics and optimization algorithms, PIV measurements could contribute to the advancement of designing efficient wind energy systems.

Chapter 6

Suggestions for Future Work

A potential direction for future work could be to further explore the effects of the rotor solidity on the turbine performance and wake flow. This could additionally be approached through numerical simulations, where the solidity parameter can be adjusted to observe its impact on various performance metrics such as power and thrust. Another avenue could be to design a physical model of a multirotor turbine, investigating how the number of rotors and their inter-rotor spacing can be varied to optimize performance. Such a study could potentially provide valuable insights into the design and optimization of multirotor wind turbines.

Furthermore, using actual rotating turbines in PIV experiments would provide a more realistic representation of real-world fluid mechanics and allow a better understanding of fluid flow dynamics around turbines. The use of rotating turbines would also enable the study of tip vortices and rotational movement in the downstream wake, which are crucial factors both for the performance of the individual turbines and vortex interactions in the near wake. Integrating PIV into this type of experiment would also provide more precise and accurate data due to the illumination's improved spatial and temporal uniformity. The combination of LED illumination and rotating turbines could significantly advance fluid mechanics and contribute to developing more efficient and effective turbine designs.

Moreover, practical issues concerning measurement methodology can be improved. Optimizing the seeding density through a sensitivity study is recommended to obtain more reliable results in future work with the PIV system. Optimizing the seeding density is criti-

cal for achieving accurate and reliable measurements. Conducting a seeding density study before the experiment will identify the optimal range of seeding density for the experimental campaign, thus avoiding overlapping particles, particle clustering, and increased noise. Additionally, improving the support structure for the multi-camera is important to avoid vibrations to the flow. Making it more robust will eliminate the added heave motion, enabling more reliable results. To better understand the impact of the multi-camera vibrations on the flow measurements, a spectral analysis of the frequency response of the camera mount could be conducted. This analysis will help identify the dominant frequencies that induce vibration and heave motion in the camera, thus enabling the design of a more effective support structure.

References

[1] P. Friedlingstein, M. O'Sullivan, M. W. Jones, R. M. Andrew, L. Gregor, J. Hauck, C. Le Quéré, I. T. Luijkx, A. Olsen, G. P. Peters, W. Peters, J. Pongratz, C. Schwingshackl, S. Sitch, J. G. Canadell, P. Ciais, R. B. Jackson, S. R. Alin, R. Alkama ... B. Zheng. Global Carbon Budget 2022, *Earth System Science Data*. 14(11): 4811-4900, 2022. doi:10.5194/essd-14-4811-2022.

[2] NOAA National Centers for Environmental Information. State of the Climate: Global Climate Report for Annual 2022. 2022. Retrieved from: https://www.ncei.noaa.gov/access/monitoring/monthly-report/global/202013. Accessed: 22.10.2022.

[3] United Nations / Framework Convention on Climate Change. Adoption of the Paris Agreement, 21st Conference of the Parties. 2015. Retrieved from: https://unfccc.int/resource/docs/2015/cop21/eng/l09r01.pdf. Accessed: 23.10.2022.

[4] P.R. Shukla, J. Skea, R. Slade, A. Al Khourdajie, R. van Diemen, D. McCollum, M. Pathak, S. Some, P. Vyas, R. Fradera, M. Belkacemi, A. Hasija, G. Lisboa, S. Luz and J. Malley, (eds.)]. Summary for Policymakers. In: Climate Change 2022: Mitigation of Climate Change. Contribution of Working Group III to the Sixth Assessment Report of the Intergovernmental Panel on Climate Change. IPCC. Cambridge University Press, Cambridge, UK and New York, NY, USA. doi: 10.1017/9781009157926.001.

[5] IEA. Defying expectations: CO2 emissions from global fossil fuel combustion are set to grow in 2022 by only a fraction of last year's big increase. 2022. Retrieved from: https://www.iea.org/news/defying-expectations-co2-emissions-from-global-fossil-fuel-combustion-are-set-to-grow-in-2022-by-only-a-fraction-of-last-year-s-big-increase. Accessed: 09.02.2023.

[6] United Nations. Goal 7: Affordable and clean energy. 2015. Retrieved from https://www.un.org/sustainabledevelopment/energy/. Accessed: 22.10.2022.

[7] R. Williams, F. Zhao, and J. Lee. GWEC | GLOBAL OFFSHORE WIND REPORT 2022. Retrieved from: https://gwec.net/gwecs-global-offshore-wind-report/. Accessed: 07.01.2023.

[8] Norwegian Goverment. Announces the first competitions for offshore wind. 2023. Retrieved from: https://www.regjeringen.no/en/aktuelt/announces-the-first-competitions-for-offshore-wind/id2969473/. Accessed: 03.04.2023.

[9] A. Colin. Wind turbines: Theory and practice. 2020. Cambridge University Press. University Printing House, Cambridge CB2 8BS, United Kingdom. doi 10.1017/9781108777469.

[10] S. Muggiasca, F. Taruffi, A. Fontanella, S.C. Carlo, H. Giberti , A. Facchinetti and M. Belloli. Design of an aeroelastic physical model of the DTU 10MW wind turbine for a floating offshore multipurpose platform prototype, *Ocean Engineering*, 239:109837. 2021, doi: 10.1016/j.oceaneng.2021.109837.

[11] N. Weekes. How powerful will wind turbines be in 2035? | windpower monthly, 2022. Retrieved from: https://www.windpowermonthly.com/article/1787760/powerful-will-wind-turbines-2035. Accessed: 22.08.2022.

[12] P. Jamieson and M. Branney. Structural Considerations of a 20MW Multi-Rotor Wind Energy System. *Journal of Physics Conference Series*, 555(1): 012013, 2014. doi: 10.1088/1742-6596/555/1/012013.

[13] G. Speakman, M. Abkar, L. Martínez-Tossas, and M. Bastankhah. Wake steering of multi-rotor wind turbines. *Wind Energy*, 24(11): 1294-1314. 2020. doi: 10.1002/we.2633.

[14] P. Jamieson, and M. Branney. Multi-Rotors; A Solution to 20 MW and Beyond? *Energy Procedia*. 24:52-59. 2012. doi: 10.1016/j.egypro.2012.06.086.

[15] M. van der Laan, S. Andersen, N. García, N. Angelou, G. Pirrung, S. Ott, M. Sjöholm, K. Sørensen, J. Neto, M. Kelly, T. Mikkelsen, and G. Larsen. Power curve and wake analyses of the vestas multi-rotor demonstrator. *Wind Energy Science*, 4:251–271, 2019. doi: 10.5194/wes-4-251-2019.

[16] Wind catching. 2022. Retrieved from: https://windcatching.com/ Accessed: 22.10.2022.

[17] M. Bastankhah, and M. Abkar. Multirotor wind turbine wakes. *Physics of Fluids*, 31(8): 085106, 2019. doi: 10.1063/1.5097285.

[18] N. Ghaias, A. Ghate, and S. Lele. Large-eddy simulation study of multi-rotor wind turbines. *Journal Physics Conference Seies*, 1037(7):072021, 2018. doi: 10.1088/1742-6596/1037/7/072021.

[19] M. Skoland. Experimental investigation of multirotor wind turbine wakes. 2022. Master's thesis, University of Bergen.

[20] I.M. Koi. Aerodynamic Interaction Effects on a Multi-Rotor Wind Turbine. 2022. Master's thesis, University of Bergen.

[21] R.J. Barthelmie, K. Hansen, S.T. Frandsen, O. Rathmann, J.G. Schepers, W. Schlez, K. Rados, A. Zervos, E.S. Politis, and P.K. Chaviaropoulos. Modelling and measuring flow and wind turbine wakes in large wind farms offshore. *Wind Energy*, 12(5):431–444, 2009. doi: 10.1002/we.348.

[22] T. Uchida. Effects of inflow shear on wake characteristics of wind-turbines over flat terrain. *Energies*, 13(14):3745, 2020. doi: 10.3390/en13143745.

[23] T. Göçmen, P Van der Laan, PE. Réthoré, A.P. Diaz, G.C. Larsen, and S. Ott. Wind turbine wake models developed at the technical university of Denmark: A review. *Renewable and Sustainable Energy Reviews*, 60: 752-769, 2016. doi: 10.1016/j.rser.2016.01.113.

[24] I. Dobrev, C. Maalouf, N. Troldborg, and F. Massouh. Investigation of the Wind Turbine Vortex Structure. Conference: 14th Int Symp on Applications of Laser Techniques to Fluid Mechanics. 2008. Retrieved from: https://www.researchgate.net/publication/229020500_Investigation_of_the_Wind_Turbine_Vortex_Structure. Accessed: 22.02.2023.

[25] K. Howard, A. Singh, F. Sotiropoulos, and M. Guala. On the statistics of wind turbine wake meandering: An experimental investigation. *Physics of Fluids*, 27(7):075103, 2015. doi: 10.1063/1.4923334.

[26] M. van der Laan, M. Baungaard, and M. Kelly. Brief communication: A clarification of wake recovery mechanisms. *Wind Energy Science*, 8(2): 247–254, 2023. doi: 10.5194/wes-8-247-2023.

[27] X. Xiong, S. Laima, and H. Li. Experimental study of the wake of multi-rotor turbine, *Ocean Engineering*, 269: 113594, 2023. doi: 10.1016/j.oceaneng.2022.113594.

[28] A.G. Jørs and T.L. Mjåtveit. Wake flow lab measurements of multi-rotor wind turbines. 2021. Bachelor's thesis, Western Norway University of Applied Sciences.

[29] J.P. Bentley. Principles of Measurement Systems. Pearson Education Limited, 4 edition, 2005. ISBN 0 130 43028 5.

[30] J. Bleeg, M. Purcell, R. Ruisi, and E. Traiger. Wind Farm Blockage and the Consequences of Neglecting Its Impact on Energy Production. *Energies*, 11(6):1609, 2018. doi: 10.3390/en11061609.

[31] A.M. Forsting, N. Troldborg, and M. Gaunaa. The flow upstream of a row of aligned wind turbine rotors and its effect on power production. *Wind Energy*, 20(1): 63–77, 2017. doi: 10.1002/we.1991.

[32] C. Garrett, and P. Cummins. The efficiency of a turbine in a tidal channel. *Journal of Fluid Mechanics*, 588: 243–251, 2007. doi: 10.1017/S0022112007007781.

[33] T. Nishino, and R. Willden . The efficiency of an array of tidal turbines partially blocking a wide channel. *Journal of Fluid Mechanics*, 708: 596–606, 2012. doi: 10.1017/jfm.2012.349.

[34] C.R. Vogel, and R. Willden. Multi-rotor tidal stream turbine fence performance and operation. *International Journal of Marine Energy*, 19: 198-206, 2017. doi: 10.1016/j.ijome.2017.08.005.

[35] J. Schluntz, and RHJ. Willden. The effect of blockage on tidal turbine rotor design and performance. *Renewable Energy*, 81: 432–441, 2015. doi: 10.1016/j.renene.2015.02.050.

[36] F. Zhu, L. Ding, B. Huang, M. Bao, and J. Liu. Blade design and optimization of a horizontal axis tidal turbine. *Ocean Engineering*, 195:106652, 2020. doi: 10.1016/j.oceaneng.2019.106652.

[37] A. Wimshurst, and R. Willden. Computational analysis of blockage designed tidal turbine rotors. 2nd International Conference on Renewable Energies Offshore. 2016. doi: 10.1201/9781315229256-71.

[38] H. Sun, X. Gao, and H. Yang. A review of full-scale wind-field measurements of the wind-turbine wake effect and a measurement of the wake-interaction effect. *Renewable and Sustainable Energy Reviews*, 132(1): 110042, 2020. doi: 10.1016/j.rser.2020.110042.

[39] R.J. Barthelmie, S.C. Pryor, S.T. Frandsen, K.S. Hansen, J.G. Schepers, K. Rados, W. Schlez, A. Neubert, L.E. Jensen, and S. Neckelmann. Quantifying the impact of wind turbine wakes on power output at offshore wind farms. *Journal of Atmospheric and Oceanic Technology*, 27(8): 1302–1317, 2010. doi: 10.1175/2010JTECHA1398.1.

[40] J. Schneemann, F. Theuer, A. Rott, M. Dörenkämper, and M. Kühn. Offshore wind farm global blockage measured with scanning lidar. *Wind Energy Science*, 6(2): 521–538, 2021. doi: 10.5194/wes-6-521-2021.

[41] S. Steen. Lecture notes in "Experimental Methods in Marine Hydrodynamics", NTNU Marin Teknikk, 2014.

[42] A. Buljan. Mingyang produces 'world's longest' anti-typhoon offshore wind turbine blade | offshore wind, 2022. Retrieved from: `https://www.offshorewind.biz/2022/12/19/mingyang-produces-worlds-longest-anti-typhoon-offshore-wind-turbine-blade/`. Accessed: 10.11.2023.

[43] M. Kanoglu Y. Cengel, M. Boles. *Thermodynamics: An Engineering Approach*. McGraw-Hill Education, 9 edition, 2018. ISBN 9781259822674.

[44] International Towing Tank Commission. Recommended Procedures: Fresh Water and Seawater Properties. 2011. Retrieved from: `https://ittc.info/media/4048/75-02-01-03.pdf`. Accessed: 11.03.2023.

[45] S.F. Hoerner. *Fluid Dynamic Drag: Practical Information on Aerodynamic Drag and Hydrodynamic Resistance*. Hoerner Fluid Dynamics, 1965. ISBN 9991194444.

[46] J. Whelan. *A fluid dynamic study of free-surface proximity and inertia effects on tidal turbines*. Doctoral dissertation, Imperial College London, South Kensington Campus, S

W 7 2A Z, 2010.

[47] G. Stenfelt, D. Lande Sudall, and J. Bartl. The Western University of Applied Science. MarinLab. 2022. Retrieved from: https://www.hvl.no/contentassets/de9d0d0d3cc146f3a0782a81d34f8e13/marinlab_info.pdf Accessed: 22.11.2022.

[48] S. Helvig, M. Vinnes, A. Segalini, N. Worth, and J. Hearst. A comparison of lab-scale free rotating wind turbines and actuator disks. *Journal of Wind Engineering and Industrial Aerodynamics*, 209:104485, 2021. doi: 10.1016/j.jweia.2020.104485.

[49] R. Garnes, J. Jensen, and A. Rogne. Upstream Blockage and Downstream Wake Flow of a Wind Turbine. 2020. Bachelor's thesis, Western Norway University of Applied Sciences.

[50] M. Hansen, C. Leikvoll, and M. Vikse. Multirotor wind turbine-drag. 2021. Bachelor's thesis, Western Norway University of Applied Sciences.

[51] Nortek Group. The comprehensive manual for velocimeters, 2021. Retrieved from: https://www.nortekgroup.com/assets/software/N3015-030-Comprehensive-Manual-Velocimeters_1118.pdf. Accessed: 10.10.2022.

[52] I.M. Viola, A. Nila, T. Davey, and R. Gabl. Underwater LED-based Lagrangian Particle Tracking Velocimetry. *Journal of Visualization*, 25: 1035-1046, 2022. doi: 10.1007/s12650-022-00832-z.

[53] LaVision. Particle Image Velocimetry. 2022. Retrieved from: http://www.lavision.de/en/techniques/piv-ptv/index.php Accessed: 11.02.2023.

[54] D. Groß, B. Wernher, and J. Gerhard. Development of a LED-based PIV/PTV system: Characterization of the flow within a cylinder wall-array in a shallow flow. River Flow 2010, 1672, Karlsruhe, 2010. Bundesanstalt für Wasserbau. Retrieved from: https://henry.baw.de/server/api/core/bitstreams/98b7f9d6-718b-438b-91c0-c641e8cd87c4/content. Accessed: 24.03.2023.

[55] B. Wieneke. Improvements for volume self-calibration. *Measurement Science and Technology*, 29(8): 084002, 2018. doi: 10.1088/1361-6501/aacd45.

[56] LaVision. Seeding Particles. Retrieved from: https://www.lavision.de/en/app

lications/fluid-mechanics/piv-system-components/seeding-particles/ Accessed: 24.04.23.

[57] S. Øye. Experimental study of the wake flow and thrust coefficient of porous actuator discs. 2022. Master's thesis, University of Bergen.

[58] LaVision. Product manual for DaVis 10.2. 2022. Retrieved from: https://www.lavision.de/fileadmin/downloads/documentation/davis10.2/Product_Manual_DaVis_10.2.pdf. Accessed: 17.12.2022.

[59] J. R. Bjørnsen. Lab-scale measurements of blockage and wake flow on a setup of three laterally spaced wind turbine rotors. Master's thesis, University of Bergen, 2021.

This page is intentionally left blank.